Tensor renormalization group approach to higher-dimensional lattice field theories

Shinichiro Akiyama

February 2022

Tensor renormalization group approach

to higher-dimensional lattice field theories

Shinichiro Akiyama

Doctoral Program in Physics

Submitted to the Graduate School of
Pure and Applied Sciences
in Partial Fulfillment of the Requirements
for the Degree of Doctor of Philosophy in
Science

at the
University of Tsukuba

Contents

1   Introduction

The quantum field theory (QFT) is a powerful framework to describe various types of physical phenomena in high-energy systems and many-body cooperative phenomena. Within this framework, one of the most important problems is to consider the path integral for a theory defined by the Lagrangian or the Hamiltonian. In high-energy physics, such a theory is defined on a continuum, which corresponds to the four-dimensional spacetime. Therefore, the path integral results in multiple integrals with uncountably infinite degrees of freedom, that is a mathematically ill-defined object. Related to this issue, the QFT in high-energy physics is usually defined via the perturbation theory, so there is an essential difficulty when we discuss non-perturbative physics. A typical example is the quantum chromodynamics (QCD), which describes the strong interaction between quarks and gluons. Although we can understand the short-range physics in the QCD with the perturbative discussion thanks to the asymptotic freedom, we can no longer investigate the long-range physics, which is outside of the scope of perturbation theory.

As a successful way to access the non-perturbative regimes, we have the lattice field theory pioneered by K. G. Wilson [Wil74]. In the lattice field theory, a continuum spacetime is replaced by a discrete lattice that allows us to consider a theory characterized by countably infinite, or finite, degrees of freedom and its continuum limit defines the quantum field theory in a mathematically rigorous manner. Moreover, the lattice field theory has a deep connection with the statistical physics [Kog79]. The procedure of the renormalization is well understood by the renormalization group, which is an important tool to understand not only high-energy physics but also the critical phenomena [WK74]. This is of great significance because once we move on to the lattice theory, we have a chance to evaluate various observables via the philosophy of the statistical ensemble. One of the most efficient methods to investigate the field theory on a lattice is the Monte Carlo (MC) simulation, which is a stochastic numerical method based on the idea of sampling. The MC method is widely applied in the study of high-energy physics. Lattice QCD calculation is a typical example of the application of the MC method and it has been playing an essentially important role to understand the non-perturbative physics in the QCD.

However, the MC simulation faces a serious difficulty when one cannot assume the probabilistic interpretation for the given Boltzmann weight. This difficulty is known as the sign problem, a serious obstacle to the numerical study of lattice field theories. A notable example where the sign problem takes place is in the systems at finite density. In particular, high-density systems such as the internal states of neutron stars, are extremely difficult to understand experimentally, and thus the expectation for numerical approaches is very high. However, due to the sign problem, many physical phenomena peculiar to finite-density systems are still not understood from the fundamental theory.

In view of this situation, we need a numerical methodology that potentially enables us to investigate the regimes where it is difficult to access with the standard MC simulation. This thesis focuses on the tensor renormalization group (TRG) from this point of view. The TRG approach is a type of the tensor network method, where we express a physical object, such as a (ground) state, observable, or path integral, by a tensor contraction, which is numerically evaluated via a certain tensor network algorithm. The idea of the tensor network was originally developed in the field of statistical physics and one of the most famous applications is the density matrix renormalization group (DMRG). The DMRG provides one with an extraordinary accurate numerical simulation for a certain class of one-dimensional quantum system [Whi92, Whi93]. Recently, the tensor network method has been in the spotlight, also in the context of the quantum information theory. From such a perspective, the various numerical algorithms are reviewed in Refs. [Orú19, ONU21]. The application of the tensor network method is a recent hot topic also in particle physics [BC20, BBC+20], including the TRG study of lattice field theories [MSUY20]. The TRG has many advantages over the standard MC method. Firstly, the TRG,

and also other tensor network algorithms, are free from the sign problem, because they do not resort to any probabilistic interpretation for the given Boltzmann weight. Secondly, the computational cost of the TRG algorithm scales logarithmically with respect to the lattice volume. This benefit comes from the fact that the TRG algorithm is based on the idea of a real-space renormalization group, which allows us to enlarge the system size toward the thermodynamic limit as a result of iterating the renormalization-group transformations. Thirdly, we can deal with the Grassmann fields directly within the TRG approach. In other words, we do not have to introduce any bosonic auxiliary fields to rewrite fermions. This is another practical benefit because such a bosonic auxiliary field sometimes introduces non-local interactions, which require more computational cost to simulate. Fourthly, the TRG enables us to numerically evaluate the partition function or the path integral itself. Indeed, with the MC method, we cannot directly calculate it, because it is not regarded as any expectation value. Since the partition function or the path integral is a generating functional, we are then allowed to derive various thermodynamic functions in principle once we obtain it. In addition, there is a superior feature in the TRG approach, compared with other tensor network algorithms, which is the applicability to the higher-dimensional, more than two-dimensional, systems on the thermodynamic lattice. Originally, the TRG was proposed to investigate the two-dimensional spin systems in Ref. [LN07], which has been followed by the various extensions with respect to the higher-dimensional application and the improvement of the accuracy. Therefore, it can be said that the TRG approach is a powerful candidate to investigate the regime whose investigation with the MC method is seriously hindered by numerical obstacles. The aim of this thesis is to study such a regime in various types of lattice field theory, exploiting these advantages of the TRG approach.

This thesis is organized as follows. In Sec. 2, we review how to construct a tensor network representation for a path integral. After that, we review the several TRG algorithms which are applied in the following sections. An extension of these algorithms to investigate lattice fermions is also demonstrated here, based on the formalism given in Ref. [AK21a]. The first part of Sec. 3 is also devoted to reviewing the numerical accuracy of the TRG algorithms by benchmarking with the Ising model. We then apply the TRG method to the four-dimensional Ising model. This part is based on Refs. [AKYY19], which is the first application of the TRG approach to the four-dimensional system. Sec. 4 explains the TRG study of the lattice ϕ^4 theory. Since the ϕ^4 theory is a non-compact field theory, its numerical treatment within the TRG approach is nontrivial. We look at the lattice ϕ^4 theory from the viewpoint of the relationship to the Ising model and discuss its phase transition. This part is based on Ref. [AKY21b]. In Sec. 5, we demonstrate the efficiency of the TRG approach for the four-dimensional system with the sign problem. In this context, we investigate the complex ϕ^4 theory at finite density, whose Silver Blaze phenomenon is a primary target. This section is based on Ref. [AKK$^+$20], which is the first application of the TRG approach to the four-dimensional quantum field theory. Application of the TRG method to lattice fermions is discussed in Sec. 6, where we study the Hubbard model at finite density. This model is a very fundamental model of the strongly correlated electrons. Moving on to the path-integral formalism, we are allowed to investigate the models with the TRG approach, whose efficiency at finite density is discussed. These TRG studies are based on Refs. [AK21b, AKY21a]. In Sec. 7, the TRG approach is extended to investigate the four-dimensional Nambu–Jona-Lasinio model at finite density, which is an effective theory of the QCD at finite density. Our research target is to numerically investigate the chiral-symmetry restoration in the cold and dense regime, where a naive MC simulation is prohibited by the serious sign problem. This section is based on Ref. [AKYY20], which is the first application of the TRG method to the four-dimensional lattice fermions. Finally, Sec. 8 is devoted to the conclusion.

2 Procedure of the tensor renormalization group approach

A primary target in the TRG approach is to evaluate a path integral. To this aim, one firstly needs to derive a tensor network representation for the path integral. Secondly, we use a certain TRG algorithm to approximately evaluate it.

2.1 Bosonic tensor network representation

Usually, there are several ways to derive a tensor network representation for a path integral. Here, we would like to introduce one of the most general ways, that is, a derivation that is essentially applicable to any bosonic lattice model. The derivation is based on the idea that one decomposes hopping structures in the local Boltzmann weight via the singular value decomposition (SVD). One of the advantages of this derivation is that we can introduce the SVD-based approximation before we carry out the TRG algorithms when we deal with models with large degrees of freedom.

Let us begin with considering the $\mathbb{Z}_q$-spin model on a lattice whose path integral is given by the following form,

$$Z = \left(\prod_{n \in \Lambda_d} \sum_{\sigma(n)} \right) \prod_{n \in \Lambda_d} \exp \left[\sum_{\nu=1}^{d} W[\sigma(n), \sigma(n+\hat{\nu})] + M[\sigma(n)] \right]. \tag{2.1}$$

Here, we have assumed that the field $\sigma(n)$ takes the value on $\mathbb{Z}_q$. Λ_d denotes a d-dimensional hypercubic lattice whose lattice sites are labeled by n. This type of integration appears when we write down a partition function of a classical spin system. $W[\sigma(n), \sigma(n+\hat{\nu})]$ represents a hopping structure and $M[\sigma(n)]$ does an on-site term. For example, in the case of the Ising-like spin models, we have

$$W[\sigma(n), \sigma(n+\hat{\nu})] = \beta J \sigma(n) \sigma(n+\hat{\nu}) \tag{2.2}$$

as a nearest-neighbor interaction term with the inverse temperature β and the coupling J and

$$M[\sigma(n)] = h \sigma(n) \tag{2.3}$$

as an external magnetic field term, which is parameterized by h. Thanks to the discreteness of $\sigma(n)$, we can identify the hopping structure as a $q \times q$ matrix,

$$T_{\sigma(n)\sigma(n+\hat{\nu})} = \exp \left[W[\sigma(n), \sigma(n+\hat{\nu})] \right]. \tag{2.4}$$

Then we apply the SVD for the matrix T, which gives us

$$T_{\sigma(n)\sigma(n+\hat{\nu})} = \sum_{i_\nu(n)} U_{\sigma(n)i_\nu(n)} s_{i_\nu(n)} V^*_{\sigma(n+\hat{\nu})i_\nu(n)}, \tag{2.5}$$

where $i_\nu(n)$ plays a role of ν-directional auxiliary field whose size is equal to $\sigma(n)$. The benefit of this decomposition is that one can integrate out $\sigma(n)$ at each lattice site, independently. As a result of this integration, one can introduce a $2d$-rank tensor,

$$\mathcal{T}_{i_1(n)\cdots i_d(n)i_1(n-\hat{1})\cdots i_d(n-\hat{d})} = \sum_\sigma \mathrm{e}^{M[\sigma]} \prod_{\nu=1}^{d} U_{\sigma i_\nu(n)} V^*_{\sigma i_\nu(n-\hat{\nu})} \sqrt{s_{i_\nu(n)}} \sqrt{s_{i_\nu(n-\hat{\nu})}}. \tag{2.6}$$

By definition, the trace of $\mathcal{T}$ is equal to a weight of periodic one-site model, that is,

$$\sum_{i_1,\cdots,i_d} \mathcal{T}_{i_1\cdots i_d i_1\cdots i_d} = \sum_\sigma \exp \left[d \times W[\sigma, \sigma] + M[\sigma] \right] \tag{2.7}$$

holds. In the above expression, we have assigned singular values for all subscripts of $\mathcal{T}$. It is also possible to define the hopping matrix T as

$$T_{\sigma(n)\sigma(n+\hat{\nu})} = \exp\left[W[\sigma(n), \sigma(n+\hat{\nu})] + \frac{1}{2d}M[\sigma(n)] + \frac{1}{2d}M[\sigma(n+\hat{\nu})]\right]. \tag{2.8}$$

In this case, the resulting tensor $\mathcal{T}$ is given by

$$\mathcal{T}_{i_1(n)\cdots i_d(n)i_1(n-\hat{1})\cdots i_d(n-\hat{d})} = \sum_{\sigma(n)}\prod_{\nu=1}^{d}U_{\sigma(n)i_\nu(n)}V^*_{\sigma(n)i_\nu(n-\hat{\nu})}\sqrt{s_{i_\nu(n)}}\sqrt{s_{i_\nu(n-\hat{\nu})}}. \tag{2.9}$$

Eq. (2.1) is now written as

$$Z = \left(\prod_{n\in\Lambda_d}\prod_{\nu=1}^{d}\sum_{i_\nu(n)}\right)\prod_{n\in\Lambda_d}\mathcal{T}_{i_1(n)\cdots i_d(n)i_1(n-\hat{1})\cdots i_d(n-\hat{d})}. \tag{2.10}$$

Hereafter, we refer to the form of Eq. (2.10) as a tensor network representation for Z. Within the picture of the tensor network representation, the tensor $\mathcal{T}$ locates on each lattice site and the auxiliary field introduced by the SVD connects tensors on different sites. As a shorthand notation, we usually introduce a subscript with prime as

$$i'_\nu(n) = i_\nu(n-\hat{\nu}). \tag{2.11}$$

Since we usually assume periodic boundary conditions and this enables us to regard Eq. (2.10) as a kind of tensor trace, we sometimes denote Eq. (2.10) as

$$Z = \mathrm{tTr}\left[\prod_{n\in\Lambda_d}\mathcal{T}_{i_1(n)\cdots i_d(n)i'_1(n)\cdots i'_d(n)}\right]. \tag{2.12}$$

We illustrate Eq. (2.12) with $d = 2$ in Fig. 2.1.

Since the above derivation is based on the assumption that the field on a lattice takes the value on $\mathbb{Z}_q$, it is not straightforwardly applicable to lattice fields which take the value on $\mathbb{R}$ or $\mathbb{C}$. Such a lattice field theory is defined by the path integral,

$$Z = \left(\prod_{n\in\Lambda_d}\int \mathrm{d}\phi(n)\right)\prod_{n\in\Lambda_d}\exp\left[\sum_{\nu=1}^{d}W[\phi(n), \phi(n+\hat{\nu})] + M[\phi(n)]\right]. \tag{2.13}$$

In this case, the hopping matrix $T_{\phi(n)\phi(n+\hat{\nu})}$ becomes an infinite-dimensional matrix, so the corresponding tensor network representation of Z is generated by an infinite-dimensional tensor. Unfortunately, we cannot deal with such an infinite-dimensional array in practical computation. Therefore, we must introduce a kind of regularization that reduces an infinite-dimensional expression to a finite one. In other words, we must introduce a discretization scheme of $\phi(n)$ in some way. In the previous TRG studies, several ways to discretize continuous degrees of freedom are proposed [Shi12b, Shi12a, LMQ+13, Tak19, DT20, Tak21]. Here, we would like to consider the regularization based on the Gauss quadrature rule, which gives us an approximation of the definite integral of a function. One of the advantages is that one can derive tensor network representations for noncompact field theories in the way explained above. Although there are various types of quadrature rules reflecting on the integrand and the interval, they give us an approximation such as

$$\int \mathrm{d}x f(x) \approx \sum_{i=1}^{K} w_i f(x_i), \tag{2.14}$$
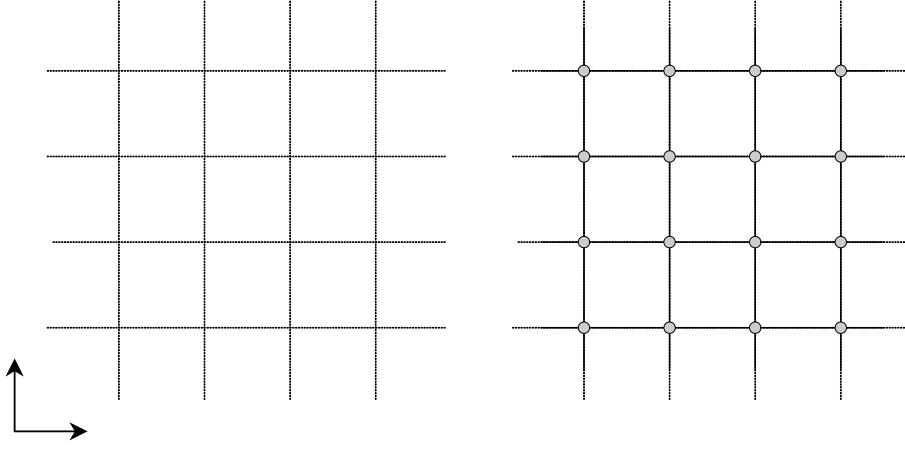
Figure 2.1: Schematic picture of the two-dimensional tensor network representation of Eq. (2.12). Left figure shows a two-dimensional square lattice. Right one represents the two-dimensional tensor network on it. Each tensor is denoted by gray symbol and they are located on lattice sites.

which is characterized by a weighted sum at specific points in the integration domain with nodes x_i and weights w_i. In practical calculation, we have to make a proper choice of these nodes and weights following the algorithm of the Gauss quadrature rules. Applying Eq. (2.14) to the integration over a non-compact field $\phi(n)$, one obtains

$$\int \mathrm{d}\phi(n) F\left[\phi(n)\right] \approx \sum_{i=1}^{K} w_i F\left[\phi_i(n)\right]. \tag{2.15}$$

For notational convenience, we introduce the vector representation for $\phi_i(n)$ as $\tilde{\phi}(n)$. We also rewrite w_i as $w_{\tilde{\phi}(n)}$. Using these notations, we express the right-hand side of Eq. (2.15) as

$$\sum_{\tilde{\phi}(n)} w_{\tilde{\phi}(n)} F\left[\tilde{\phi}(n)\right]. \tag{2.16}$$

Now, Eq. (2.13) can be approximated by a certain quadrature rule as

$$Z \approx \left(\prod_{n\in\Lambda_d}\sum_{\tilde{\phi}(n)} w_{\tilde{\phi}(n)}\right)\prod_{n\in\Lambda_d}\exp\left[\sum_{\nu=1}^{d} W[\tilde{\phi}(n),\tilde{\phi}(n+\hat{\nu})] + M[\tilde{\phi}(n)]\right]. \tag{2.17}$$

[1] Once we have approximated the original Z as in Eq. (2.17), we can apply the same derivation with the case of spin systems. The hopping matrix is given by $T_{\tilde{\phi}(n)\tilde{\phi}(n+\hat{\nu})}$, which can be regarded as a $K \times K$ matrix. Applying the SVD and carrying out the summation over $\tilde{\phi}(n)$ at each site independently, then

---

[1]When one applies a certain quadrature rule to an integral, some modification of the integrand can be required. However, at this stage, we forget it and explain the procedure to derive tensor network representations. As we see in the following, such modification does not change essential steps.

one obtains a tensor network representation of Eq. (2.17) in the form of Eq. (2.12). The weight $w_{\tilde{\phi}(n)}$ are treated as an additional on-site term.

So far, we have discussed the model just characterized by a nearest-neighbor hopping and an on-site structure like in Eqs. (2.1) and (2.13). Now, we would like to explain how to derive tensor network representations for lattice gauge theories, which are characterized by so-called plaquette interactions. For simplicity, we consider pure gauge theories in the following. Within the lattice gauge theory, we consider a link variable $U_\nu(n)$, which is defined on a link (n, ν). $U_\nu(n)$ takes its value on a gauge group G and the path integral of lattice gauge theory is given as a multiple integral on the group G such that

$$Z = \left(\prod_{n \in \Lambda_d} \prod_{\nu=1}^{d} \int dU_\nu(n) \right) \prod_{n \in \Lambda_d} \exp \left[\beta \sum_{\nu > \lambda} \Re\mathrm{Tr} \left[U_\nu(n) U_\lambda(n + \hat{\nu}) U_\nu^\dagger(n + \hat{\lambda}) U_\lambda^\dagger(n) \right] \right]. \tag{2.18}$$

β represents the inverse gauge coupling and $\Re(z)$ denotes the real part of $z (\in \mathbb{C})$. Notice that the summation,

$$\beta \sum_{\nu > \lambda} \Re\mathrm{Tr} \left[U_\nu(n) U_\lambda(n + \hat{\nu}) U_\nu^\dagger(n + \hat{\lambda}) U_\lambda^\dagger(n) \right] \tag{2.19}$$

runs over the all plaquettes living on $\nu\lambda$-plane with the condition of $\nu > \lambda$. In the d-dimensional hypercubic lattice Λ_d, we have $d(d-1)/2$ numbers of term in Eq. (2.19). The essential idea to derive the tensor network representation of Eq. (2.18) is almost same with the case of spin models. To make it clear, we assume $G = \mathbb{Z}_q$, for a while. The link variables in the $\mathbb{Z}_q$ gauge theory are parametrized according to

$$U_\nu(n) = \exp \left[\frac{2\pi i}{q} r_\nu(n) \right], \tag{2.20}$$

with the integer $r_\nu(n) = 0, 1, \cdots, q-1$. Thanks to this parametrization, we can express Eq. (2.18) as

$$Z = \left(\prod_{n \in \Lambda_d} \prod_{\nu=1}^{d} \sum_{r_\nu(n)} \right) \prod_{n \in \Lambda_d} \exp \left[\beta \sum_{\nu > \lambda} \cos \left(\frac{2\pi}{q} \left[r_\nu(n) + r_\lambda(n + \hat{\nu}) - r_\nu(n + \hat{\lambda}) - r_\lambda(n) \right] \right) \right]. \tag{2.21}$$

Defining a four-rank tensor P as

$$P_{r_\nu(n) r_\lambda(n+\hat{\nu}) r_\nu(n+\hat{\lambda}) r_\lambda(n)} = \beta \cos \left(\frac{2\pi}{q} \left[r_\nu(n) + r_\lambda(n + \hat{\nu}) - r_\nu(n + \hat{\lambda}) - r_\lambda(n) \right] \right), \tag{2.22}$$

we now consider its higher-order SVD (HOSVD), which gives us

$$P_{r_\nu(n) r_\lambda(n+\hat{\nu}) r_\nu(n+\hat{\lambda}) r_\lambda(n)} = \sum_{a,b,c,d} V_{r_\nu(n)a} V_{r_\lambda(n+\hat{\nu})b} V_{r_\nu(n+\hat{\lambda})c} V_{r_\lambda(n)d} B_{abcd}, \tag{2.23}$$

where V is a unitary matrix and B is a core tensor. As an advantage of this derivation, we can introduce the HOSVD-based approximation before we carry out the TRG algorithms when we deal with the lattice gauge theory with large gauge degrees of freedom. The core tensor B lives on a plaquette $\Box = (n, \nu, \lambda)$ and we emphasize it by writing

$$B_{\Box;abcd} = B_{abcd}. \tag{2.24}$$

As in the case of spin models, we are allowed to integrate out $r_\nu(n)$ at each link independently. As a result of this integration, one can introduce a $2(d-1)$-rank tensor A at each link $\ell = (n, \nu)$ according to

$$A_{\ell; m_1 \cdots m_{d-1} m'_1 \cdots m'_{d-1}} = \sum_r \left(\prod_{j=1}^{d-1} V_{rm_j} V_{rm'_j} \right). \tag{2.25}$$

Hereafter, we call A_ℓ as a link tensor, because it lives on a link ℓ and $B_\square$ as a plaquette tensor, because it does on a plaquette $\square$. The path integral of Eq. (2.21) is now described by a tensor network generated by A_ℓ's and $B_\square$'s. Although this is a tensor network representation, we can move on to the representation as in the form of Eq. (2.12) by employing "asymmetric formulation" derived in Ref. [LMQ$^+$13]. Within the asymmetric formulation on Λ_d, we use d pieces of A_ℓ's and $d(d-1)/2$ pieces of $B_\square$'s to construct a $2d$-rank tensor $\mathcal{T}_{c; i_1 \cdots i_d i'_1 \cdots i'_d}$ on a basic cell c of Λ_d. Each subscript $i_\nu^{(\prime)}$ consists of $d-1$ numbers of legs coming from A_ℓ's ($B_\square$'s). By definition, one finds

$$\sum_{i_1, \cdots, i_d} \mathcal{T}_{c; i_1 \cdots i_d i_1 \cdots i_d} = \mathrm{e}^{\beta d(d-1)/2}, \tag{2.26}$$

which means that the trace over $\mathcal{T}_c$ corresponds to a weight of the periodic one-site model. Note that the asymmetric formulation just rewrites the tensor network representation, but it provides us with a way to study the lattice gauge theory by the same TRG algorithms in spin systems. [2] Fig. 2.2 explains how to define $\mathcal{T}_c$ in two dimensions. Fig. 2.3 also shows the procedure of the two-dimensional asymmetric formulation, which should be compared with Fig. 2.1. The left representation in Fig. 2.3 has a same structure to that in Fig. 2.1, although $\mathcal{T}_c$ is not on a lattice site but on a plaquette which is a unit cell in two-dimensional square lattice. Fig. 2.4 explains structures of $\mathcal{T}_c$ in three- and four-dimensional lattices.

Finally, we would like to make a comment on the case where the gauge group G is a continuous group. To derive a tensor network representation, we need to employ some regularization to make finite-dimensional tensors. As such a regularization scheme, a certain Gauss quadrature rule is one of the candidates. Based on a regularization, one can then carry out the HOSVD as in Eq. (2.23) and introduce link tensors by integrating out the regularized gauge field at each link independently. [3]

2.2   Tensor renormalization group algorithms

The TRG was originally introduced by Levin and Nave to investigate two-dimensional classical spin models [LN07]. Following their work, various types of TRG algorithms have been proposed. The TRG algorithms can be regarded as variants of the real-space renormalization group because they are based on the idea that one can access a system in the thermodynamic limit as a result of iterating a simple renormalization-group transformation, which introduces some approximation. In TRG algorithms, such an approximation is usually given by the SVD. Here, we would like to review the higher-order TRG (HOTRG) algorithm [XCQ$^+$12] and the anisotropic TRG (ATRG) algorithm [AOT20a]. Both of them are typical TRG algorithms, which are applicable to any dimensional lattice system.
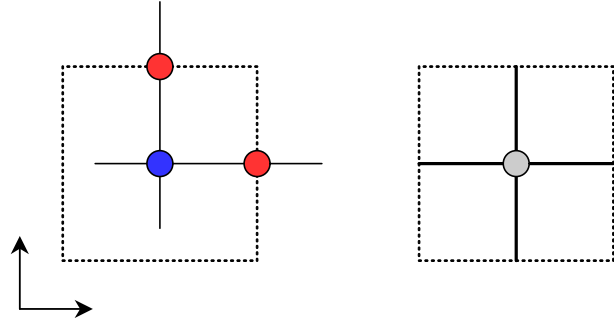
Figure 2.2: Schematic picture of $\mathcal{T}_c$ in two dimensions. Red symbol shows a link tensor A_ℓ and blue one does a plaquette tensor $B_\square$. Dotted lines show a square lattice. Combining two A_ℓ's and one $B_\square$, one obtains $\mathcal{T}_c$, which is denoted by a gray symbol in the right-hand side. Note that $\mathcal{T}_c$ is a four-rank tensor, $\mathcal{T}_{c;i_1 i_2 i'_1 i'_2}$, where i_1 and i_2 come from A_ℓ's and i'_1 and i'_2 come from $B_\square$.
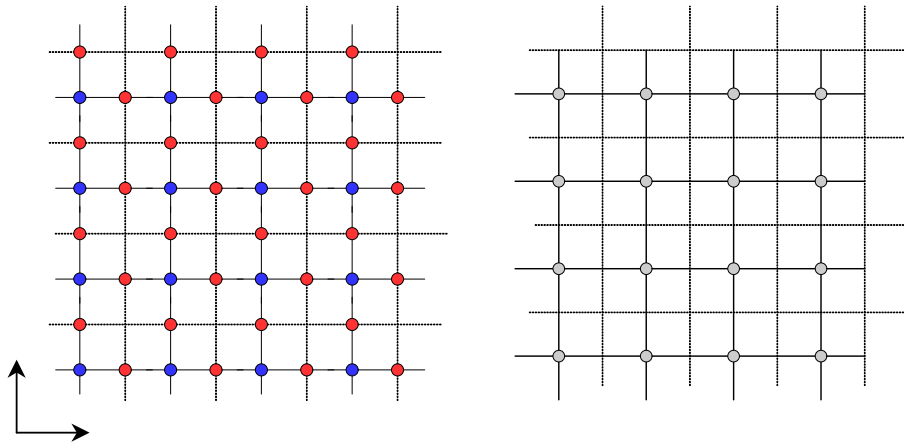
Figure 2.3: Asymmetric formulation in two dimensions. Left tensor network shows the original one constructed by A_ℓ's and $B_\square$'s. Right one is a tensor network given by $\mathcal{T}_c$'s. Although each $\mathcal{T}_c$ lives on a plaquette, not on a site, the geometry is same to the network in Fig. 2.1.
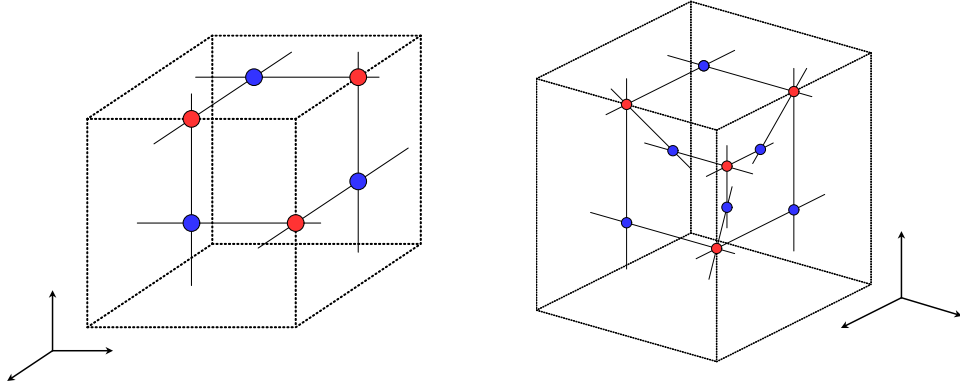
Figure 2.4: (Left) Asymmetric formulation in three dimensions. Red symbol shows a link tensor A_ℓ and blue one does a plaquette tensor $B_\square$. Dotted lines show a cubic lattice. $\mathcal{T}_c$ is given by three A_ℓ's and three $B_\square$'s. (Right) Four-dimensional asymmetric formulation. Dotted lines show a three-dimensional sub-lattice. "Skewed" lines in A_ℓ's and $B_\square$'s correspond to subscripts along the rest of one direction in the four-dimensional total lattice.
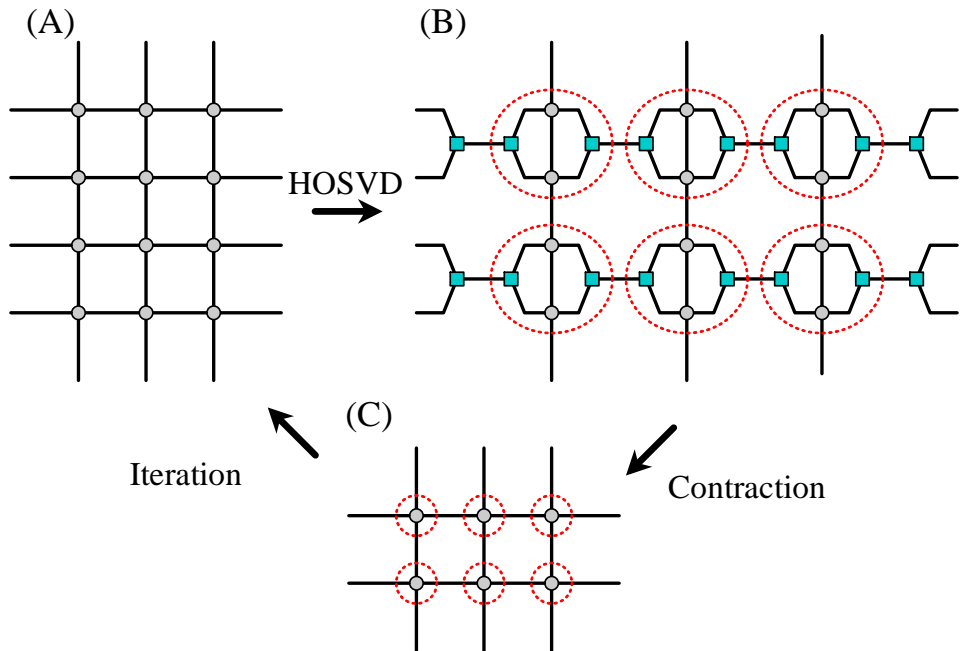
Figure 2.5: Schematic illustration of HOTRG. (A) Local tensors construct tensor network representation. (B) HOSVD introduces the optimal approximation for each subnetwork, which is consist of two adjacent tensors. (C) After the contraction, the lattice size is reduced by a factor of 2.

2.2.1 Higher-order tensor renormalization group

We review the numerical algorithm of the HOTRG based on Ref. [XCQ$^+$12]. The HOTRG provides us with a way to approximately carry out tensor contractions in Eq. (2.12) via inserting isometries. Fig. 2.5 is a schematic illustration of the algorithm. The HOTRG focuses on a contraction between two adjacent tensors, which is a "subnetwork" in Eq. (2.12), say,

$$\sum_{i_1(n)} \mathcal{T}_{i_1(n+\hat{1})\cdots i_d(n+\hat{1})i_1(n)\cdots i'_d(n+\hat{1})} \mathcal{T}_{i_1(n)\cdots i_d(n)i'_1(n)\cdots i'_d(n)}, \tag{2.27}$$

where we have considered a subnetwork made by two tensors living on sites $n, n + \hat{1} \in \Lambda_d$. Note that $i'_\nu(n + \hat{\nu}) = i_\nu(n)$ holds in our notation. If we naively implement the contraction of Eq. (2.27), we encounter a $2(2d-1)$-rank tensor, which is a higher-rank tensor compared with $\mathcal{T}$, so it is impossible to iterate such a naive contraction. Instead of Eq. (2.27), the HOTRG carries out a contraction such that

$$\sum_{i_1(n)} \sum_{\substack{\text{subscripts} \\ \text{except } i_1(n),\{j_\nu\},\{j'_\nu\}}} \mathcal{T}_{i_1(n+\hat{1})\cdots i_d(n+\hat{1})i_1(n)\cdots i'_d(n+\hat{1})} \mathcal{T}_{i_1(n)\cdots i_d(n)i'_1(n)\cdots i'_d(n)} \prod_{\nu\neq 1} U^{(\nu)}_{i_\nu(n+\hat{1})i_\nu(n),j_\nu} U^{(\nu)*}_{i'_\nu(n+\hat{1})i'_\nu(n),j'_\nu}, \tag{2.28}$$

where $U^{(\nu)}$'s are so-called isometries satisfying

$$\sum_{ab} U^{(\nu)}_{ab,c} U^{(\nu)*}_{ab,c'} = \delta_{cc'}. \tag{2.29}$$

δ denotes Kronecker's delta. In the practical calculation, we restrict the size of c in order to introduce a low-rank approximation of Eq. (2.27). The restricted size of c is called a bond dimension, which characterizes a maximal size of tensors treated within the TRG algorithms. When the bond dimension is set to be D ($\in \mathbb{N}$), then all subscripts appearing in the HOTRG runs up to D at most. Therefore, $U^{(\nu)}$'s are $D^2 \times D$ matrices, at most. If c is allowed to run up to D^2, then one can make $U^{(\nu)}$ a unitary matrix, so Eq. (2.28) becomes equal to Eq. (2.27) with inserting identities. In other words, we can systematically control the accuracy of HOTRG varying the bond dimension D. As a result of Eq. (2.28), one obtains a $2d$-rank tensor $\mathcal{T}'_{j_1\cdots j_d j'_1\cdots j'_d}$. Since the rank of $\mathcal{T}'$ is equal to that of $\mathcal{T}$, there is no difficulty in repeating the renormalization-group transformation of Eq. (2.28), varying the direction in which it takes place.

Now, our task is to derive proper $U^{(\nu)}$'s. This task is accomplished by the HOSVD of Eq. (2.27) in the HOTRG algorithm. However, a direct HOSVD requires a very large amount of memory space to hold the $2(2d-1)$-rank tensor of Eq. (2.27), so we need to implement the HOSVD indirectly. We then consider an eigenvalue decomposition (EVD), which becomes equivalent to a certain step of the HOSVD. To see it, let us focus on the procedure to derive $U^{(2)}$ as an example. Firstly, we carry out the following contraction,

$$(\mathcal{T}\mathcal{T}^*)_{i_2(n+\hat{1})\tilde{i}_2(n+\hat{1})i_1(n)\tilde{i}_1(n)} = \sum \mathcal{T}_{i_1(n+\hat{1})i_2(n+\hat{1})\cdots i_d(n+\hat{1})i_1(n)\cdots i'_d(n+\hat{1})} \mathcal{T}^*_{i_1(n+\hat{1})\tilde{i}_2(n+\hat{1})\cdots i_d(n+\hat{1})\tilde{i}_1(n)\cdots i'_d(n+\hat{1})}. \tag{2.30}$$

---

[2]It may be interesting to consider an efficient TRG algorithm to evaluate the tensor network generated by link tensors and plaquette tensors, directly.

[3]Regularization of continuous gauge groups (or non-compact fields) is also necessary when we consider a quantum computation of such quantum field theories. Therefore, the development of an efficient regularization scheme has been a recent hot topic in the community.

In the right-hand side, the subscripts appearing twice are summed. The resulting tensor is of four-rank, which is less than or equal to the rank of $\mathcal{T}$. Similarly, we also carry out a contraction,

$$(\mathcal{T}\mathcal{T}^*)_{i_2(n)\tilde{i}_2(n)i_1(n)\tilde{i}_1(n)} = \sum \mathcal{T}_{i_1(n)i_2(n)\cdots i_d(n)i'_1(n)\cdots i'_d(n)} \mathcal{T}^*_{\tilde{i}_1(n)\tilde{i}_2(n)\cdots i_d(n)i'_1(n)\cdots i'_d(n)}, \tag{2.31}$$

whose rank is also four. [4] Next, we contract Eqs. (2.30) and (2.31) as

$$(\mathcal{T}\mathcal{T}\mathcal{T}^*\mathcal{T}^*)_{i_2(n+\hat{1})i_2(n)\tilde{i}_2(n+\hat{1})\tilde{i}_2(n)} = \sum (\mathcal{T}\mathcal{T}^*)_{i_2(n+\hat{1})\tilde{i}_2(n+\hat{1})i_1(n)\tilde{i}_1(n)} (\mathcal{T}\mathcal{T}^*)_{i_2(n)\tilde{i}_2(n)i_1(n)\tilde{i}_1(n)}. \tag{2.32}$$

Then the EVD of Eq. (2.32) gives us

$$(\mathcal{T}\mathcal{T}\mathcal{T}^*\mathcal{T}^*)_{i_2(n+\hat{1})i_2(n)\tilde{i}_2(n+\hat{1})\tilde{i}_2(n)} = \sum_m P^{(2)}_{i_2(n+\hat{1})i_2(n),m} \lambda^{(2)}_m P^{(2)*}_{\tilde{i}_2(n+\hat{1})\tilde{i}_2(n),m}. \tag{2.33}$$

Since all λ_m's take non-negative values, we sort them in descending order. We repeat from Eq. (2.30) to Eq. (2.32) with respect to i'_2's. As a result of this, we have a four-rank tensor , whose EVD also gives us

$$(\mathcal{T}\mathcal{T}\mathcal{T}^*\mathcal{T}^*)_{i'_2(n+\hat{1})i'_2(n)\tilde{i}'_2(n+\hat{1})\tilde{i}'_2(n)} = \sum_m Q^{(2)}_{i'_2(n+\hat{1})i'_2(n),m} \lambda^{(2)'}_m Q^{(2)*}_{\tilde{i}'_2(n+\hat{1})\tilde{i}'_2(n),m}. \tag{2.34}$$

We also sort λ'_m's in descending order. $P^{(2)}$ and $Q^{(2)}$ are candidates of $U^{(2)}$. A proper $U^{(2)}$ is decided via checking a quantity defined as

$$\epsilon^{(2)} = \left(\sum_{m=1}^{D} \lambda^{(2)}_m \right) - \left(\sum_{m=1}^{D} \lambda^{(2)'}_m \right). \tag{2.35}$$

When $\epsilon^{(2)} > 0$ ($\epsilon^{(2)} < 0$) then we choose $P^{(2)}$ ($Q^{(2)}$) as $U^{(2)}$. This is because

$$\text{Tr}\left[\mathcal{T}\mathcal{T}\mathcal{T}^*\mathcal{T}^* \right] - \left(\sum_{m=1}^{D} \lambda^{(2)(')}_m \right) \tag{2.36}$$

estimates a fidelity, where $\text{Tr}\left[\mathcal{T}\mathcal{T}\mathcal{T}^*\mathcal{T}^* \right]$ corresponds to the squared Frobenius norm of $\mathcal{T}\mathcal{T}$. The smaller the value of Eq. (2.36) is, the better the finite-D approximation works. Repeating the above procedure for all ν except $\nu = 1$, then all the isometries in Eq. (2.28) are obtained via checking $\epsilon^{(\nu)}$'s.

The computational complexity of the HOTRG is characterized by the bond dimension D and the dimensionality d. [5] The memory footprint scales with $\mathcal{O}(D^{2d})$ and the computational time scales with $\mathcal{O}(D^{4d-1})$. The bottleneck of the algorithm is the contraction of Eq. (2.28), whose execution time can be reduced by parallel computation. The parallelized HOTRG algorithm is demonstrated in detail in Ref. [YS21].

2.2.2   Anisotropic tensor renormalization group

The ATRG algorithm was originally introduced by Adachi, Okubo, and Todo in Ref. [AOT20a]. Here, we would like to review the algorithm with some modifications based on Refs. [AOT20a, Oba20, AKYY20, AKK$^+$20]. The ATRG also provides us with a way to approximately carry out tensor contractions in Eq. (2.12), but with much less computational complexity compared with the HOTRG. Fig. 2.6 is a schematic illustration of the algorithm.

---

[4]In Eqs. (2.30) and (2.31), tensors with different subscripts are assumed to represent different tensors.

[5]It is linearly that the computational cost scales with the iteration number.
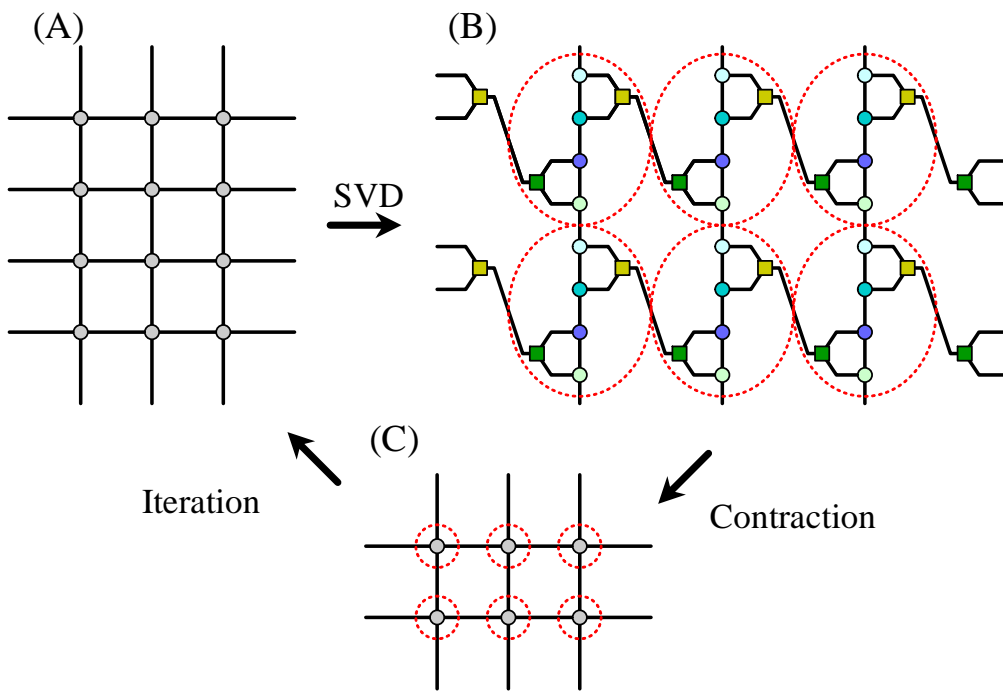
Figure 2.6: Schematic illustration of ATRG. (A) Local tensors construct tensor network representation. (B) SVD for local tensor introduces the extra approximation compared with HOTRG. (C) After the contraction, the lattice size is reduced by a factor of 2.

As in the HOTRG, the ATRG focuses on the subnetwork of Eq. (2.27), but we begin with considering a low-rank approximation of $\mathcal{T}$ itself before we apply a certain renormalization-group transformation. Instead of Eq. (2.27), the ATRG considers

$$\sum_{i_1(n),\alpha,\beta} \mathcal{A}_{i_1(n+\hat{1})\cdots i_d(n+\hat{1})\alpha} \mathcal{B}_{i_1(n)\cdots i'_d(n+\hat{1})\alpha} \mathcal{C}_{i_1(n)\cdots i_d(n)\beta} \mathcal{D}_{i'_1(n)\cdots i'_d(n)\beta}, \tag{2.37}$$

where all tensors are of rank $d+1$. These tensors are defined via the SVD [6] of $\mathcal{T}$ such that

$$\mathcal{A}_{i_1(n+\hat{1})\cdots i_d(n+\hat{1})\alpha} = U[\mathcal{T}]_{i_1(n+\hat{1})\cdots i_d(n+\hat{1}),\alpha}, \tag{2.38}$$

$$\mathcal{B}_{i_1(n)\cdots i'_d(n+\hat{1})\alpha} = V^*[\mathcal{T}]_{i_1(n)\cdots i'_d(n+\hat{1}),\alpha}\sigma[\mathcal{T}]_\alpha, \tag{2.39}$$

$$\mathcal{C}_{i_1(n)\cdots i_d(n)\beta} = U[\mathcal{T}]_{i_1(n)\cdots i_d(n),\beta}\sigma[\mathcal{T}]_\beta, \tag{2.40}$$

$$\mathcal{D}_{i'_1(n)\cdots i'_d(n)\beta} = V^*[\mathcal{T}]_{i'_1(n)\cdots i'_d(n),\beta}, \tag{2.41}$$

with

$$\mathcal{T}_{i_1\cdots i_d,i'_1\cdots i'_d} \approx \sum_{\alpha=1}^{D} U[\mathcal{T}]_{i_1\cdots i_d,\alpha}\sigma[\mathcal{T}]_\alpha V^*[\mathcal{T}]_{i'_1\cdots i'_d,\alpha}. \tag{2.42}$$

To accomplish a renormalization-group transformation just within these $(d+1)$-rank tensors, we swap some subscripts between $\mathcal{B}$ and $\mathcal{C}$ via the truncated SVD,

$$\sum_{i_1(n)} \mathcal{B}_{i_1(n)i'_2(n+\hat{1})\cdots i'_d(n+\hat{1})\alpha} \mathcal{C}_{i_1(n)i_2(n)\cdots i_d(n)\beta} \approx \sum_{\gamma=1}^{D} U[\mathcal{B}\mathcal{C}]_{i_2(n)\cdots i_d(n)\alpha,\gamma}\sigma[\mathcal{B}\mathcal{C}]_\gamma V^*[\mathcal{B}\mathcal{C}]_{i'_2(n+\hat{1})\cdots i'_d(n+\hat{1})\beta,\gamma}. \tag{2.43}$$

However, a direct implementation of Eq. (2.43) is hindered both by the memory cost and the complexity. Here, we make a pretreatment for Eq. (2.43) proposed in Ref. [Oba20] before we carry out an economic SVD algorithm to reduce the computational cost of Eq. (2.43). Fig. 2.7 summarizes the following procedure. As a pretreatment for Eq. (2.43), we carry out the QR decomposition both for $\mathcal{B}$ and $\mathcal{C}$ in advance.

$$\mathcal{B}_{i_1(n)i'_2(n+\hat{1})\cdots i'_d(n+\hat{1})\alpha} = \sum_p Q[\mathcal{B}]_{i'_2(n+\hat{1})\cdots i'_d(n+\hat{1}),p} R[\mathcal{B}]_{i_1(n)\alpha,p}, \tag{2.44}$$

$$\mathcal{C}_{i_1(n)i_2(n)\cdots i_d(n)\beta} = \sum_q Q[\mathcal{C}]_{i_2(n)\cdots i_d(n),q} R[\mathcal{C}]_{i_1(n)\beta,q}. \tag{2.45}$$

Note that p and q run up to $D^{\min(d-1,2)}$, at most. Using these R's, we define

$$\mathcal{M}_{\alpha q\beta p} = \sum_{i_1(n)} R[\mathcal{B}]_{i_1(n)\alpha,p} R[\mathcal{C}]_{i_1(n)\beta,q}, \tag{2.46}$$

---

[6]For a while, we denote the SVD of a matrix A as $A = \sum U[A]\sigma[A]V^*[A]$ to save symbols. We also use similar notations for matrix decompositions, such as the EVD and the QR decomposition.
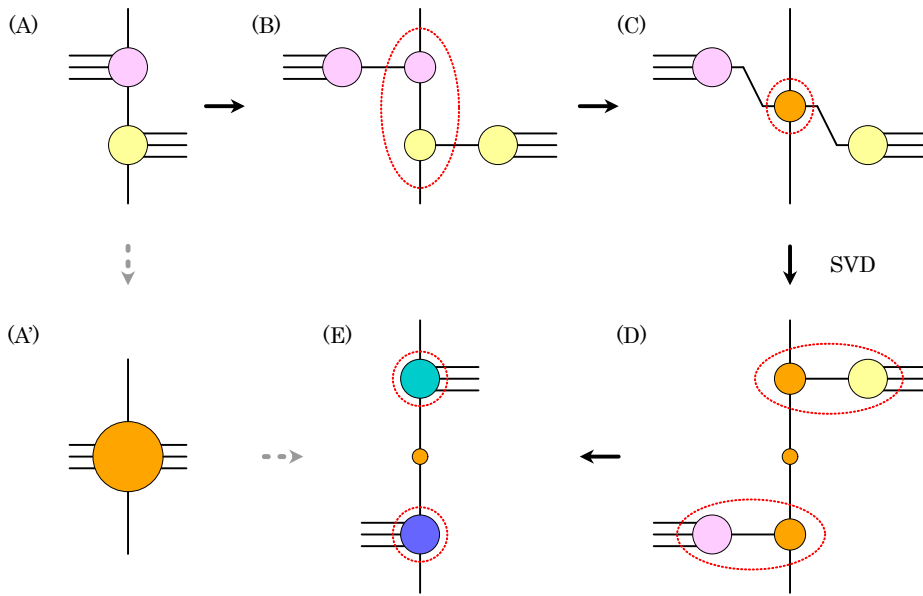
Figure 2.7: Schematic illustration of the subscript-swapping procedure in Ref. [Oba20] in four dimensions. (A) and (A') show the left-hand side of Eq. (2.43). We cannot have a tensor shown in (A') because of the required memory. (B) QR decompositions of $\mathcal{B}$ and $\mathcal{C}$ in Eqs. (2.44) and (2.45). (C) Orange symbol denotes $\mathcal{M}$ in Eq. (2.46). (D) Truncated SVD of $\mathcal{M}$ as in Eq. (2.47). (E) One restores $U[\mathcal{BC}]$ and $V^{\dagger}[\mathcal{BC}]$ like in Eqs. (2.48) and (2.49). This results in the SVD of (A'), that is, the procedure from (A) to (E) (shown by solid arrows) is equivalent to the procedure (A)$\rightarrow$(A')$\rightarrow$(E) (shown by dotted arrows).

whose SVD provides us with

$$\mathcal{M}_{\alpha q \beta p} \approx \sum_{\gamma=1}^{D} U[\mathcal{M}]_{\alpha q, \gamma} \sigma[\mathcal{M}]_{\gamma} V^*[\mathcal{M}]_{\beta p, \gamma}. \tag{2.47}$$

Then we can obtain the matrices in the right-hand side of Eq. (2.43) as

$$U[\mathcal{BC}]_{i_2(n)\cdots i_d(n)\alpha, \gamma} = \sum_{q} Q[\mathcal{C}]_{i_2(n)\cdots i_d(n), q} U[\mathcal{M}]_{\alpha q, \gamma}, \tag{2.48}$$

$$V^*[\mathcal{BC}]_{i'_2(n+\hat{1})\cdots i'_d(n+\hat{1})\beta, \gamma} = \sum_{p} Q[\mathcal{B}]_{i'_2(n+\hat{1})\cdots i'_d(n+\hat{1}), p} V^*[\mathcal{M}]_{\beta p, \gamma}, \tag{2.49}$$

and $\sigma[\mathcal{BC}]_{\gamma} = \sigma[\mathcal{M}]_{\gamma}$. Although the computational complexity of the naive SVD in Eq. (2.43) scales with $\mathcal{O}(D^{3d})$, the SVD of Eq. (2.47) requires the complexity whose scaling is $\mathcal{O}(D^{3\min(d,3)})$, which is smaller than $\mathcal{O}(D^{3d})$ with $d \geq 4$. Therefore, the pretreatment in Ref. [Oba20] is of practical importance when we apply the ATRG algorithm to four-dimensional field theories. The second trick we explain is an economic SVD algorithm. Such an economic SVD algorithm is necessary because the subscript-swapping procedure can be the bottleneck of the ATRG as pointed out in the original paper [AOT20a]. In addition, the memory cost of $\mathcal{M}$ scales with $\mathcal{O}(D^{2\min(d,3)})$, which can be larger than the memory footprints of initial tensors in Eq. (2.37). Here, we employ the so-called randomized SVD (RSVD) algorithm as an economic SVD. The first application of the RVD to the TRG approach was presented in Ref. [MIZK18]. The RSVD algorithm allows us to obtain the right-hand side of Eq. (2.47) without making $\mathcal{M}$ explicitly. There are two parameters which control the accuracy of the RSVD. One is the oversampling parameter and the other is the iteration number of QR decomposition in the algorithm. Denoting the later parameter by q, the total computational complexity of the subscript-swapping procedure scales with $\mathcal{O}(qD^{\min(d+3,6)})$. We explain algorithmic details about the subscript-swapping procedure with the RSVD in Appendix A.

Our next task is to derive so-called squeezers, which play a similar role of isometries in the HOTRG algorithm, but they do not need to satisfy the orthogonal condition as in Eq. (2.29). The renormalization-group transformation in the ATRG is accomplished by

$$\sum_{\substack{\text{subscripts} \\ \text{except } i_1(n+\hat{1}),\gamma,\{j_\nu\}}} \mathcal{A}_{i_1(n+\hat{1})i_2(n+\hat{1})\cdots i_d(n+\hat{1})\alpha} U[\mathcal{BC}]_{i_2(n)\cdots i_d(n)\alpha, \gamma} \sigma[\mathcal{BC}]_{\gamma} \prod_{\nu\neq 1} E^{(\nu)}_{i_\nu(n+\hat{1})i_\nu(n),j_\nu}, \tag{2.50}$$

and

$$\sum_{\substack{\text{subscripts} \\ \text{except } i'_1(n),\gamma,\{j'_\nu\}}} V^*[\mathcal{BC}]_{i'_2(n+\hat{1})\cdots i'_d(n+\hat{1})\beta, \gamma} \mathcal{D}_{i'_1(n)i'_2(n)\cdots i'_d(n)\beta} \prod_{\nu\neq 1} F^{(\nu)}_{i'_\nu(n+\hat{1})i'_\nu(n),j'_\nu}, \tag{2.51}$$

with the squeezers $E^{(\nu)}$'s and $F^{(\nu)}$'s, which are $D^2 \times D$ matrices, at most. In Eqs. (2.50) and (2.51), we have introduced some modification on the original ATRG algorithm. In the original ATRG, one takes a square root of $\sigma[\mathcal{BC}]$, which is equally assigned to Eqs. (2.50) and (2.51). A square root of $\sigma[\mathcal{BC}]$ can be avoided, however, by modifying how to derive $E^{(\nu)}$'s and $F^{(\nu)}$'s as we explain in the following. Note that this modification was first applied in Ref. [AKK$^+$20]. We focus on the derivation of $E^{(2)}$ and $F^{(2)}$ but it is easily extended to the cases of $E^{(\nu)}$'s and $F^{(\nu)}$'s for any ν except $\nu = 1$. Fig. 2.8 shows a procedure to derive squeezers explained below. Let us consider the tensors such as

$$(\mathcal{A}\mathcal{A}^*)_{i_2(n+\hat{1})\tilde{i}_2(n+\hat{1})\alpha\tilde{\alpha}} = \sum \mathcal{A}_{i_1(n+\hat{1})i_2(n+\hat{1})\cdots i_d(n+\hat{1})\alpha} \mathcal{A}_{i_1(n+\hat{1})\tilde{i}_2(n+\hat{1})\cdots i_d(n+\hat{1})\tilde{\alpha}}, \tag{2.52}$$
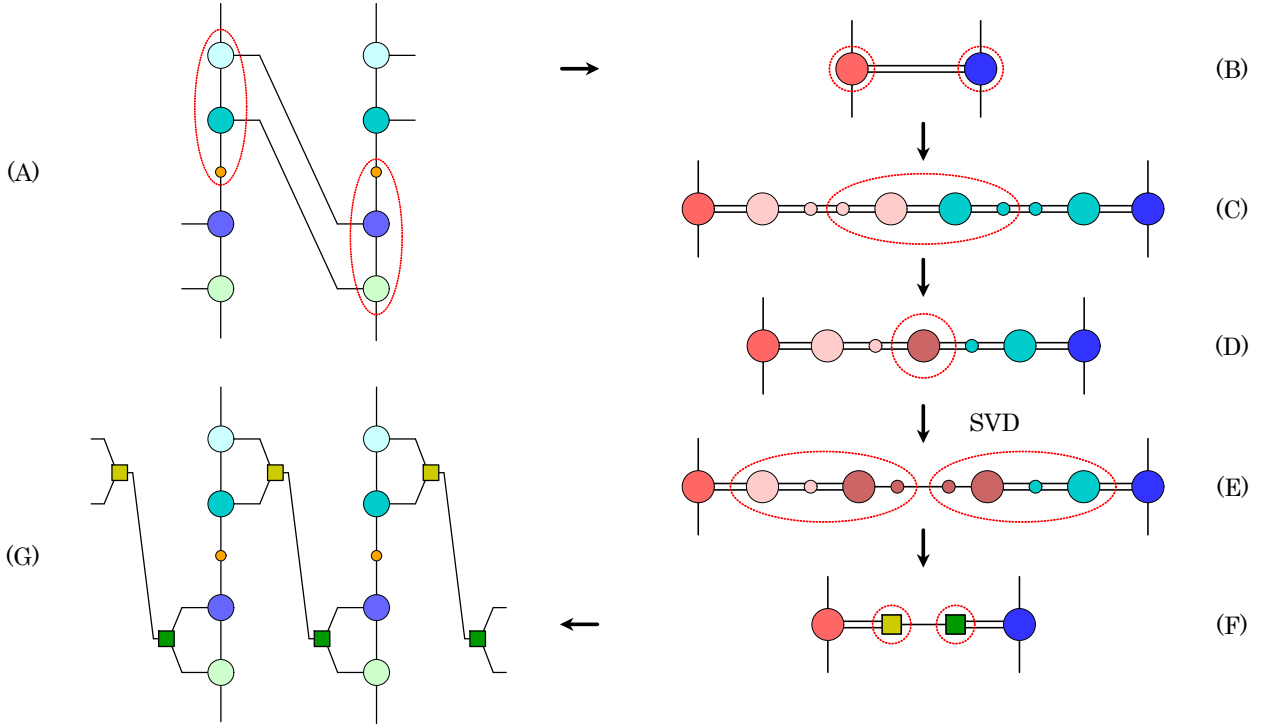
Figure 2.8: Schematic illustration of how to derive squeezers in two dimensions. (A) Subnetwork we have after the subscript-swapping procedure. Each symbol corresponds to $\mathcal{A}$, $U[\mathcal{BC}]$, $\sigma[\mathcal{BC}]$, $V^{\dagger}[\mathcal{BC}]$, and $\mathcal{D}$ at $n+\hat{1}$, n, and $n+\hat{1}+\hat{2}$, $n+\hat{2}$. (B) One considers the SVD of $\mathcal{A}(U\sigma)[\mathcal{BC}]$ and that of $(\sigma V^{\dagger}[\mathcal{BC}])\mathcal{D}$. (C) Eq. (2.61) obtained by inserting $(U\sigma\sigma^{-1}U^{\dagger})[\mathcal{A}(U\sigma)[\mathcal{BC}]]$ and $(U\sigma\sigma^{-1}U^{\dagger})[\mathcal{D}(V^{*}\sigma)[\mathcal{BC}]]$ into Eq. (2.60). (D) Symbol in the red dotted circle shows S in Eq. (2.62). (E) SVD of S in the right-hand side of Eq. (2.62). (F) Yellow symbol shows Eq. (2.64) and green one does Eq. (2.65). (G) We insert the squeezers obtained in Eqs. (2.64) and (2.65) into the tensor network of (A).

$$((U\sigma)[\mathcal{BC}](U^*\sigma)[\mathcal{BC}])_{i_2(n)\tilde{i}_2(n)\alpha\tilde{\alpha}} = \sum (U\sigma)[\mathcal{BC}]_{i_2(n)\cdots i_d(n)\alpha,\gamma}(U^*\sigma)[\mathcal{BC}]_{\tilde{i}_2(n)\cdots i_d(n)\tilde{\alpha},\gamma}, \tag{2.53}$$

$$((V^*\sigma)[\mathcal{BC}](V\sigma)[\mathcal{BC}])_{i'_2(n+\hat{1})\tilde{i}'_2(n+\hat{1})\beta\tilde{\beta}} = \sum (V^*\sigma)[\mathcal{BC}]_{i'_2(n+\hat{1})\cdots i'_d(n+\hat{1})\beta,\gamma}(V\sigma)[\mathcal{BC}]_{\tilde{i}'_2(n+\hat{1})\cdots i'_d(n+\hat{1})\tilde{\beta},\gamma}, \tag{2.54}$$

$$(\mathcal{D}\mathcal{D}^*)_{i'_2(n)\tilde{i}'_2(n)\beta\tilde{\beta}'} = \sum \mathcal{D}_{i'_1(n)i'_2(n)\cdots i'_d(n)\beta}\mathcal{D}_{i'_1(n)\tilde{i}'_2(n)\cdots i'_d(n)\tilde{\beta}}, \tag{2.55}$$

where we have assumed that the subscripts appearing twice or more are contracted under $\sum$'s. We have also used a shorthand notation, $(U\sigma)[\mathcal{BC}] = U[\mathcal{BC}]\sigma[\mathcal{BC}]$, and so on. We then combine these tensors in the two ways,

$$(\mathcal{A}(U\sigma)[\mathcal{BC}](U^*\sigma)[\mathcal{BC}]\mathcal{A}^*)_{i_2(n+\hat{1})i_2(n)\tilde{i}_2(n+\hat{1})\tilde{i}_2(n)}$$
$$= \sum (\mathcal{A}\mathcal{A}^*)_{i_2(n+\hat{1})\tilde{i}_2(n+\hat{1})\alpha\tilde{\alpha}}((U\sigma)[\mathcal{BC}](U^*\sigma)[\mathcal{BC}])_{i_2(n)\tilde{i}_2(n)\alpha\tilde{\alpha}}, \tag{2.56}$$

$$(\mathcal{D}(V^*\sigma)[\mathcal{BC}](V\sigma)[\mathcal{BC}]\mathcal{D}^*)_{i'_2(n+\hat{1})i'_2(n)\tilde{i}'_2(n+\hat{1})\tilde{i}'_2(n)}$$
$$= \sum ((V^*\sigma)[\mathcal{BC}](V\sigma)[\mathcal{BC}])_{i'_2(n+\hat{1})\tilde{i}'_2(n+\hat{1})\beta\tilde{\beta}}(\mathcal{D}\mathcal{D}^*)_{i'_2(n)\tilde{i}'_2(n)\beta\tilde{\beta}'}. \tag{2.57}$$

We carry out the EVD of Eq. (2.56),

$$(\mathcal{A}(U\sigma)[\mathcal{BC}](U^*\sigma)[\mathcal{BC}]\mathcal{A}^*)_{i_2(n+\hat{1})i_2(n)\tilde{i}_2(n+\hat{1})\tilde{i}_2(n)}$$
$$= \sum_p U[\mathcal{A}(U\sigma)[\mathcal{BC}]]_{i_2(n+\hat{1})i_2(n),p}\sigma^2[\mathcal{A}(U\sigma)[\mathcal{BC}]]_p U^*[\mathcal{A}(U\sigma)[\mathcal{BC}]]_{\tilde{i}_2(n+\hat{1})\tilde{i}_2(n),p}, \tag{2.58}$$

Although Eq. (2.58) is the EVD of Eq. (2.56), this is equivalent to the SVD of $\mathcal{A}(U\sigma)[\mathcal{BC}]$. Therefore, Eq. (2.58) provides us with $U[\mathcal{A}(U\sigma)[\mathcal{BC}]]$ and the squared singular value $\sigma^2[\mathcal{A}(U\sigma)[\mathcal{BC}]]$. Similarly, the EVD of Eq. (2.57) gives us

$$(\mathcal{D}(V^*\sigma)[\mathcal{BC}](V\sigma)[\mathcal{BC}]\mathcal{D}^*)_{i'_2(n+\hat{1})i'_2(n)\tilde{i}'_2(n+\hat{1})\tilde{i}'_2(n)}$$
$$= \sum_q U[\mathcal{D}(V^*\sigma)[\mathcal{BC}]]_{i'_2(n+\hat{1})i'_2(n),q}\sigma^2[\mathcal{D}(V^*\sigma)[\mathcal{BC}]]_q U^*[\mathcal{D}(V^*\sigma)[\mathcal{BC}]]_{\tilde{i}'_2(n+\hat{1})\tilde{i}'_2(n),q}. \tag{2.59}$$

Now, let us consider a subnetwork constructed by $\mathcal{A}(U\sigma)[\mathcal{BC}]$ on the lattice sites $n + \hat{1}, n$ and $\mathcal{D}(V^*\sigma)[\mathcal{BC}]$ on $n + \hat{1} + \hat{2}, n + \hat{2}$. This subnetwork is written as

$$\sum_{i_2(n+\hat{1}),i_2(n)} \mathcal{A}(U\sigma)[\mathcal{BC}]_{i_2(n+\hat{1})i_2(n)i_1(n+\hat{1})i_3(n+\hat{1})i_3(n)\cdots i_d(n+\hat{1})i_d(n)\alpha}$$
$$\times \mathcal{D}(V^*\sigma)[\mathcal{BC}]_{i_2(n+\hat{1})i_2(n)i'_1(n+\hat{2})i'_3(n+\hat{1}+\hat{2})i'_3(n+\hat{2})\cdots i'_d(n+\hat{1}+\hat{2})i'_d(n+\hat{2})\beta}. \tag{2.60}$$

Inserting $(U\sigma\sigma^{-1}U^\dagger)[\mathcal{A}(U\sigma)[\mathcal{BC}]]$ and $(U\sigma\sigma^{-1}U^\dagger)[\mathcal{D}(V^*\sigma)[\mathcal{BC}]]$ into Eq. (2.60),

$$\sum_{i_2(n+\hat{1}),i_2(n)} \sum_{\tilde{i}_2(n+\hat{1}),\tilde{i}_2(n)} \sum_{\tilde{\tilde{i}}_2(n+\hat{1}),\tilde{\tilde{i}}_2(n)} \sum_{p,q}$$
$$\times (U\sigma)[\mathcal{A}(U\sigma)[\mathcal{BC}]]_{i_2(n+\hat{1})i_2(n),p}(U^*\sigma^{-1})[\mathcal{A}(U\sigma)[\mathcal{BC}]]_{\tilde{i}_2(n+\hat{1})\tilde{i}_2(n),p}$$
$$\times \mathcal{A}(U\sigma)[\mathcal{BC}]_{\tilde{i}_2(n+\hat{1})\tilde{i}_2(n)i_1(n+\hat{1})i_3(n+\hat{1})i_3(n)\cdots i_d(n+\hat{1})i_d(n)\alpha}$$
$$\times (U\sigma)[\mathcal{D}(V^*\sigma)[\mathcal{BC}]]_{i_2(n+\hat{1})i_2(n),q}(U^*\sigma^{-1})[\mathcal{D}(V^*\sigma)[\mathcal{BC}]]_{\tilde{\tilde{i}}_2(n+\hat{1})\tilde{\tilde{i}}_2(n),q}$$
$$\times \mathcal{D}(V^*\sigma)[\mathcal{BC}]_{\tilde{\tilde{i}}_2(n+\hat{1})\tilde{\tilde{i}}_2(n)i'_1(n+\hat{2})i'_3(n+\hat{1}+\hat{2})i'_3(n+\hat{2})\cdots i'_d(n+\hat{1}+\hat{2})i'_d(n+\hat{2})\beta}. \tag{2.61}$$

Note that the second and third lines in Eq. (2.61) correspond to the SVD of $\mathcal{A}(U\sigma)[\mathcal{BC}]$. Similarly, the last two lines give us the SVD of $\mathcal{D}(V^*\sigma)[\mathcal{BC}]$. In Eq. (2.61), we set

$$S_{pq} = \sum_{i_2(n+\hat{1}),i_2(n)} (U\sigma)[\mathcal{A}(U\sigma)[\mathcal{BC}]]_{i_2(n+\hat{1})i_2(n),p}(U\sigma)[\mathcal{D}(V^*\sigma)[\mathcal{BC}]]_{i_2(n+\hat{1})i_2(n),q}, \tag{2.62}$$

whose SVD with a truncation provides us with

$$S_{pq} \approx \sum_{j_2=1}^{D} U[S]_{p,j_2}\sigma[S]_{j_2}V^*[S]_{q,j_2}. \tag{2.63}$$

Substituting this decomposition back into Eq. (2.61), one obtains an approximation of Eq. (2.60) with the squeezers $E^{(2)}$ and $F^{(2)}$ defined via

$$E^{(2)}_{i_2(n+\hat{1})i_2(n),j_2} = \sum_{p}(U^*\sigma^{-1})[\mathcal{A}(U\sigma)[\mathcal{BC}]]_{i_2(n+\hat{1})i_2(n),p}U[S]_{p,j_2}\sqrt{\sigma[S]}_{j_2}, \tag{2.64}$$

$$F^{(2)}_{i_2(n+\hat{1})i_2(n),j_2} = \sum_{q}(U^*\sigma^{-1})[\mathcal{D}(V^*\sigma)[\mathcal{BC}]_{i_2(n+\hat{1})i_2(n),q}V^*[S]_{q,j_2}\sqrt{\sigma[S]}_{j_2}. \tag{2.65}$$

One should notice that $E^{(2)}$ and $F^{(2)}$ realize an indirect SVD of Eq. (2.60), "looking at" the Frobenius norms of adjacent $(\mathcal{BC})$'s, which have been approximated via subscript-swapping procedure. In this sense, the ATRG algorithm introduces the approximation, looking at a wider subnetwork than the HOTRG does. Since we have considered $\mathcal{D}(V^*\sigma)[\mathcal{BC}]$ on $n+\hat{1}+\hat{2}, n+\hat{2}$ in Eq. (2.60), that on $n+\hat{1}$ and n defined $F^{(2)}$ in Eq. (2.51). Repeating the derivation below Eq. (2.52) for all ν, we can obtain all $E^{(\nu)}$'s and $F^{(\nu)}$'s.

Notice that the current ATRG computation starts with four types of tensor in Eq. (2.37), but we have just two kinds of tensor as the result of renormalization-group transformation, as in Eqs. (2.50) and (2.51). To iterate the above procedure, we make some transformations for the results of Eqs. (2.50) and (2.51). Setting the result of Eq. (2.50) be $\mathcal{G}_{i_1 j_2 \cdots j_d \gamma}$ and that of Eq. (2.51) be $\mathcal{H}_{i_1' j_2' \cdots j_d' \gamma}$, we perform QR decompositions both for $\mathcal{G}$ and $\mathcal{H}$ as

$$\mathcal{G}_{i_1 j_2 \cdots j_d \gamma} = \sum_{p} Q[\mathcal{G}]_{i_1 j_2 \cdots j_d,p}R[\mathcal{G}]_{\gamma,p}, \tag{2.66}$$

$$\mathcal{H}_{i_1' j_2' \cdots j_d' \gamma} = \sum_{q} Q[\mathcal{H}]_{i_1' j_2' \cdots j_d',q}R[\mathcal{H}]_{\gamma,q}. \tag{2.67}$$

Carrying out the SVD of

$$K_{pq} = \sum_{\gamma} R[\mathcal{G}]_{\gamma,p}R[\mathcal{H}]_{\gamma,q}, \tag{2.68}$$

without any decimation, we obtain new four types of tensor as

$$\mathcal{A}_{i_1 j_2 \cdots j_d \alpha} = \sum_{p} Q[\mathcal{G}]_{i_1 j_2 \cdots j_d,p}U[K]_{p,\alpha} \tag{2.69}$$

$$\mathcal{B}_{i_1' j_2' \cdots j_d' \alpha} = \sum_{q} Q[\mathcal{H}]_{i_1' j_2' \cdots j_d',q}V^*[K]_{q,\alpha}\sigma[K]_{\alpha}, \tag{2.70}$$

$$\mathcal{C}_{i_1 j_2 \cdots j_d \beta} = \sum_p Q[\mathcal{G}]_{i_1 j_2 \cdots j_d, p} U[K]_{p,\beta} \sigma[K]_\beta, \tag{2.71}$$

$$\mathcal{D}_{i'_1 j'_2 \cdots j'_d \beta} = \sum_q Q[\mathcal{H}]_{i'_1 j'_2 \cdots j'_d, q} V^*[K]_{q,\beta}. \tag{2.72}$$

As another remark, we can regard the combination of $\mathcal{G}$ and $\mathcal{H}$,

$$\sum_{\gamma=1}^{D} \mathcal{G}_{i_1 j_2 \cdots j_d \gamma} \mathcal{H}_{i'_1 j'_2 \cdots j'_d \gamma}, \tag{2.73}$$

as an approximated $2d$-rank tensor on a coarse-grained lattice site. This picture may be helpful to understand the procedure of the ATRG.

Finally, let us consider the total computational cost in the current implementation of the ATRG algorithm. The memory footprint is $\mathcal{O}(D^{\max(d+1,4)})$, which is smaller than that of the HOTRG, $\mathcal{O}(D^{2d})$. As the computational complexity, we are required the $\mathcal{O}(qD^{\min(d+3,6)})$ cost in the subscript-swapping procedure. The current implementation requires the $\mathcal{O}(D^6)$ cost in the EVD, Eqs. (2.58) and (2.59), to derive the squeezers. These must be compared with the costs of Eqs. (2.50) and (2.51), which scale with $\mathcal{O}(D^{2d+1})$. Table 2.1 shows the comparison of these complexities at each dimension d. According to Ref. [Oba20], it is practically sufficient to set $q = \mathcal{O}(D)$ in the RSVD algorithm applied in the ATRG. This tells us that when $d \geq 4$, the bottleneck of the algorithm comes from the tensor contractions of Eqs. (2.50) and (2.51), whose execution time can be reduced by the parallel computation. The implementation provided in Ref. [AKYY20] reduces the computational complexity per one process from $\mathcal{O}(D^{2d+1})$ to $\mathcal{O}(D^{2d})$. When $d = 3$, the costs of the tensor contraction and the subscript-swapping procedure are comparable. In $d = 2$, the EVDs of Eqs. (2.58) and (2.59) are the bottleneck. Since our target is to investigate the higher-dimensional QFTs with the algorithm, this is not a problem in any way. If one uses the RSVD, instead of EVDs and full SVD, to fined the squeezers, however, the the cost is reduced to be $\mathcal{O}(D^5)$ from $\mathcal{O}(D^6)$. Therefore, the total computational complexity in the d-dimensional ATRG scales with $\mathcal{O}(D^{2d+1})$ in the current implementation.

Table 2.1: Scaling of the computational costs in the subscript-swapping procedure, to obtain the squeezers, and the tensor contraction in the renormalization-group transformation. If one applied the RSVD in deriving the squeezers, the cost is reduced to be $\mathcal{O}(D^5)$ from $\mathcal{O}(D^6)$.

Dimension d	2	3	4	5
Subscript-swapping	qD^5	qD^6	qD^6	qD^6
Derivation of the squeezers	D^6	D^6	D^6	D^6
Tensor contraction in Eqs. (2.50) and (2.51)	D^5	D^7	D^9	D^{11}

2.3 Formalism of the Grassmann tensor renormalization group

Here, we follow the formulation of Ref. [AK21a], where the fermionic path integrals are expressed by the Grassmann tensors. Let us now consider the following fermionic action as an example,

$$S[\bar{\psi}, \psi] = \sum_{n \in \Lambda} \left[-t \sum_{\nu=1}^{d} \left(\bar{\psi}(n)\psi(n+\hat{\nu}) + \bar{\psi}(n+\hat{\nu})\psi(n) \right) + W[\bar{\psi}(n), \psi(n)] \right]. \tag{2.74}$$

$\psi(n)$ and $\bar{\psi}(n)$ are the fermion fields. For simplicity, we assume that they are single-component Grassmann fields. The path integral is

$$Z = \left(\prod_{n \in \Lambda_d} \int \int \mathrm{d}\bar{\psi}(n)\mathrm{d}\psi(n) \right) \mathrm{e}^{-S[\bar{\psi},\psi]}. \tag{2.75}$$

We decompose hopping factors introducing auxiliary Grassmann fields such that

$$\mathrm{e}^{t\bar{\psi}(n)\psi(n+\hat{\nu})} = \int \int \mathrm{d}\bar{\eta}_\nu(n)\mathrm{d}\eta_\nu(n) \, \mathrm{e}^{-\bar{\eta}_\nu(n)\eta_\nu(n)} \, \mathrm{e}^{\sqrt{t}\bar{\psi}(n)\eta_\nu(n)} \, \mathrm{e}^{-\sqrt{t}\psi(n+\hat{\nu})\bar{\eta}_\nu(n)}, \tag{2.76}$$

$$\mathrm{e}^{t\bar{\psi}(n+\hat{\nu})\psi(n)} = \int \int \mathrm{d}\bar{\xi}_\nu(n)\mathrm{d}\xi_\nu(n) \, \mathrm{e}^{-\bar{\xi}_\nu(n)\xi_\nu(n)} \, \mathrm{e}^{-\sqrt{t}\bar{\psi}(n+\hat{\nu})\bar{\xi}_\nu(n)} \, \mathrm{e}^{-\sqrt{t}\psi(n)\xi_\nu(n)}. \tag{2.77}$$

Thanks to these decompositions, we are now allowed to integrate out $\psi(n)$ and $\bar{\psi}(n)$ independently at each site. The Grassmann tensor $\mathcal{T}$ is defined as a result of the integration,

$$\mathcal{T} = \int \int \mathrm{d}\bar{\psi}\mathrm{d}\psi \, \mathrm{e}^{-W[\bar{\psi},\psi]} \prod_{\nu=1}^{d} \mathrm{e}^{\sqrt{t}\bar{\psi}\eta_\nu(n)} \, \mathrm{e}^{-\sqrt{t}\psi\xi_\nu(n)} \, \mathrm{e}^{-\sqrt{t}\bar{\psi}\bar{\xi}_\nu(n-\hat{\nu})} \, \mathrm{e}^{-\sqrt{t}\psi\bar{\eta}_\nu(n-\hat{\nu})}. \tag{2.78}$$

Since (η_ν, ξ_ν) and $(\bar{\eta}_\nu, \bar{\xi}_\nu)$ play the roles of bond degrees of freedom, we regard them as subscripts of the Grassmann tensor; $\mathcal{T}_{\Psi_1 \cdots \Psi_d \bar{\Psi}_d \cdots \bar{\Psi}_1}$ with $\Psi_\nu = (\eta_\nu, \xi_\nu)$ and $\bar{\Psi}_\nu = (\bar{\eta}_\nu, \bar{\xi}_\nu)$. The path integral of Eq. (2.75) is now expressed by

$$Z = \left(\prod_{n \in \Lambda_d} \prod_{\nu=1}^{d} \int \int \mathrm{d}\bar{\Psi}_\nu(n)\mathrm{d}\Psi_\nu(n) \, \mathrm{e}^{-\bar{\Psi}_\nu(n)\Psi_\nu(n)} \right) \prod_{n \in \Lambda_d} \mathcal{T}_{\Psi_1(n)\cdots\Psi_d(n)\bar{\Psi}_d(n-\hat{d})\cdots\bar{\Psi}_1(n-\hat{1})}. \tag{2.79}$$

We refer this expression as the Grassmann tensor network representation for Z. For notational convenience, we also express Eq. (2.79) by

$$Z = \mathrm{gTr} \left[\prod_{n \in \Lambda_d} \mathcal{T}_{\Psi_1(n)\cdots\Psi_d(n)\bar{\Psi}_d(n-\hat{d})\cdots\bar{\Psi}_1(n-\hat{1})} \right], \tag{2.80}$$

imitating the notation of Eq. (2.12).

To apply a certain TRG algorithm to evaluate Eq. (2.80), one needs to develop the corresponding algorithm extended to evaluate the Grassmann integral. To this aim, we rewrite Eq. (2.78) in the following form,

$$\mathcal{T} = \left(\prod_{\nu=1}^{d} \sum_{i_\nu, j_\nu, i'_\nu, j'_\nu} \right) T_{(i_1 j_1)\cdots(i_d j_d)(i'_1 j'_1)\cdots(i'_d j'_d)} \eta_1^{i_1} \xi_1^{j_1} \cdots \eta_d^{i_d} \xi_d^{j_d} \bar{\xi}_d^{j'_d} \bar{\eta}_d^{i'_d} \cdots \bar{\xi}_1^{j'_1} \bar{\eta}_1^{i'_1}. \tag{2.81}$$

T in the right-hand side is a tensor in the usual sense.[7] In the practical TRG calculation, we have to encode the information of the Grassmann algebra into T in some way. One of such ways is to encode the Grassmann parity for each Ψ_ν, $\bar{\Psi}_\nu$ into the ordering of corresponding ν-directional subscript in T. Table 2.2 shows an example, which maps the ν-directional subscript $(i_\nu j_\nu)$ to the new one $I_\nu \in \mathbb{N}$.

---

[7]One can easily obtain an explicit form of T, but it is not necessary in the following discussion.

Based on the mapping in Table 2.2, we can regard T in Eq. (2.81) as a $2d$-rank tensor $T_{I_1 \cdots I_d I'_1 \cdots I'_d}$. For each subscript I_ν (I'_ν), the first two components correspond to the Grassmann-even sector of Ψ_ν ($\bar{\Psi}_\nu$). When one implements the Grassmann TRG algorithm, it is necessary to read out the Grassmann parity from the subscript of T. This means that we need to define a binary function f_ν on I_ν: $f_\nu(I_\nu) = 0$ (1) if I_ν corresponds to the Grassmann-even (odd) sector. Thanks to these binary functions, we can reproduce the Grassmann algebra just in T. For instance,

$$T_{I_1 I_2 I_3 \cdots I_d I'_1 \cdots I'_d} = (-1)^{f_1(I_1) f_2(I_2)} T_{I_2 I_1 I_3 \cdots I_d I'_1 \cdots I'_d} \tag{2.82}$$

corresponds to the exchange between Ψ_1 and Ψ_2. The same argument also holds for the renormalized Grassmann tensor $\mathcal{T}'$ defined by a certain TRG algorithm, where the SVD,

$$Q_{abcd} \approx \sum_{k=1}^{D} U_{ab,k} \sigma_k V^*_{cd,k}, \tag{2.83}$$

is employed to introduce the coarse-grained degrees of freedom. Within the formulation explained above, each subscript has the information of the Grassmann parity, which allows us to consider the block-diagonal representation of Eq. (2.83),

$$\begin{bmatrix} Q^{(\text{even})} & 0 \\ 0 & Q^{(\text{odd})} \end{bmatrix} \approx \begin{bmatrix} U^{(\text{even})} & 0 \\ 0 & U^{(\text{odd})} \end{bmatrix} \begin{bmatrix} \sigma^{(\text{even})} & 0 \\ 0 & \sigma^{(\text{odd})} \end{bmatrix} \begin{bmatrix} V^{(\text{even})\dagger} & 0 \\ 0 & V^{(\text{odd})\dagger} \end{bmatrix} \tag{2.84}$$

In Eq. (2.83), the subscript k corresponds to a new auxiliary Grassmann field in ν-direction. In addition, if σ_k belongs to $\sigma^{(\text{even})}$ ($\sigma^{(\text{odd})}$), then k represents the Grassmann-even (odd) component. In other words, the block-diagonalized SVD defines a new binary function f_ν for the coarse-grained auxiliary Grassmann field in ν-direction.

Table 2.2: Mapping of subscripts.

$I_\nu^{(')}$	1	2	3	4
$i_\nu^{(')}$	0	1	1	0
$j_\nu^{(')}$	0	1	0	1

Now, it must be ready to extend a certain TRG algorithm to evaluate Eq. (2.79). All we have to do is to carry out the TRG algorithm combining some phase factor $(-1)^p$ characterized by binary functions which reproduce the Grassmann algebra. Suppose we make a renormalization-group mapping based on the HOTRG along $\hat{1}$-direction, which firstly carries out the Grassmann integration,

$$\begin{aligned} &(\mathcal{T}\mathcal{T})_{\Psi_1(n+\hat{1})\Xi_2 \cdots \Xi_d \bar{\Xi}_d \cdots \bar{\Xi}_2 \bar{\Psi}_1(n-\hat{1})} \\ &= \int \int \mathrm{d}\bar{\Psi}_1(n)\mathrm{d}\Psi_1(n) \, \mathrm{e}^{-\bar{\Psi}_1(n)\Psi_1(n)} \mathcal{T}_{\Psi_1(n+\hat{1}) \cdots \Psi_d(n+\hat{1})\bar{\Psi}_d(n+\hat{1}-\hat{d}) \cdots \bar{\Psi}_1(n)} \mathcal{T}_{\Psi_1(n) \cdots \Psi_d(n)\bar{\Psi}_d(n-\hat{d}) \cdots \bar{\Psi}_1(n-\hat{1})}, \end{aligned} \tag{2.85}$$

before we apply isometries to accomplish the renormalization-group transformation $(\mathcal{T}\mathcal{T}) \mapsto \mathcal{T}'$. We have used shorthand notations defined by $\Xi_\nu = (\Psi_\nu(n+\hat{1})\Psi_\nu(n))$ and $\bar{\Xi}_\nu = (\bar{\Psi}_\nu(n-\hat{\nu})\bar{\Psi}_\nu(n+\hat{1}-\hat{\nu}))$.

Therefore, introducing $\tilde{I}_\nu(n) = f_\nu(I_\nu(n))$, one can find

$$
\begin{aligned}
p = {} & \tilde{I}_1(n) \\
& + \tilde{I}_2(n)\tilde{I}_2(n+\hat{1}) \\
& + \tilde{I}_3(n)[\tilde{I}_2(n+\hat{1}) + \tilde{I}_3(n+\hat{1})] \\
& + \cdots \\
& + \tilde{I}_d(n)[\tilde{I}_2(n+\hat{1}) + \cdots + \tilde{I}_d(n+\hat{1})] \\
& + \tilde{I}'_d(n-\hat{d})[\tilde{I}'_d(n+\hat{1}-\hat{d}) + \cdots + \tilde{I}'_2(n+\hat{1}-\hat{2})] \\
& + \tilde{I}'_{d-1}(n-\widehat{d-1})[\tilde{I}'_{d-1}(n+\hat{1}-\widehat{d-1}) + \cdots + \tilde{I}'_2(n+\hat{1}-\hat{2})] \\
& + \cdots \\
& + \tilde{I}'_2(n-\hat{2})\tilde{I}'_2(n+\hat{1}-\hat{2})
\end{aligned}
\tag{2.86}
$$

is the phase factor which makes the contraction

$$
(TT)_{I_1(n+\hat{1})L_2\cdots L_d I'_1(n)L'_2\cdots L'_d} = \sum_{I_1(n)}(-1)^p T_{I_1(n+\hat{1})\cdots I_d(n+\hat{1})I_1(n)\cdots I'_d(n-\hat{d}+\hat{1})} T_{I_1(n)\cdots I_d(n)I'_1(n-\hat{1})\cdots I'_d(n-\hat{d})}
\tag{2.87}
$$

equivalent to Eq. (2.85). [8] Note that we have introduced shorthand notations $L_\nu = (I_\nu(n+\hat{1})I_\nu(n))$ and $L'_\nu = (I'_\nu(n+\hat{1}-\hat{\nu})I'_\nu(n-\hat{\nu}))$. It is a very straightforward task to develop the Grassmann version of the HOTRG or ATRG reflecting on Eqs. (2.86) or (2.87). [9] In the case of the Grassmann HOTRG, instead of considering the subnetwork in Eq. (2.27), we start from the right-hand side of Eq. (2.87) to construct the renormalization-group transformation of Eq. (2.28). In the case of the Grassmann ATRG, the phase in Eq. (2.86) is took into account separately. Instead of Eq. (2.43), we firstly consider

$$
\sum_{I_1(n)}(-1)^{\tilde{I}_1(n)}\mathcal{B}_{I_1(n)I'_2(n+\hat{1})\cdots I'_d(n+\hat{1})\alpha}\mathcal{C}_{I_1(n)I_2(n)\cdots I_d(n)\beta}
$$

$$
\approx \sum_{\gamma=1}^{D} U[\mathcal{BC}]_{I_2(n)\cdots I_d(n)\alpha,\gamma}\sigma[\mathcal{BC}]_\gamma V^*[\mathcal{BC}]_{I'_2(n+\hat{1})\cdots I'_d(n+\hat{1})\beta,\gamma}.
\tag{2.88}
$$

As the second modification, the renormalization-group transformations defined in Eqs. (2.50) and (2.51) are replaced by

$$
\sum_{\substack{\text{subscripts} \\ \text{except } I_1(n+\hat{1}),\gamma}}(-1)^P \mathcal{A}_{I_1(n+\hat{1})I_2(n+\hat{1})\cdots I_d(n+\hat{1})\alpha}U[\mathcal{BC}]_{I_2(n)\cdots I_d(n)\alpha,\gamma}\sigma[\mathcal{BC}]_\gamma \prod_{\nu\neq1}E^{(\nu)}_{I_\nu(n+\hat{1})I_\nu(n),J_\nu},
\tag{2.89}
$$

and

$$
\sum_{\substack{\text{subscripts} \\ \text{except } I'_1(n),\gamma}}(-1)^{P'}V^*[\mathcal{BC}]_{I'_2(n+\hat{1})\cdots I'_d(n+\hat{1})\beta,\gamma}\mathcal{D}_{I'_1(n)I'_2(n)\cdots I'_d(n)\beta}\prod_{\nu\neq1}F^{(\nu)}_{I'_\nu(n+\hat{1})I'_\nu(n),J_\nu},
\tag{2.90}
$$

---

[8] To derive Eq. (2.86), we have employed a trick, $\tilde{I}_\nu(n) = \tilde{I}'_\nu(n-\hat{\nu})$.

[9] When one assumes the anti-periodic boundary condition in $\hat{\nu}$-direction, an additional phase factor $(-1)^{\tilde{I}_\nu}$ is necessary just in taking the trace of T.

with

$$
\begin{aligned}
P = {}& \tilde{I}_2(n)\tilde{I}_2(n+\hat{1}) \\
& + \tilde{I}_3(n)[\tilde{I}_2(n+\hat{1}) + \tilde{I}_3(n+\hat{1})] \\
& + \cdots \\
& + \tilde{I}_d(n)[\tilde{I}_2(n+\hat{1}) + \cdots + \tilde{I}_d(n+\hat{1})],
\end{aligned} \tag{2.91}
$$

and

$$
\begin{aligned}
P' = {}& \tilde{I}'_d(n-\hat{d})[\tilde{I}'_d(n+\hat{1}-\hat{d}) + \cdots + \tilde{I}'_2(n+\hat{1}-\hat{2})] \\
& + \tilde{I}'_{d-1}(n-\widehat{d-1})[\tilde{I}'_{d-1}(n+\hat{1}-\widehat{d-1}) + \cdots + \tilde{I}'_2(n+\hat{1}-\hat{2})] \\
& + \cdots \\
& + \tilde{I}'_2(n-\hat{2})\tilde{I}'_2(n+\hat{1}-\hat{2}).
\end{aligned} \tag{2.92}
$$

Notice that the phases P and P' must be included in the derivation of the squeezers $E^{(\nu)}$'s and $F^{(\nu)}$'s.

2.4 Impurity tensor method

So far, we have seen how to derive tensor network representations for path integrals and how to evaluate them within some TRG algorithms. We can indeed obtain various types of thermodynamic functions once we have had a path integral. This is because the path integral is a generating function whose derivative gives us an expectation value of a certain observable. It is instructive, however, there is another way to evaluate these expectation values without employing numerical differentiation. This technique is the so-called "impurity tensor method", which is demonstrated in Refs. [YKN$^+$18, MOR19], for instance.

The idea of this technique is quite simple. As we derived a tensor network representation for a path integral, we express an expectation value $\langle O \rangle$ for some observable O by a tensor network. As an example, let us consider a magnetization on site p, $\langle \sigma(p) \rangle$, of the Ising model. This quantity is defined as

$$
\langle \sigma(p) \rangle = \frac{1}{Z} \left[\left(\prod_{n \in \Lambda_d} \sum_{\sigma(n)} \right) \sigma(p) \prod_{n \in \Lambda_d} \exp \left[\sum_{\nu=1}^{d} W[\sigma(n), \sigma(n+\hat{\nu})] + M[\sigma(n)] \right] \right]. \tag{2.93}
$$

For the denominator, we have already derived the tensor network representation, which results in the form of Eq. (2.12). For the numerator, we have the same $2d$-rank tensor in Eq. (2.6) except $n = p$. At $n = p$, we need to consider the integration,

$$
\mathcal{S}_{i_1(p)\cdots i_d(p)i_1(p-\hat{1})\cdots i_d(p-\hat{d})} = \sum_{\sigma} \sigma \mathrm{e}^{M[\sigma]} \prod_{\nu=1}^{d} U_{\sigma i_\nu(p)} V^*_{\sigma i_\nu(p-\hat{\nu})} \sqrt{s_{i_\nu(p)}} \sqrt{s_{i_\nu(p-\hat{\nu})}}, \tag{2.94}
$$

where we have set the result as a $2d$-rank tensor $\mathcal{S}$. $\mathcal{S}$ is referred as an impurity tensor, named after the expression,

$$
\langle \sigma(p) \rangle = \frac{\mathrm{tTr} \left[\mathcal{S}_{i_1(p)\cdots i_d(p)i_1(p-\hat{1})\cdots i_d(p-\hat{d})} \prod_{n \neq p} \mathcal{T}_{i_1(n)\cdots i_d(n)i_1(n-\hat{1})\cdots i_d(n-\hat{d})} \right]}{\mathrm{tTr} \left[\prod_n \mathcal{T}_{i_1(n)\cdots i_d(n)i_1(n-\hat{1})\cdots i_d(n-\hat{d})} \right]}, \tag{2.95}
$$

which seems that there is one-point impurity in the uniform tensor network. As in the same way, we can derive tensor network representations for n-point functions.

Eq. (2.95) is ready to be evaluated by the HOTRG or the ATRG. There is no problem making a renormalization-group transformation for the denominator. For the numerator, we insert the same isometries or squeezers applied in coarse-graining the tensor network of the denominator. Strictly speaking, these isometries or squeezers are not optimal as for the tensor network of the numerator. However, it is empirically known that these projectors do work also in evaluating a tensor network including a few impurity tensors, located nearby.

3   Ising model

The Ising model is the simplest model expressed by Eq. (2.1). The lower critical dimension is one and the upper critical dimension is four. The model in two dimensions is exactly solved and the system does show the critical behavior. Therefore, the two-dimensional Ising model should be the first testbed for the TRG approach. We review some TRG studies of the model in three dimensions, where the precise critical temperature and exponents are available comparing the MC simulation. The study of the Ising model with the TRG approach is then extended also in four dimensions.

3.1   Two- and three-dimensional models

The tensor network representation of the partition function of the d-dimensional Ising model is easily obtained via the derivation explained in the precious section. Here, we see the accuracy of the TRG method, benchmarking with the two-dimensional Ising model, whose exact solution is given by

$$\frac{1}{V} \ln Z = \ln \left(2 \cosh(2K) \right) + \int_0^{\pi} \frac{\mathrm{d}\theta}{2\pi} \ln \left[\frac{1}{2} \left(1 + \sqrt{1 - s^2 \cos^2 \theta} \right) \right],$$

(3.1)

where $K = \beta J$ and

$$s = \frac{2 \sinh 2K}{\cosh^2 2K}.$$

(3.2)

The critical point T_{c} is exactly determined by

$$J/T_{\mathrm{c}} = \frac{1}{2} \ln \left(1 + \sqrt{2} \right).$$

(3.3)

Note that $s = 1$ holds at the critical point. Fig. 3.1 compares the relative errors of $\ln Z$ obtained by several TRG algorithms with respect to the exact solution. All calculations are carried out with $D = 24$. The result shows that both the HOTRG and the ATRG improve the accuracy of the original Levin-Nave TRG [LN07], at the same D. On the other hand, Fig. 3.2 shows the resulting relative errors as functions of execution time obtained by our implementation of the ATRG explained in the previous section and the HOTRG. At the same execution time, the ATRG achieves better performance compared with the HOTRG. This result indicates a potential efficiency of the ATRG algorithm over the HOTRG, particularly in the higher dimensions. Fig. 3.3 shows the internal energy as a function of temperature obtained by the HOTRG calculation with the impurity method. Enlarging the bond dimension, the exact solution is well restored. The internal energy E is exactly obtained via

$$E = -\frac{1}{V} \frac{\partial}{\partial \beta} \ln Z,$$

(3.4)

which is expressed by

$$E = -J \coth 2K \left[1 - (1 - 2 \tanh^2 2K) \frac{2}{\pi} \mathcal{K}(s) \right],$$

(3.5)

with the complete elliptic integral of the first kind,

$$\mathcal{K}(k) = \int_0^{\pi/2} \frac{\mathrm{d}\theta}{\sqrt{1 - k^2 \sin^2 \theta}}.$$

(3.6)
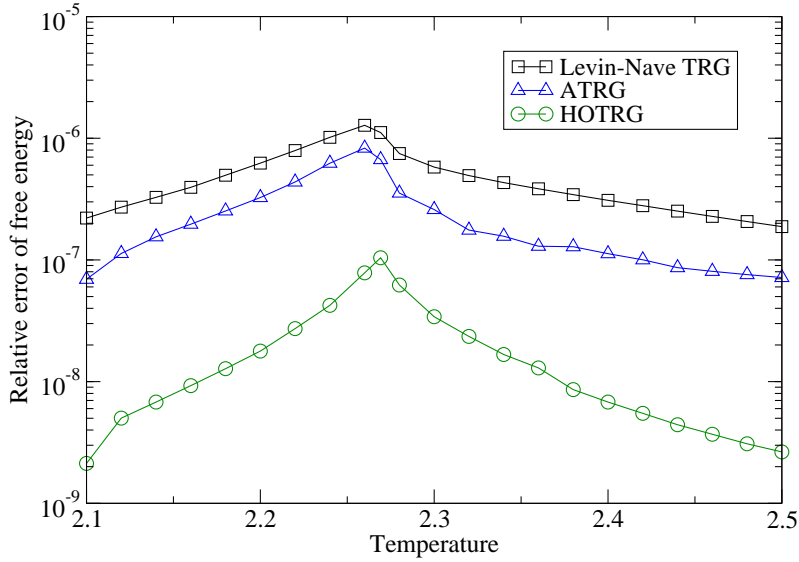
Figure 3.1: Comparison of the relative errors of $\ln Z$ obtained by the Levin-Nave TRG, our implementation of the ATRG, and the HOTRG. In all TRG computations, we set $D = 24$.
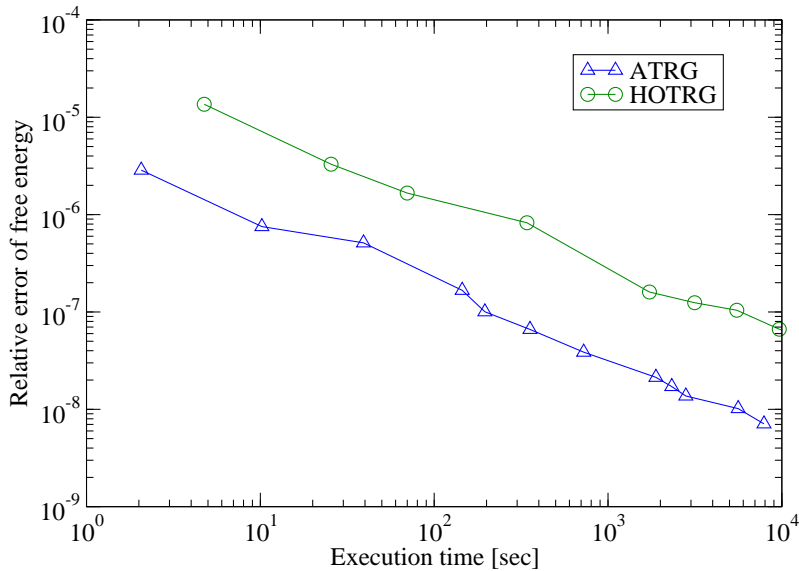
Figure 3.2: Comparison of the relative errors of $\ln Z$ obtained by our implementation of the ATRG and the HOTRG as functions of execution time. The former shows a better performance at the same execution time compared with the HOTRG.
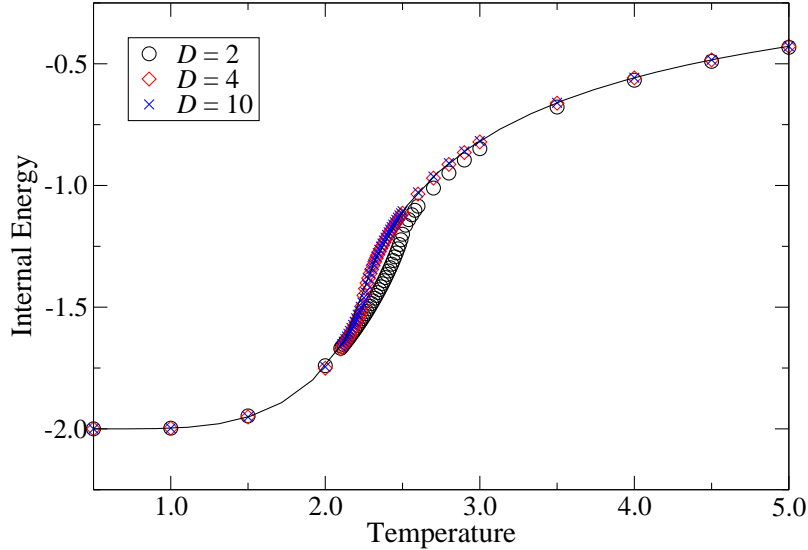
Figure 3.3:   Comparison of the HOTRG computation and the exact internal energy of Eq. (3.5). Enlarging the bond dimension D, the HOTRG restores the exact result.

Both figs. 3.1 and 3.3 show the high precision of the TRG algorithms in the two-dimensional Ising model. [1]

Moreover, the three-dimensional Ising model was precisely investigated by the HOTRG algorithm in Refs. [XCQ$^+$12, WXC$^+$14]. Table 3.1 compares the critical temperatures obtained by various methods. The HOTRG calculations agree with the MC result. In addition, Ref. [XCQ$^+$12] estimates the critical exponent of the specific heat α by fitting the internal energy. They find $\alpha = 0.1023$ with $T > T_c$ and $\alpha = 0.1137$ with $T < T_c$. These values are consistent with the MC simulation in Ref. [Has01], which results in $\alpha = 0.111$. The critical exponent of the magnetization β is also provided in Ref. [XCQ$^+$12]. They find the exponent $\beta = 0.3295$ by fitting the magnetization in the thermodynamic limit. $\beta = 0.3262$ is found by the MC simulation in Ref. [Has01]. These numerical investigations highly suggest that the TRG approach is not only limited to two dimensions, but also applicable to the higher dimensions.

3.2 Four-dimensional model

Since the upper critical dimension of the Ising model is four, the model defined in the dimensions larger than four is believed to be well explained by the mean-field theory. Refs. [Aiz81, Aiz82] show that the effect of the background fluctuations becomes negligible and the model with dimensions larger than four does obey the mean-field exponents. Just on the upper critical dimension, some multiplicative logarithmic corrections are combined to the leading scaling behaviors of the mean-field theory. Some of these corrections were derived by the perturbative calculation with the renormalization group method

---

[1]Note that much more accurate TRG algorithms can be available in case of the two-dimensional systems. Tensor network renormalization (TNR) [EV15, Eve17] is such a typical algorithm. There also exist some variants of the TNR [YGW17, IMK20].

Table 3.1: Comparison of the critical point in the three-dimensional Ising model.

Method	T_c
HOTRG with $D = 23$ (2014) [WXC$^+$14]	4.51152469(1)
HOTRG with $D = 16$ (2012) [XCQ$^+$12]	4.511544
Monte Carlo (2010) [Has10]	4.5115232(17)
TPVA (2005) [GN05]	4.554
CTMRG (2001) [NHO$^+$01]	4.5393
Series Expansion (2000) [BC00]	4.511536(21)

[WR73]. Since the Ising model can be identified as an infinite-coupling limit of the single-component scalar ϕ^4 theory, the four-dimensional Ising model has also been attracting the interest of particle physicists for a long time, in the context of the triviality of the lattice ϕ^4 theory in four dimensions, which is related to the scalar sector of the standard model describing the generation of gauge boson and fermion mass via the Higgs mechanism [WK74, LW87, LW88, LW89, Hua89, JTM$^+$89, FJJ$^+$90]. [2]

A numerical study of the four-dimensional Ising model serves as a non-perturbative test of the triviality as demonstrated in Refs. [KL93, Ken04]. If the leading scaling behavior is explained by the mean-field theory and it is modified just by the multiplicative logarithmic factor, it supports a scenario of the triviality of the lattice ϕ^4 theory in four dimensions. Although some previous MC studies successfully caught the mean-field exponents [BS80, SV87, BJM02, LM09, LM11], there remains some controversy over the appearance of the logarithmic corrections [LM09, LM11, CCC05, Ste05, BNW06]. This is mainly coming from the current status of this model where no MC study has confirmed the logarithmic correction expected by the perturbative renormalization group analysis in the scaling behavior of the specific heat, which is $(\ln |t|)^{1/3}$ with the reduced temperature $t = (T - T_c)/T_c$. This can be attributed to the difficulty that the cubic root of logarithmic divergence is too weak to be detected by the finite-size scaling analysis, or the possibility that the specific heat may be actually bounded [LM09]. The finite-size effect of the four-dimensional Ising model was investigated from various viewpoints [JTM$^+$89] and a recent detailed MC research found a serious finite-size effect due to some non-trivial boundary effect in the four-dimensional Ising model [LM11]. From the viewpoint of numerical study, it could be possible that there remain some unrevealing aspects in the phase transition of this model. In addition, it should be worth trying different approaches other than the MC method.

In the following, we apply the parallelized HOTRG algorithm to investigate the four-dimensional Ising model. As an advantage of the TRG approach, we can study the model in the thermodynamic limit, where the finite-size effect is negligible. Note that this part is mainly based on Ref. [AKYY19], which is the first application of the TRG approach to the four-dimensional system, and partially on Ref. [AKYY20].

Using the parallelized HOTRG, we enlarge the bond dimension up to $D = 13$. We first evaluate the free energy whose convergence behavior is confirmed via the quantity,

$$\delta_D = \left| \frac{\ln Z(D) - \ln Z(D = 13)}{\ln Z(D = 13)} \right|. \tag{3.7}$$

Figure 3.4 shows a typical behavior of δ_D in the vicinity of the transition point, as we see below. We observe that δ_D decreases monotonically as a function of D. Next we survey the location of the

---

[2]There are also recent studies to discuss the triviality of the four-dimensional $O(N)$ ϕ^4 theory with the higher-loop beta function [Shr14, Shr16, Shr17].
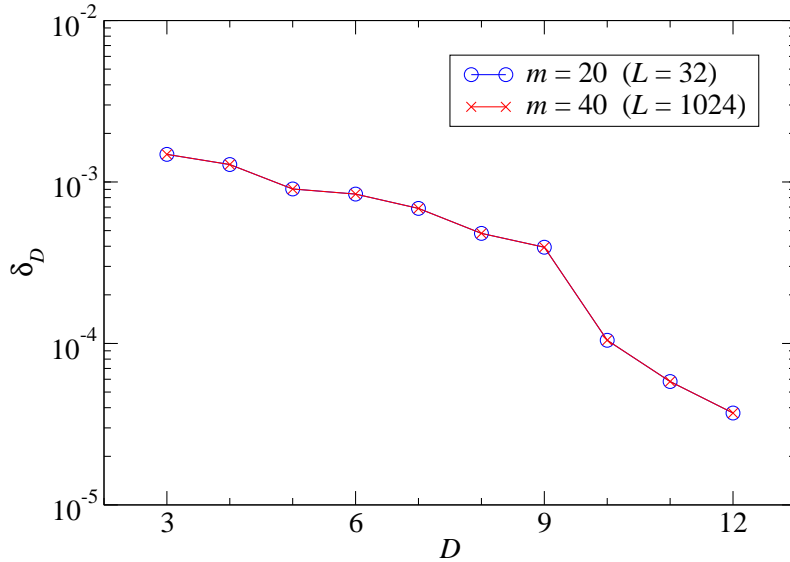
Figure 3.4: Convergence behavior of $\ln Z$ as a function of bond dimension D at $T = 6.64250$ in the vicinity of the transition point. m denotes the iteration number, which gives a linear lattice size L via $L = 2^{m/4}$.

transition point observing the quantity,

$$X^{(m)} = \frac{\left(\text{Tr} A^{(m)}\right)^2}{\text{Tr} \left(A^{(m)}\right)^2},\tag{3.8}$$

where $A^{(m)}$ is a $D \times D$ matrix defined by

$$A^{(m)}_{i_4 i'_4} = \sum_{i_1,i_2,i_3} \mathcal{T}^{(m)}_{i_1 i_2 i_3 i_4 i_1 i_2 i_3 i'_4}.\tag{3.9}$$

$\mathcal{T}^{(m)}$ denotes the m-th coarse-grained tensor obtained in the HOTRG calculation. The quantity $X^{(m)}$ counts the number of the largest singular value of $A^{(m)}$ and is useful to detect the $\mathbb{Z}_n$-symmetry breaking [GW09]. Fig. 3.5 shows a history of $X^{(m)}$ with respect to the iteration number m. After sufficient times of iteration, typically beyond $m = 30$, $X^{(m)} = 1$ holds when the system is in the disordered (symmetric) phase and $X^{(m)} = 2$ when in the ordered (symmetry-breaking) phase. It should be emphasized that in the current HOTRG calculation, we can identify which phase is realized on the lattice whose volume is $V = 1024^4$ with the temperature resolution $\Delta T = 6.25 \times 10^{-6}$. Figure 3.6 shows the transition temperature T_c as a function of D. The error bars, provided by the temperature resolution, are all smaller than the corresponding symbols. Since $T_c(D)$ is estimated by $X^{(m)}$ with sufficiently large m, there remains little finite-size effect. The current HOTRG calculation locates the transition point at $T_c(D = 13) = 6.650365(5)$ on 1024^4 lattice. Note that a recent MC study [LM09] found $\beta_c = 0.1496947(5)$, which corresponds to $T_c = 6.68026(2)$, so there is a slight deviation from the result with HOTRG up to $D = 13$. This deviation might be attributed to the infinite-volume extrapolation in Ref. [LM09], which uses the results on relatively small lattices with $V \leq 80^4$. For

comparison, we also plot $T_c(D)$ obtained by the parallelized ATRG calculation in Fig. 3.6, which is based on Ref. [AKYY20]. Although the range of the bond dimension is quite different between the HOTRG and the ATRG, the resulting location of the transition point seems comparable between these two kinds of algorithms.
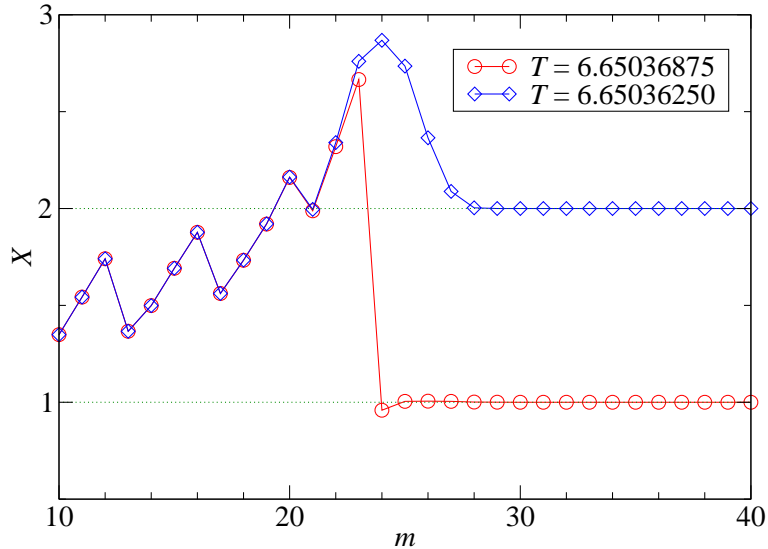
Figure 3.5: $X^{(m)}$ at the m-th coarse-graining step with $D = 13$. Red line corresponds to the disordered phase and blue one does to the ordered one.

Let us now move on to the evaluation of the internal energy, which can be obtained by numerical differentiation or the coarse-graining of the tensor network including two impurities. We compared both methods varying the temperature resolution and found that the latter successfully keeps the numerical stability as the resolution becomes finer. In the following, we show the results with the impurity tensor method. Figure 3.7 shows typical histories of the internal energy with respect to the iteration number m. The convergence toward the thermodynamic limit is clearly observed. Figure 3.8 shows the internal energy as a function of temperature for various lattice sizes in the vicinity of the transition point. With $m \geq 24$, which is equivalent to $L \geq 64$, a finite jump emerges with mutual crossings of curves between different volumes around the transition point. These are characteristic features of the first-order phase transition as discussed in Ref. [FMOU90]. We checked that a similar volume dependence and a finite jump at $L \geq 64$ were observed also in the case of $D = 14$. The numerical value of the finite jump $\Delta E(D = 13)$ in the infinite-volume limit is

$$\Delta E(D = 13) = 0.0034(5),$$

which is obtained by the linear extrapolation toward the transition point both from the low- and high-temperature regimes. The resolution of the temperature at the boundary between the two phases is $\Delta T = 6.25 \times 10^{-6}$. Note that the numerical result of the internal energy obtained by the impurity tensor method is consistent with the location of T_c estimated by the plain HOTRG calculation of $X^{(m)}$.
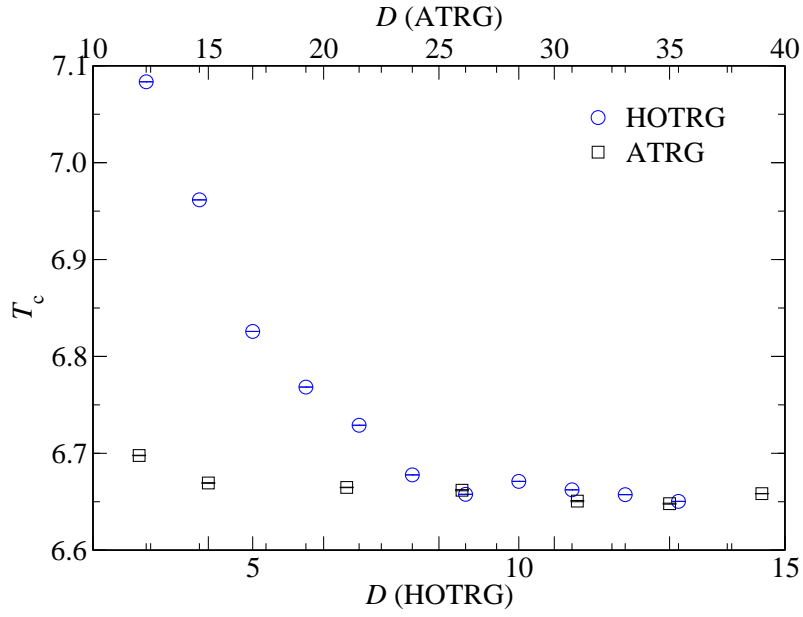
Figure 3.6:   Transition temperature as a function of the bond dimension. The circle shows the result obtained by the HOTRG and the square by the ATRG. Error bars are all within symbols.
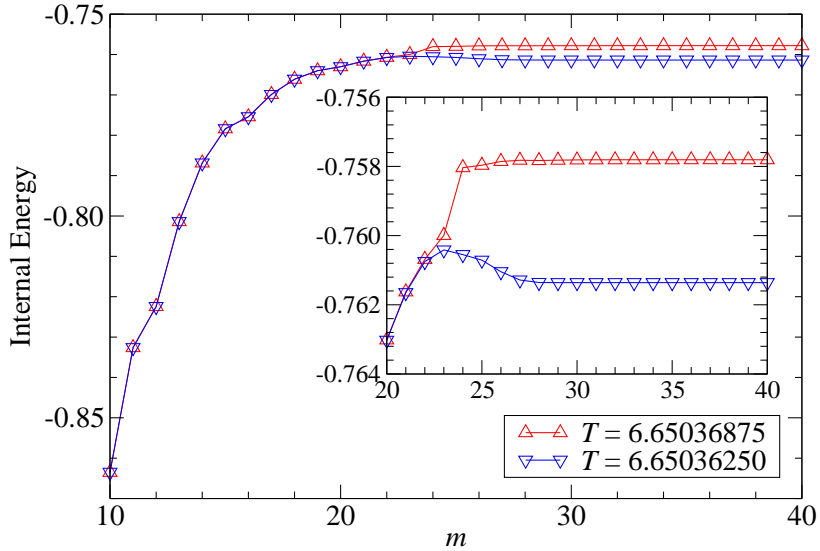
Figure 3.7:   History of the internal energy at the m-th coarse-graining step with $D = 13$. The red line corresponds to the disordered phase and the blue one does to the ordered phase. Inset graph magnifies the m dependence beyond $m = 20$.
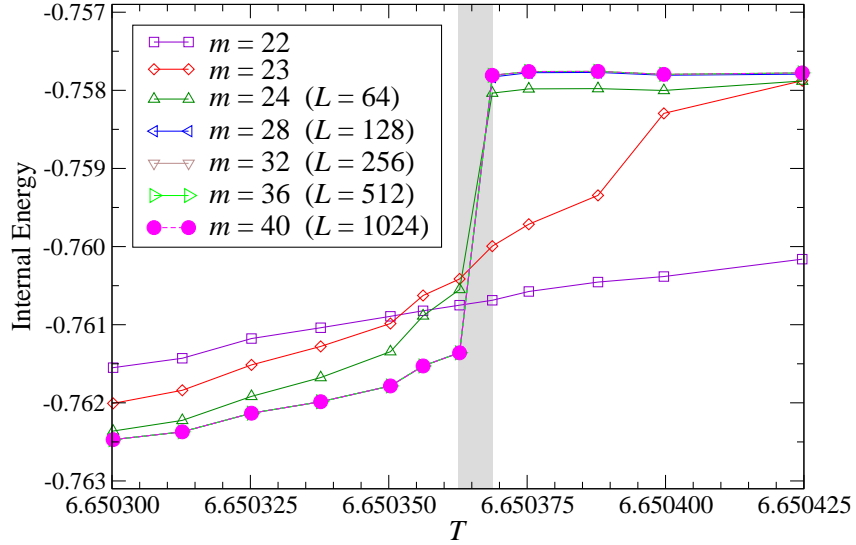
Figure 3.8:   Internal energy as a function of temperature for various lattice size with $D = 13$. $T_{\mathrm{c}}(D = 13)$ estimated by $X^{(m)}$ of Eq. (3.8) is within the gray band.
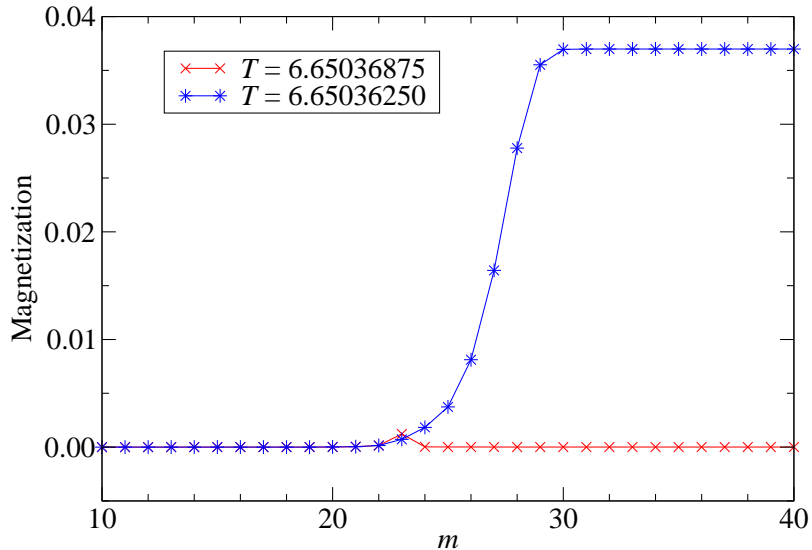
Figure 3.9:   History of the magnetization at the m-th coarse-graining step with $D = 13$ and $h = 1.0 \times 10^{-9}$. The red line corresponds to the disordered phase and the blue one does to the ordered phase.
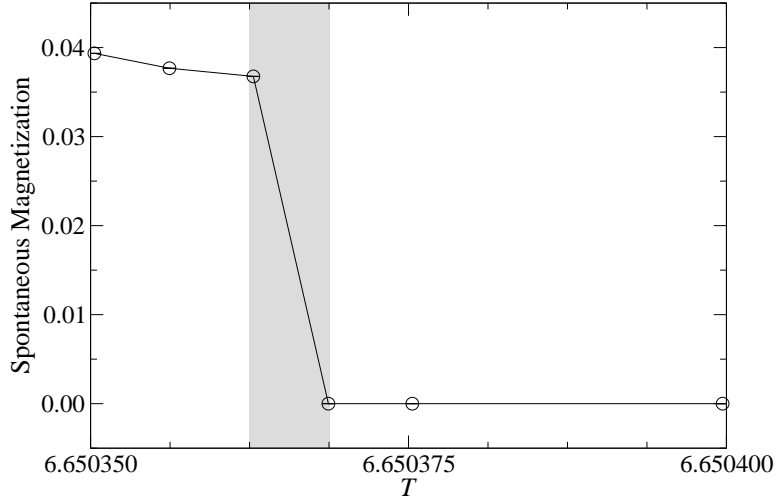
Figure 3.10:   Spontaneous magnetization in the thermodynamic limit with $D = 13$. Error bars, provided by extrapolation, are within symbols. $T_c(D = 13)$ estimated by $X^{(m)}$ of Eq. (3.8) is within the gray band.

Finally, we investigate spontaneous magnetization, which is an order parameter to detect the symmetry-breaking phase transition. We again apply the impurity tensor method, where $\langle \sigma(n) \rangle$ is expressed by a tensor network including one-point impurity. Figure 3.9 shows histories of magnetization toward the thermodynamic limit as a function of m. We evaluate magnetizations with the external fields of $h = 1.0 \times 10^{-9}$ and 2.0×10^{-9}. After taking the infinite-volume limit, we extrapolate data toward the limit $h \to 0$. Figure 3.10 shows the resulting spontaneous magnetization as a function of temperature. The transition point is consistent with both estimates by $X^{(m)}$ and the internal energy. We observe a finite jump in the magnetization, whose numerical value is obtained by the linear extrapolation toward the transition point both from the low- and high- temperature regimes,

$$\Delta m(D = 13) = 0.037(2).$$

The resolution of the temperature at the boundary between the two phases is again $\Delta T = 6.25 \times 10^{-6}$. Note that we tried several choices of the external field other than $h = \mathcal{O}(10^{-9})$ and confirmed that the behavior of the magnetization is numerically robust against the change of the magnitude of h.

4 ϕ^4 theory

As we explained in the previous section, the triviality problem of the four-dimensional lattice ϕ^4 theory is one of the biggest theoretical concerns in particle physics, because ϕ^4 theory is related to the scalar sector in the standard model [WK74, Aiz81, Aiz82, Fro82, DN83, Lin86, HJL$^+$87, LW87, LW88, LW89, Hua89, FJJ$^+$90, KPST07]. The single-component ϕ^4 theory becomes equivalent to the Ising model in the infinite limit of the quartic coupling $\lambda = \infty$, so that numerical studies of the four-dimensional Ising model have been performed as a non-perturbative test of the triviality, assuming the universality [BS80, SV87, KL93, BJM02, Ken04, LM09, LM11]. [1] In the previous section, we investigated the phase transition of the Ising model on the four-dimensional lattice whose volume is varied up to 1024^4 with the HOTRG algorithm. The HOTRG with $D = 13$ finds finite jumps both for the internal energy and the magnetization as functions of temperature. These are characteristic features of the first-order phase transition, which is not expected by the mean-field theory. In this section, we would like to focus on the single-component ϕ^4 theory and its phase transition. We use the ATRG algorithm with the impurity tensor method to investigate the models in three and four dimensions. It must be instructive to study the order of the phase transition in these models. This section is based on Ref. [AKY21b].

4.1 Formulation on a d-dimensional lattice

The single-component ϕ^4 theory on a d-dimensional lattice is defined via the action,

$$S[\phi] = \sum_{n \in \Lambda_d} \left[-2\kappa \sum_{\nu=1}^d \phi(n)\phi(n+\hat{\nu}) + \phi(n)^2 + \lambda \left(\phi(n)^2 - 1 \right)^2 \right]. \tag{4.1}$$

Taking the limit $\lambda \to \infty$, the value of $\phi(n)^2$ is fixed to be 1, so the scalar field $\phi(n)$ is identified with the Ising spin variable. 2κ corresponds to the inverse temperature β in the Ising model. Note that by setting

$$\varphi(n) = \sqrt{2\kappa}\phi(n), \tag{4.2}$$

$$m_0^2 = \frac{1-2\lambda}{\kappa} - 2d, \tag{4.3}$$

$$g_0 = \frac{6\lambda}{\kappa^2}, \tag{4.4}$$

Eq. (4.1) is rewritten as

$$S[\varphi] = \sum_{n \in \Lambda_d} \left[\frac{1}{2} \sum_{\nu=1}^d (\varphi(n+\hat{\nu}) - \varphi(n))^2 + \frac{1}{2}m_0^2\varphi(n)^2 + \frac{g_0}{4!}\varphi(n)^4 \right], \tag{4.5}$$

which may be a more conventional expression for the ϕ^4 theory. The path integral is defined by

$$Z = \left(\prod_{n \in \Lambda_d} \int_{-\infty}^{\infty} \mathrm{d}\phi(n) \right) \mathrm{e}^{-S[\phi]}, \tag{4.6}$$

with the action of Eq. (4.1).

---

[1]In the standard model, we need to consider the ϕ^4 interaction as a part of a combined Higgs-Yukawa sector, whose nonperturbative aspects were investigated with the lattice simulations [LSS90a, LSS90b].

4.2 Tensor network representation

Since the path integral of Eq. (4.6) is given by integrations over non-compact fields $\phi(n)$, we need to employ a certain regularization scheme to obtain its finite-dimensional tensor network representation. Here, we consider the regularization of $\phi(n)$ via the K-point Gauss-Hermite quadrature rule, which gives us

$$\int_{-\infty}^{\infty} \mathrm{d}\phi(n)\ \mathrm{e}^{-\phi(n)^2} F[\phi(n)] \simeq \sum_{i=1}^{K} w_i F[\phi_i(n)], \qquad (4.7)$$

where ϕ_i and w_i are the i-th node and its weight. See Appendix B for the details of the Gauss-Hermite quadrature rule. Using the vector notation introduced in Eq. (2.16), the regularized path integral $Z(K)$ is given by

$$Z(K) = \left(\prod_{n \in \Lambda_d} \sum_{\tilde{\phi}(n)} w_{\tilde{\phi}(n)} \right) \prod_{n \in \Lambda_d} \exp\left[2\kappa \sum_{\nu=1}^{d} \tilde{\phi}(n)\tilde{\phi}(n+\hat{\nu}) - \lambda \left(\tilde{\phi}(n)^2 - 1 \right)^2 \right]. \qquad (4.8)$$

Defining a d-dimensional hopping matrix T via

$$T_{\tilde{\phi}(n)\tilde{\phi}(n+\hat{\nu})} = \sqrt[2d]{w_{\tilde{\phi}(n)}w_{\tilde{\phi}(n+\hat{\nu})}} \exp\left[2\kappa\tilde{\phi}(n)\tilde{\phi}(n+\hat{\nu}) - \frac{\lambda}{2d}\left(\tilde{\phi}(n)^2 - 1 \right)^2 - \frac{\lambda}{2d}\left(\tilde{\phi}(n+\hat{\nu})^2 - 1 \right)^2 \right], \tag{4.9}$$

we carry out the truncated SVD of T as

$$T_{\tilde{\phi}(n)\tilde{\phi}(n+\hat{\nu})} \approx \sum_{i_\nu(n)=1}^{D} U_{\tilde{\phi}(n)i_\nu(n)} s_{i_\nu(n)} V^*_{\tilde{\phi}(n+\hat{\nu})i_\nu(n)}. \qquad (4.10)$$

One obtains a tensor network representation for $Z(K)$ as in the form of Eq. (2.12) with

$$\mathcal{T}_{i_1(n)\cdots i_d(n)i'_1(n)\cdots i'_d(n)} = \sum_{\tilde{\phi}} \prod_{\nu=1}^{d} U_{\tilde{\phi}i_\nu(n)} V^*_{\tilde{\phi}i'_\nu(n)} \sqrt{s_{i_\nu(n)}} \sqrt{s_{i'_\nu(n)}}. \qquad (4.11)$$

4.3 Three-dimensional theory

The theory with $d = 2$ is believed to belong to the two-dimensional Ising universality class. The TRG approach has already been applied to two-dimensional lattice ϕ^4 theory [Shi12b, Shi12a, KKN$^+$19, DT20]. For example, Ref. [KKN$^+$19] employs the Gauss-Hermite quadrature rule as a regularization scheme and the numerical results successfully confirm that the theory does belong to the Ising universality class. The same situation is also expected in the case of $d = 3$, that is, the three-dimensional lattice ϕ^4 theory is expected to belong to the three-dimensional Ising universality class. So far, no TRG calculation has been made for the three-dimensional ϕ^4 theory, we firstly investigate the critical behavior in three dimensions.

As the four-point coupling constant, we set $\lambda = 40$. This choice may help us avoid the weak coupling regime and Eq. (4.1) describes a finite-λ generalization of the Ising model. We first show the convergence of the free energy as a function of the regularization parameter K and the bond dimension D, defining the relative errors,

$$\delta_K = \left| \frac{\ln Z(K, D = 90) - \ln Z(K = 2000, D = 90)}{\ln Z(K = 2000, D = 90)} \right|, \qquad (4.12)$$

and

$$\delta_D = \left| \frac{\ln Z(K = 2000, D) - \ln Z(K = 2000, D = 90)}{\ln Z(K = 2000, D = 90)} \right|. \tag{4.13}$$

In Fig. 4.1, we show δ_K with $D = 90$ on the lattice whose volume is $V = 4096^3$ at $\kappa = 0.112859$ and 0.112920. As we will see below, $\kappa = 0.112859$ is in the symmetric phase at the vicinity of the critical point, while $\kappa = 0.112920$ is in the symmetry-breaking phase. We observe a monotonic decrease of δ_K as a function of K. Since the double-well potential in the ϕ^4 theory becomes sharper for larger λ, we take a large number of K to achieve sufficient convergence for δ_K. Figure 4.2 shows the D dependence of δ_D, where δ_D reaches the order of 10^{-5} up to $D = 90$. In the following, we present the numerical results at $\lambda = 40$ with $K = 2000$ and $D = 90$.
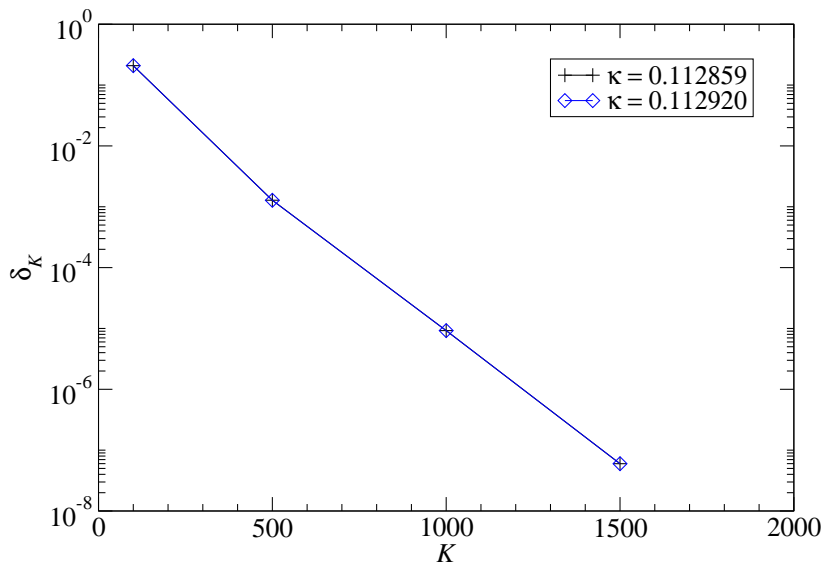
Figure 4.1: Convergence behavior of free energy with δ_K of Eq. (4.12)at $\kappa = 0.112859$ and 0.112920 as a function of K on $V = 4096^3$. We set $\lambda = 40$.

Secondly, let us investigate the bond energy E_b defined by

$$E_b = -\frac{1}{2} \frac{\partial}{\partial \kappa} \frac{\ln Z}{V}, \tag{4.14}$$

as a function of κ. Since 2κ corresponds to the inverse temperature β in the Ising model, the bond energy can be regarded as internal energy in the thermodynamic limit. The bond energy E_b is evaluated via the impurity tensor method, where we have a tensor network including adjacent impurity tensors to describe E_b. We show the bond energy as a function of κ on the 4096^3 lattice in Fig. 4.3, where the gray band with $0.11285890 \leq \kappa \leq 0.11285905$ in the inset graph denotes the location of the critical point determined by the quantity $X^{(m)}$, whose definition is same with Eq. (3.8). Although the value of E_b at $\kappa = 0.11285900$ is located in this gray band, this is due to the resulting behavior of $X^{(m)}$ at $\kappa = 0.11285900$, which does not show any clear plateau, $X^{(m)} = 1$ or 2. It should be emphasized that the bond energy on each lattice volume smoothly varies as a function of κ without
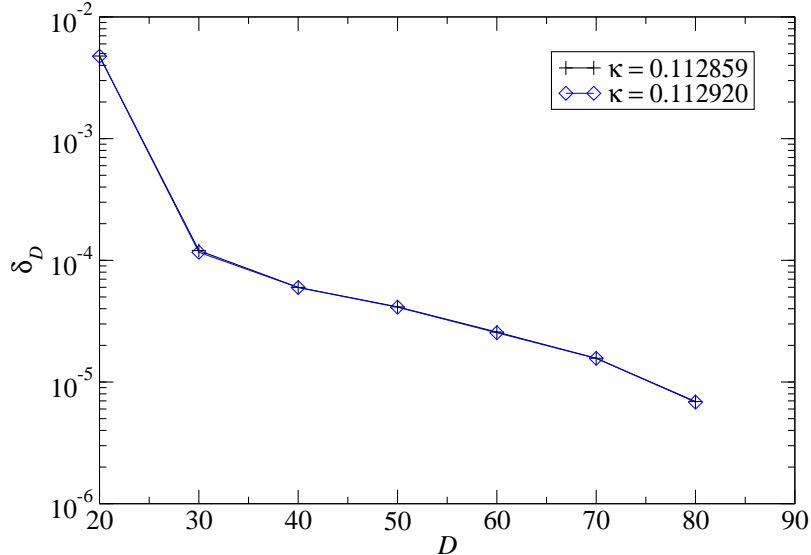
Figure 4.2: Same as Fig. 4.1 for δ_D of Eq. (4.13).

any gap. Moreover, there is no mutual crossing of curves for different volumes around the critical point. The curve of E_{b} monotonically reaches that on the largest lattice whose volume is 4096^3. As explained in Ref. [FMOU90], these are characteristic features of the second-order phase transition and the current numerical result indicates that the critical behavior takes place in the three-dimensional theory.

Thirdly, we evaluate the vacuum condensate $\langle\phi\rangle_{h=0}$, where h denotes an external field couples with $\phi(n)$. As the magnetization in the Ising model, $\langle\phi\rangle_{h=0}$ is an order parameter of the $\mathbb{Z}_2$-symmetry breaking. We calculate $\langle\phi\rangle_{h=0}$ with a one-point impurity tensor, introducing the external fields of $h = 1.0 \times 10^{-10}$ and 2.0×10^{-10} at each κ. After taking the infinite volume limit, we extrapolate the value of $\langle\phi\rangle$ at $h = 0$. In Fig. 4.4, we show $\langle\phi\rangle_{h=0}$ as a function of κ. To determine the critical point κ_{c} and extract the critical exponent β, we make a fit of $\langle\phi\rangle_{h=0}$ on 4096^3 lattice, which can be regarded as the thermodynamic limit. Employing the fitting form,

$$\langle\phi\rangle_{h=0} = A(\kappa - \kappa_{\mathrm{c}})^{\beta}, \tag{4.15}$$

on $\kappa \in [0.11285900, 0.11300000]$ in the symmetry-breaking phase, we obtain $A = 3.7(9)$, $\kappa_{\mathrm{c}} = 0.112859(6)$, and $\beta = 0.32(2)$. The resulting β is consistent with the recent HOTRG estimate, $\beta \approx 0.3295$ [XCQ+12], and the MC one, $\beta \approx 0.3264$ [Has10], in the three-dimensional Ising model. Therefore, current numerical results both for the bond energy E_{b} and the vacuum condensation $\langle\phi\rangle_{h=0}$ show consistency with the second-order phase transition in the universality class of the three-dimensional Ising model.

4.4   Four-dimensional theory

Now, let us move on to the case in $d = 4$. Here, the main concern is whether the system undergoes the second-order phase transition as expected in the mean-field theory or the (weak) first-order phase
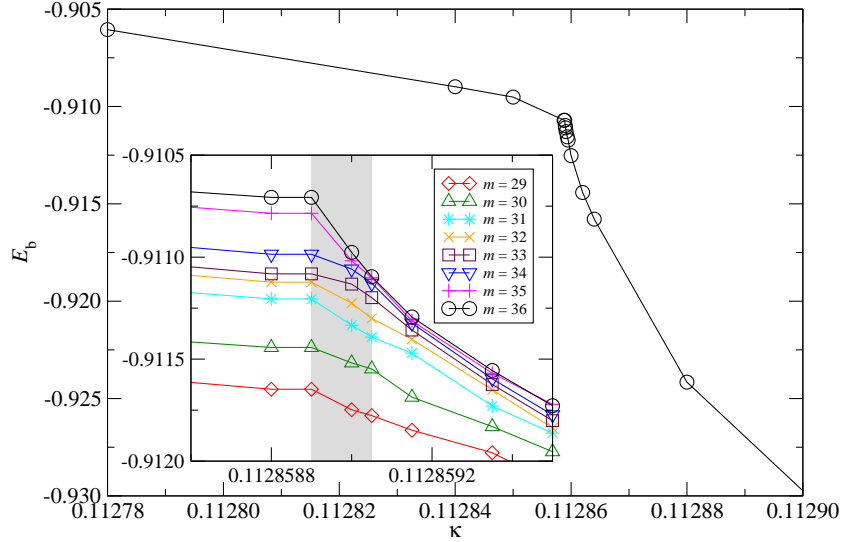
Figure 4.3: Three-dimensional bond energy as a function of κ on $V = 4096^3$ ($m = 36$). Inset graph shows it for various lattice sizes and gray band restricts the location of κ_{c} by $X^{(m)}$.
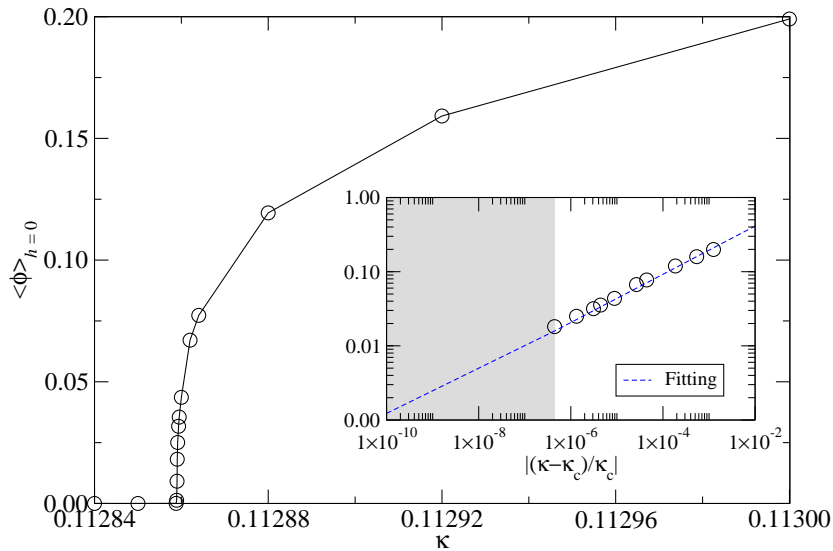
Figure 4.4: Three-dimensional vacuum condensation $\langle\phi\rangle_{h=0}$ as a function of κ on $V = 4096^3$. Inset graph also shows $\langle\phi\rangle_{h=0}$ together with the fitting result (dotted line) as a function of the reduced parameter $|(\kappa - \kappa_{\mathrm{c}})/\kappa_{\mathrm{c}}|$ on a logarithmic scale. Gray band indicates κ_{c} estimated by $X^{(m)}$.

transition as expected by the HOTRG calculation, assuming the same universality class of the four-dimensional Ising model. We begin with checking the convergence behaviors with respect to the regularization parameter K and the bond dimension D via the quantities,

$$\delta_K = \left| \frac{\ln Z(K, D = 50) - \ln Z(K = 2000, D = 50)}{\ln Z(K = 2000, D = 50)} \right|, \qquad (4.16)$$

$$\delta_D = \left| \frac{\ln Z(K = 2000, D) - \ln Z(K = 2000, D = 50)}{\ln Z(K = 2000, D = 50)} \right|. \qquad (4.17)$$

For comparison, we also set $\lambda = 40$, as in the three-dimensional study. Figure 4.5 shows δ_K with $D = 50$ on $V = 1024^4$ at $\kappa = 0.0763059$ and 0.0765000, which are in the symmetric and symmetry-breaking phases, respectively. Note that $\kappa = 0.0763059$ is close to the transition point κ_c, as we will see below. We observe that δ_K decreases monotonically as a function of K and reaches the order of 10^{-7} around $K = 1500$. This shows that the Gauss-Hermite quadrature method is not affected by whether the system is in the symmetric or symmetry-breaking phase. We also plot the δ_D in Fig. 4.6. Although Fig. 4.6 shows the fluctuation of free energy, it is suppressed as $\delta_D \approx 10^{-5}$ up to $D = 50$. It is worth emphasizing that the achieved order of δ_D is comparable with the three-dimensional one as shown in Fig. 4.2.
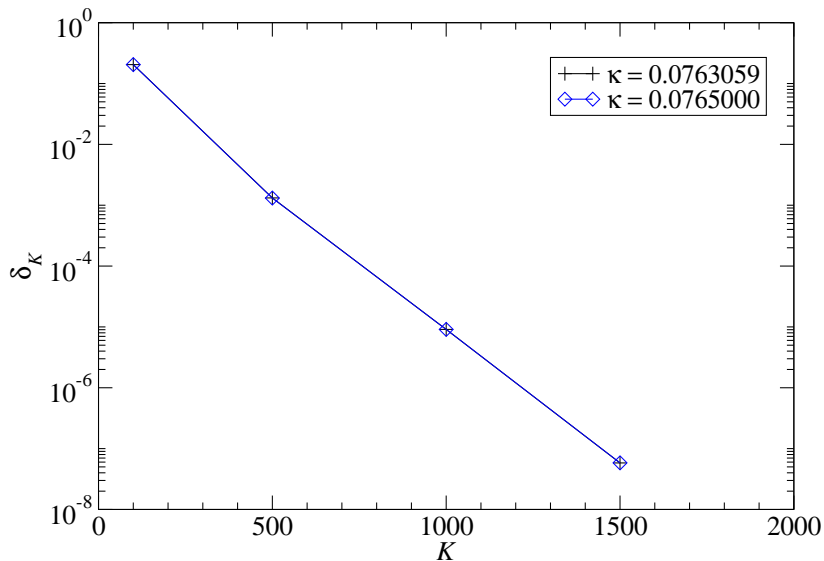
Figure 4.5: Convergence behavior of free energy with δ_K of Eq. (4.16) at $\kappa = 0.0763059$ and 0.0765000 as a function of K on $V = 1024^4$.

It is worth making some comparisons between the TRG approach and the other methods to check the reliability of the current study because the four-dimensional TRG computation is more challenging than the three-dimensional one. To this aim, we calculate κ_c at $\lambda = 5$ and compare it with the previous results obtained by various methods including the MC simulation [AdFGW13]. At $\lambda = 5$, we have found that the converging behavior in the free energy to the bond dimension becomes slightly slower
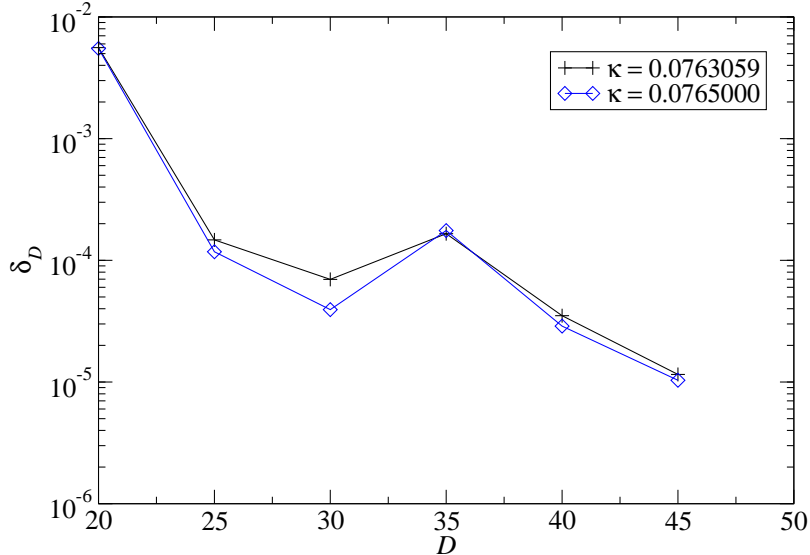
Figure 4.6: Same as Fig. 4.5 for δ_D of Eq. (4.17).

than that with $\lambda = 40$, so we take $D = 55$ and $K = 2000$ to evaluate κ_c at $\lambda = 5$. Up to $D = 55$, the relative error for the free energy is suppressed to $\mathcal{O}(10^{-5})$, which is the same extent with the case of $\lambda = 40$. Figure 4.7 shows the history of $X^{(m)}$ at $\kappa = 0.089225$ and 0.089300, whose difference $\Delta\kappa = 7.5 \times 10^{-5}$ is the finest resolution across the transition point. We find $X^{(m)} = 1$ for $m \gtrsim 30$ at $\kappa = 0.089225$ and $X^{(m)} = 2$ for $m \gtrsim 25$ at $\kappa = 0.089300$. This observation, on the 1024^4 lattice, allows us to restrict the location of κ_c by $\kappa_c = 0.0892625(375)$, whose error bar is provided by the resolution of κ. In Fig. 4.8, we see that our result is comparable to the MC result, $\kappa_c = 0.08893(20)$, in Ref. [AdFGW13]. A slight deviation from the MC result might be attributed to the finite-size effect because the MC simulation in Ref. [AdFGW13] is carried out on a lattice whose volume is 32^4, which is much smaller than 1024^4.

Now, let us turn on to the case of $\lambda = 40$. As in the $\lambda = 5$ computation, we determine κ_c at $\lambda = 40$, but with $D = 50$ and $K = 2000$, via observing the history of $X^{(m)}$ with respect to m. The result is $\kappa_c = 0.076305975(25)$ on the 1024^4 lattice, whose error bar is provided by the resolution of κ. Here, we make another numerical comparison between the current TRG approach with the previous HOTRG study of the four-dimensional Ising model. Since the Ising model at the temperature T can be regarded as the limit of $\lambda \to \infty$ in Eq. (4.1) with $2\kappa = 1/T$, we can see how κ_c approaches to the Ising limit as a function of λ. In Fig. 4.9, we check the $1/\lambda$ dependence of κ_c toward the Ising limit, where the result at $\lambda = 100$ is obtained in the same way as the $\lambda = 40$ with $D = 50$ and $K = 2000$. The error bars are provided by the resolution of κ but they are all within symbols. We can see that κ_c's at finite λ monotonically approach to the Ising limit. Fig. 4.9 also justifies that the choice of $\lambda = 40$ does play a role of finite-λ generalization of the Ising model, as mentioned previously.

We now turn to the investigation of the phase transition by the bond energy E_b. As in the three-dimensional study, E_b is evaluated with the impurity tensor method. Figure 4.10 plots the bond energy as a function of κ on the 1024^4 lattice. The resolution of κ becomes finer toward the transition point and the finest one is $\Delta\kappa = 5.0 \times 10^{-8}$ in the vicinity of the transition point. The location of the
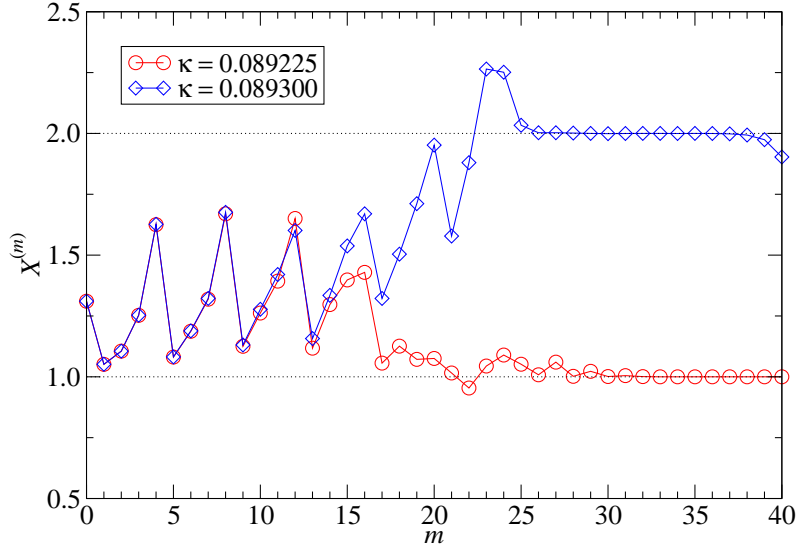
Figure 4.7: History of $X^{(m)}$ as a function of the coarse-graining step m at $\kappa = 0.089225$ (circle) and 0.089300 (diamond).
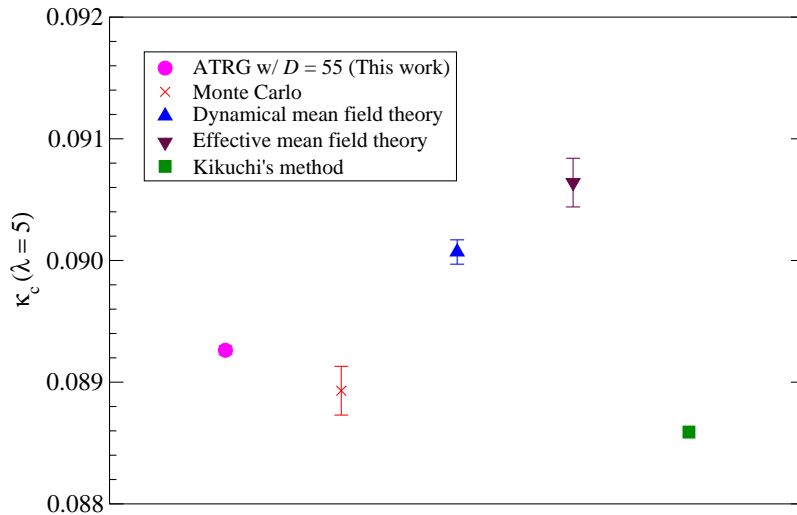
Figure 4.8: Comparison of κ_c at $\lambda = 5$ obtained by various methods. All numerical values except for the ATRG result are taken from Table III in Ref. [AdFGW13]. For details on the dynamical or effective mean field theory, see Ref. [AdFGW13]. For Kikuchi's method, see Ref. [Kik51].
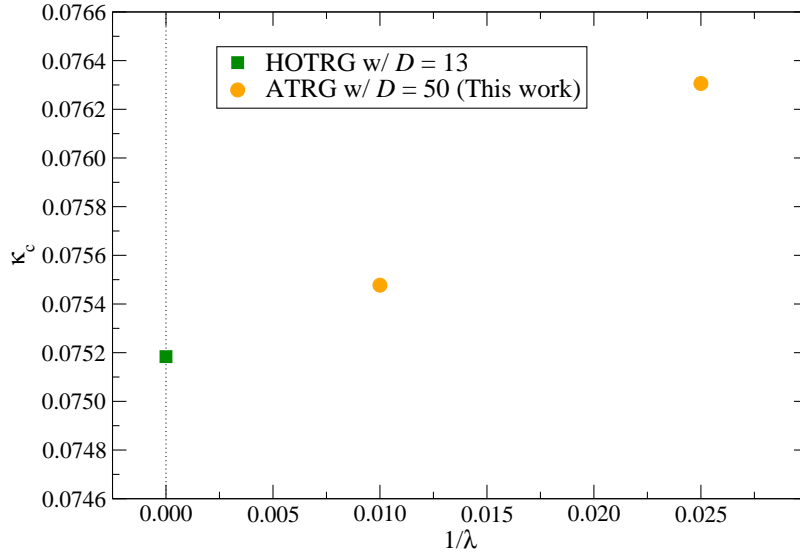
Figure 4.9: κ_c as a function of $1/\lambda$. $1/\lambda = 0$ corresponds to the Ising model. Square symbol at $1/\lambda = 0$ denotes the result obtained by the HOTRG [AKYY19]. All error bars are within symbols.

transition point in E_b is consistent with κ_c determined by $X^{(m)}$, which is shown by the gray band. The inset graph in Fig. 4.10 shows an emergent finite gap with mutual crossings of curves for different volumes, $m \geq 23$, around κ_c. These are characteristic features of the first-order phase transition as discussed in Ref. [FMOU90]. As the latent heat, we obtain

$$\Delta E_b = 0.001318(3), \tag{4.18}$$

with the linear extrapolation toward κ_c from different phases. In this extrapolation, we have used data points in $[0.07630560, 0.07630595]$ for the symmetric phase and $[0.0763060, 0.0763064]$ for the symmetry-breaking phase. Fig. 4.10 should be compared with Fig. 3.8, where gaps are started to be generated in similar lattice volumes. It should also be remarking that the value of ΔE_b is smaller than the latent heat $\Delta E = 0.0034(5)$ found in the Ising case with the HOTRG [AKYY19].

Finally, we evaluate the vacuum condensate of the scalar field $\langle \phi \rangle_{h=0}$, which is an order parameter of spontaneous breaking of the $\mathbb{Z}_2$ symmetry. As in the three-dimensional investigation, we calculate $\langle \phi \rangle$ by introducing the external fields of $h = 1.0 \times 10^{-10}$ and 2.0×10^{-10} at each κ. After taking the infinite volume limit, we extrapolate the value of $\langle \phi \rangle$ at $h = 0$. Figure 4.11 shows $\langle \phi \rangle_{h=0}$ as a function of κ. The resolution of κ is the same as that in Fig. 4.10. We find that the value of κ_c, where the vacuum condensation sets in, is consistent with both estimates obtained by $X^{(m)}$ and the bond energy. A finite jump in $\langle \phi \rangle_{h=0}$ at κ_c is another indication of the first-order phase transition. We find

$$\Delta \langle \phi \rangle_{h=0} = 0.0105(9), \tag{4.19}$$

as the value of finite jump, where we have used data points in $[0.07630560, 0.07630595]$ for the symmetric phase and $[0.0763060, 0.0763064]$ for the broken symmetry phase, as in the case with the bond energy, to extrapolate linearly the values of $\langle \phi \rangle_{h=0}$ toward κ_c. Note that this quantity is estimated as $0.037(2)$ in the Ising case with the HOTRG [AKYY19]. Therefore, the gap shrinks as E_b does.
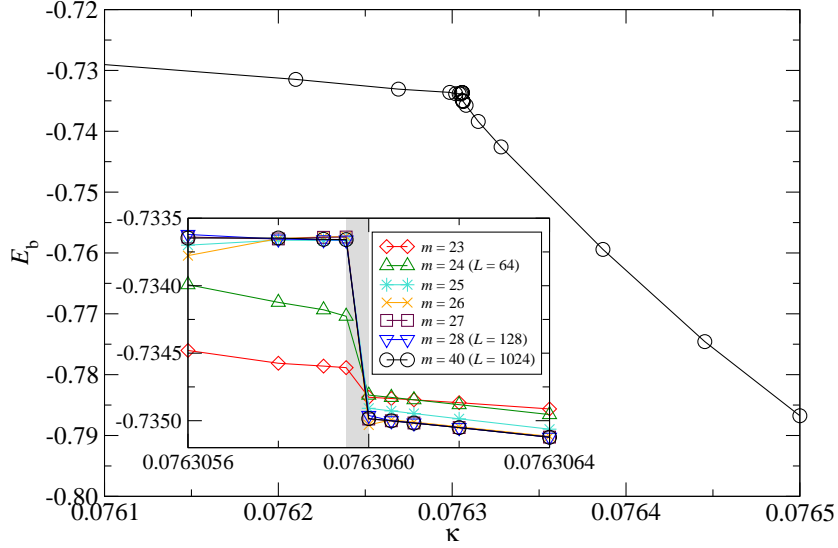
Figure 4.10: Bond energy as a function of κ on $V = 1024^4$. Inset graph shows it for various lattice sizes and gray band denotes κ_c estimated by $X^{(m)}$.
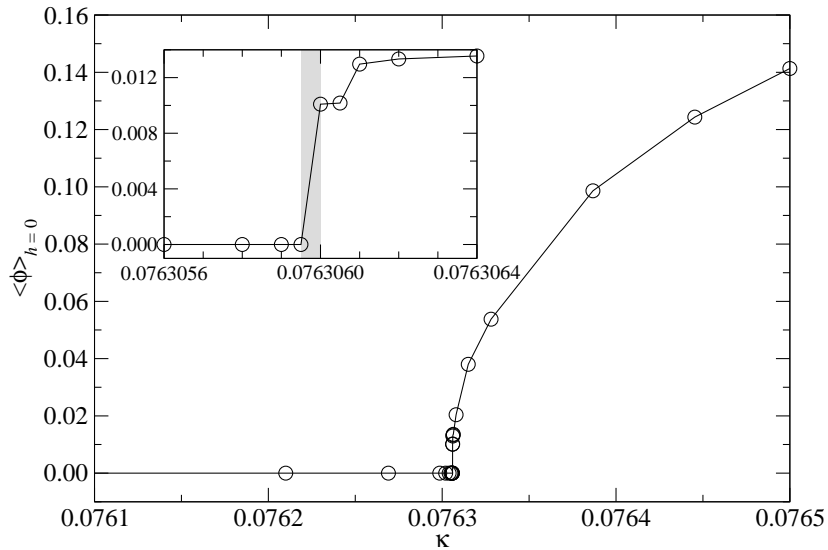
Figure 4.11: Vacuum condensation $\langle\phi\rangle_{h=0}$ as a function of κ on $V = 1024^4$. Gray band in inset graph shows κ_c estimated by $X^{(m)}$.

4.5 Discussion

So far, we have investigated the higher-dimensional Ising model and lattice ϕ^4 theories. The TRG approach successfully finds the second-order phase transitions in three dimensions, which is consistent with the previous numerical studies including the MC simulations. In four dimensions, the situation is much different. These TRG studies imply the scenario of weak first-order phase transition in the Ising model, also in its finite-λ generalization. In the contest of the triviality issue, this scenario supports the triviality in four dimensions, because the first-order transition does not allow us to take a continuum limit of lattice ϕ^4 theory. After our investigations, the scenario of the weak first-order phase transition in the Ising model or the ϕ^4 theory has been phenomenologically discussed in some studies [CCC19, CC20b, CC20a].

From the viewpoint of the more mathematical treatment of the Ising model or lattice ϕ^4 theory, the first-order phase transition in four dimensions might be less possible. For instance, Ref. [ADS15] provides proof that the spontaneous magnetization vanishes continuously at the critical point in the ferromagnetic Ising model with $d \geq 2$. [2] This is not confirmed in the current TRG computation. One of the ways to deal with this problem can be provided by some finite-D scaling in the TRG calculation. However, since Fig. 4.6 shows non-monotonic behavior for D, it is difficult to be carried out within the current study. A much larger bond dimension may be required in this research direction.

One of the main concerns is whether the mean-field prediction is reliable on the upper critical dimension of the Ising model. To think of this concern, it must be instructive to employ a method that can consider the effect of fluctuations neglected in the mean-field approximation. One of such improved mean-field calculations is known as the dynamical mean-field theory (DMFT). The DMFT has applied to ϕ^4 theories in various dimensions in Ref. [AdFGW13], where although the method incorrectly predicts the first-order transition for any λ in two- or three-dimensional theories, the extrapolation away from the transition point allows one to obtain the correct critical coupling and exponents. In the four-dimensional DMFT, the authors in Ref. [AdFGW13] have found the weak first-order transition in the strong coupling regime. It may imply that there is a first-order nature in the large-λ region.

---

[2]The author thanks Sinya Aoki, Takashi Hara, and Hal Tasaki, for their helpful comments.

5   Complex ϕ^4 theory at finite density

Our next target is a bosonic system with the sign problem. Since the TRG approach does not rely on a probabilistic interpretation for the given Boltzmann weight, the method must be free from the sign problem. Here, we consider the complex ϕ^4 theory at finite chemical potential, which is a typical system with the sign problem. This model has a characteristic feature called the Silver Blaze phenomenon, which has been studied by various methods intended to overcome or tame the sign problem, such as the complex Langevin approach [Aar09a], the thimble method [CDRMS13,FHK+13,MKO18], and the world-line representation [GK13,OG18]. The efficiency of the TRG method for this model has been confirmed in Ref. [KKN+20], which is a two-dimensional study. Employing the parallelized ATRG algorithm, we consider the model in four dimensions. This section is based on Ref. [AKK+20], which is the first application of the TRG approach to the four-dimensional quantum field theory.

5.1   Sign problem

The sign problem is an infamous numerical difficulty, which takes place when one applies the MC method to a certain type of system. Here, let us briefly see it. A main goal of the MC method is to estimate

$$\langle O(x) \rangle = \frac{\int \mathrm{d}x\, O(x)\, \mathrm{e}^{-S(x)}}{\int \mathrm{d}x\, \mathrm{e}^{-S(x)}}, \tag{5.1}$$

where $x \in \mathbb{R}^n$ denotes some dynamical variable and $S(x)$ represents an action. $O(x)$ is an observable whose expectation value is denoted by $\langle O(x) \rangle$. With the condition of $S(x) \in \mathbb{R}$, we can identify

$$\frac{\mathrm{e}^{-S(x)}}{\int \mathrm{d}x\, \mathrm{e}^{-S(x)}} \tag{5.2}$$

as a probability distribution function. In the Markov chain MC (MCMC) simulation, one generates a sample $\{x^{(i)}\}_{i=1,\cdots,N_{\mathrm{conf}}}$ based on Eq. (5.2) where N_{conf} denotes the sample size. Then $\langle O(x) \rangle$ is estimated by

$$\langle O(x) \rangle \approx \frac{1}{N_{\mathrm{conf}}} \sum_{i=1}^{N_{\mathrm{conf}}} O(x^{(i)}). \tag{5.3}$$

Unfortunately, when $S(x) \notin \mathbb{R}$, we can no longer regard Eq. (5.2) as a probability distribution function. A naive way to deal with such a complex action is provided by the reweighting method, where we regard

$$\frac{\mathrm{e}^{-\Re(S(x))}}{\int \mathrm{d}x\, \mathrm{e}^{-\Re(S(x))}} \tag{5.4}$$

as a probability distribution and estimate $\langle O(x) \rangle$ via

$$\langle O(x) \rangle = \frac{\left\langle O(x)\mathrm{e}^{-\mathrm{i}\Im(S(x))} \right\rangle_{\mathrm{pq}}}{\left\langle \mathrm{e}^{-\mathrm{i}\Im(S(x))} \right\rangle_{\mathrm{pq}}}, \tag{5.5}$$

where $\langle \cdot \rangle_{\mathrm{pq}}$ represents an expectation value evaluated by Eq. (5.4). For the ratio in the right-hand side of Eq. (5.5), one has

$$\frac{\left\langle O(x)\mathrm{e}^{-\mathrm{i}\Im(S(x))} \right\rangle_{\mathrm{pq}}}{\left\langle \mathrm{e}^{-\mathrm{i}\Im(S(x))} \right\rangle_{\mathrm{pq}}} \approx \frac{\mathrm{e}^{-\mathcal{O}(n)} \pm \mathcal{O}(1/\sqrt{N_{\mathrm{conf}}})}{\mathrm{e}^{-\mathcal{O}(n)} \pm \mathcal{O}(1/\sqrt{N_{\mathrm{conf}}})}, \tag{5.6}$$

which requires the statistical error to be smaller than $\mathrm{e}^{-\mathcal{O}(n)}$. This requirement is equivalent to the condition,

$$N_{\mathrm{conf}} \gtrsim \mathrm{e}^{\mathcal{O}(n)}, \tag{5.7}$$

that is, one has to make N_{conf} exponentially large. This is the so-called sign problem, where the MCMC simulation of the system with large degrees of freedom is hindered by Eq. (5.7). Note that the sign problem is caused by the probabilistic interpretation, which is essentially required in the MC method.

5.2 Formulation on a four-dimensional lattice

The complex ϕ^4 theory at finite density on a four-dimensional lattice is defined via the following action,

$$S[\phi] = \sum_{n \in \Lambda_4} \left[(8 + m^2)|\phi(n)|^2 + \lambda|\phi(n)|^4 - \sum_{\nu=1}^{4} \left(\mathrm{e}^{\mu\delta_{\nu,4}}\phi(n)^*\phi(n+\hat{\nu}) + \mathrm{e}^{-\mu\delta_{\nu,4}}\phi(n)\phi(n+\hat{\nu})^* \right) \right], \tag{5.8}$$

with the complex scalar field $\phi(n)$, the bare mass m, the quartric coupling constant $\lambda > 0$ and the chemical potential μ. When $\mu = 0$, $S[\phi] \in \mathbb{R}$ and there is no sign problem, but once we consider the theory at finite μ, $S[\phi]$ takes its value on $\mathbb{C}$ and we encounter the sign problem.

Although there is a several choices to express the complex scalar fields, we consider the polar-coordinate representation, $\phi(n) = r(n)\mathrm{e}^{\mathrm{i}\pi\theta(n)}$. Then the path integral is given by

$$Z = \left(\prod_{n \in \Lambda_4} \int_0^\infty r(n)\mathrm{d}r(n) \int_{-1}^1 \pi\mathrm{d}\theta(n) \right) \exp\left[-S[r,\theta]\right], \tag{5.9}$$

with

$$S[r,\theta] = \sum_{n \in \Lambda_4} \left[(8 + m^2)r(n)^2 + \lambda r(n)^4 - 2\sum_{\nu=1}^{4} r(n)r(n+\hat{\nu})\cos\left[\pi\left\{\theta(n+\hat{\nu}) - \theta(n)\right\} - \mathrm{i}\mu\delta_{\nu,4}\right] \right]. \tag{5.10}$$

5.3 Tensor network representation

Since there are two continuous variables $r(n)$ and $\theta(n)$, whose value ranges are different, we employ two kinds of regularization schemes. We regularize $r(n)$ by the Gauss-Laguerre quadrature rule and $\theta(n)$ by the Gauss-Legendre quadrature rule. Regularization parameters are K_1 and K_2, respectively. See Appendix B for the details of the quadrature rules employed here. Using the vector notation introduced in Eq. (2.16), the regularized path integral $Z(K_1, K_2)$ is given by

$$Z(K_1, K_2) = \left(\prod_{n \in \Lambda_4} \sum_{\tilde{r}(n)} \tilde{r}(n) v_{\tilde{r}(n)} \mathrm{e}^{\tilde{r}(n)} \sum_{\tilde{\theta}(n)} w_{\tilde{\theta}(n)} \pi \right)$$

$$\times \prod_{n \in \Lambda_4} \exp\left[-(8+m^2)\tilde{r}(n)^2 + \lambda\tilde{r}(n)^4 + 2\sum_{\nu=1}^{4} \tilde{r}(n)\tilde{r}(n+\hat{\nu})\cos\left[\pi\left\{\tilde{\theta}(n+\hat{\nu}) - \tilde{\theta}(n)\right\} - \mathrm{i}\mu\delta_{\nu,4}\right] \right], \tag{5.11}$$

where v and w denote the weights in quadrature rules. We define a hopping matrix as

$$
\begin{aligned}
&T_{\tilde{r}(n)\tilde{\theta}(n),\tilde{r}(n+\hat{\nu})\tilde{\theta}(n+\hat{\nu})} \\
&= \sqrt[4]{\pi} \sqrt[8]{\tilde{r}(n)v_{\tilde{r}(n)}\mathrm{e}^{\tilde{r}(n)}w_{\tilde{\theta}(n)}\tilde{r}(n+\hat{\nu})v_{\tilde{r}(n+\hat{\nu})}\mathrm{e}^{\tilde{r}(n+\hat{\nu})}w_{\tilde{\theta}(n+\hat{\nu})}} \\
&\quad \times \exp\left[-\left(1+\frac{m^2}{8}\right)\left(\tilde{r}(n)^2+\tilde{r}(n+\hat{\nu})^2\right)-\frac{\lambda}{8}\left(\tilde{r}(n)^4+\tilde{r}(n+\hat{\nu})^4\right)\right] \\
&\quad \times \exp\left[2\tilde{r}(n)\tilde{r}(n+\hat{\nu})\cos\left[\pi\left\{\tilde{\theta}(n+\hat{\nu})-\tilde{\theta}(n)\right\}-\mathrm{i}\mu\delta_{\nu,4}\right]\right),
\end{aligned} \tag{5.12}
$$

which is a $K_1K_2 \times K_1K_2$ matrix. We then apply the SVD for the hopping matrix, which gives us

$$
T_{\tilde{r}(n)\tilde{\theta}(n),\tilde{r}(n+\hat{\nu})\tilde{\theta}(n+\hat{\nu})} = \sum_{i_\nu(n)} U_{\tilde{r}(n)\tilde{\theta}(n),i_\nu)(n)}s_{i_\nu(n)}V^*_{\tilde{r}(n+\hat{\nu})\tilde{\theta}(n+\hat{\nu}),i_\nu(n)}. \tag{5.13}
$$

One must be ready to obtain a tensor network representation for $Z(K_1,K_2)$ as in the form of Eq. (2.12) with a local tensor,

$$
\mathcal{T}_{i_1(n)i_2(n)i_3(n)i_4(n)i'_1(n)i'_2(n)i'_3(n)i'_4(n)} = \sum_{\tilde{r}}\sum_{\tilde{\theta}}\prod_{\nu=1}^4 U_{\tilde{r}\tilde{\phi},i_\nu(n)}V^*_{\tilde{r}\tilde{\theta}(n),i'_\nu(n)}\sqrt{s_{i_\nu(n)}}\sqrt{s_{i'_\nu(n)}}. \tag{5.14}
$$

5.4 Algorithmic-parameter dependence

We choose $m=0.1$ and $\lambda=1.0$ in Eq. (5.10). [1] Let us firstly check an algorithmic-parameter dependence of the thermodynamic potential. In the TRG calculation, we have two algorithmic parameters. One is the regularization-parameter dependence. For simplicity, we set $K=K_1=K_2$ in the following. The other is finite-bond dependence. Figure 5.1 shows the K dependence of the thermodynamic potential with $D=45$ on $V=1024^4$ choosing $\mu=0.6$, which is close to the critical chemical potential, as we will see below. A converging behavior indicates that current regularization schemes nicely work for this theory. On the other hand, Fig. 5.2 shows the D dependence of the thermodynamic potential with $K=64$, which seems converged around $D \sim 40$.

5.5 Average phase factor

The phase-quenched theory is defined by the real part of the action, whose path integral is given by

$$
Z_{\mathrm{pq}} = \left(\prod_{n\in\Lambda_4}\int\mathrm{d}\phi(n)\right)\exp\left[-\Re(S[\phi])\right]. \tag{5.15}
$$

The phase-quenched theory is employed in the reweighting method, where an expectation value of an observable O is considered via

$$
\begin{aligned}
\langle O \rangle &= \frac{\left(\prod_{n\in\Lambda_4}\int\mathrm{d}\phi(n)\right)O\exp\left[-S[\phi]\right]}{\left(\prod_{n\in\Lambda_4}\int\mathrm{d}\phi(n)\right)\exp\left[-S[\phi]\right]} \\
&= \frac{\left(\prod_{n\in\Lambda_4}\int\mathrm{d}\phi(n)\right)O\mathrm{e}^{\mathrm{i}\theta}\exp\left[-\Re(S[\phi])\right]/\left(\prod_{n\in\Lambda_4}\int\mathrm{d}\phi(n)\right)\exp\left[-\Re(S[\phi])\right]}{\left(\prod_{n\in\Lambda_4}\int\mathrm{d}\phi(n)\right)\mathrm{e}^{\mathrm{i}\theta}\exp\left[-\Re(S[\phi])\right]/\left(\prod_{n\in\Lambda_4}\int\mathrm{d}\phi(n)\right)\exp\left[-\Re(S[\phi])\right]} \\
&= \frac{\langle O\mathrm{e}^{\mathrm{i}\theta}\rangle_{\mathrm{pq}}}{\langle\mathrm{e}^{\mathrm{i}\theta}\rangle_{\mathrm{pq}}},
\end{aligned} \tag{5.16}
$$

---

[1]These parameters are the same as employed in the two-dimensional study [KKN+20].
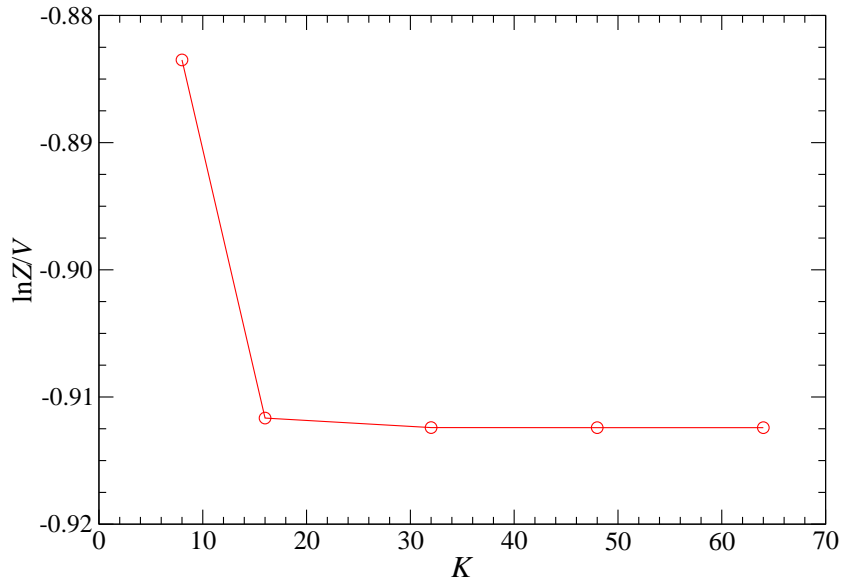
Figure 5.1: K dependence of thermodynamic potential with $m^2 = 0.01$, $\lambda = 1.0$, $\mu = 0.6$ and $D = 45$ on $V = 1024^4$.
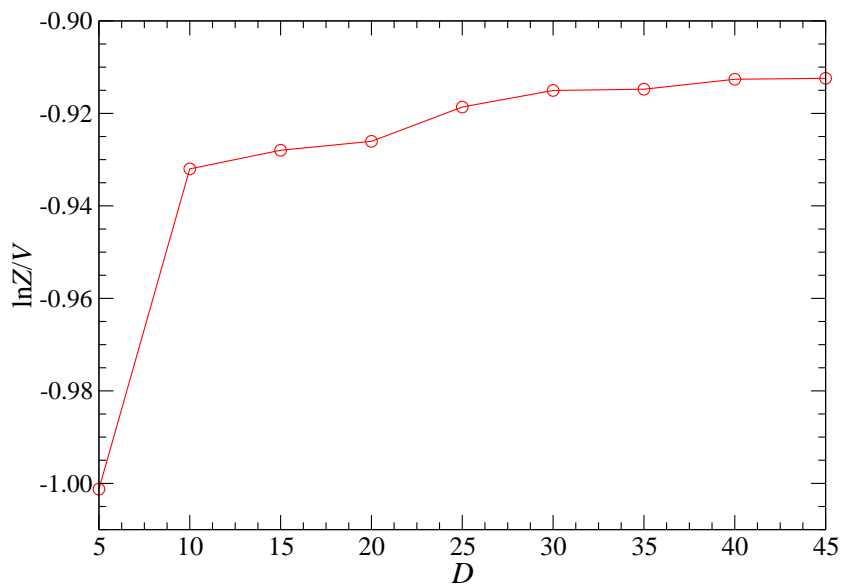
Figure 5.2: D dependence of thermodynamic potential density with $m^2 = 0.01$, $\lambda = 1.0$, $\mu = 0.6$ and $K = 64$ on $V = 1024^4$.

as we explained previously. θ denotes $-\Im(S[\phi])$, which corresponds to the imaginary part of the action, and $\langle\cdot\rangle_{\mathrm{pq}}$ represents an expectation value evaluated by the phase-quenched theory. Therefore, the aim of reweighting method is to evaluate the ratio of $\langle Oe^{i\theta}\rangle_{\mathrm{pq}}$ and $\langle e^{i\theta}\rangle_{\mathrm{pq}}$. When one is in the regime where the average of the phase factor oscillates frequently, it is difficult for the Monte Carlo method to evaluate the ratio because of the vanishing contributions from both the numerator and the denominator. In Fig. 5.3, we show the average phase factor $\langle e^{i\theta}\rangle_{\mathrm{pq}}$ as a function of chemical potential, varying the lattice volume. This quantity is usually employed to measure how severe the sign problem is for the parameter regime one considers. It is clear that $\langle e^{i\theta}\rangle_{\mathrm{pq}}$ vanishes at finite density region, enlarging the lattice volume. On the lattice with the volume $V = 1024^4$, which can be identified as the thermodynamic limit at zero temperature, the average phase factor quickly falls off from one at $\mu = 0$ to zero for $\mu \geq 0.05$, where the Monte Carlo simulation is hindered by the severe sign problem.
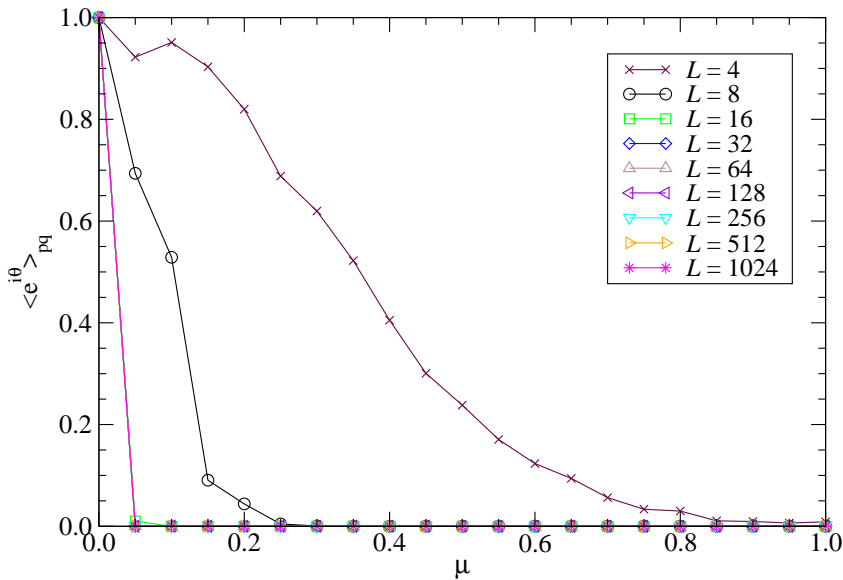
Figure 5.3: Average phase factor as a function of μ with $m^2 = 0.01$, $\lambda = 1.0$, $K = 64$, $D = 45$. The lattice volume V is varied from 4^4 to 1024^4.

5.6   Silver Blaze Phenomenon

When a system possesses a matter mass gap m, it is expected that the matter number density remains zero as long as the chemical potential μ is smaller than m in the thermodynamic and zero-temperature limit. This type of behavior was referred to as the Silver Blaze phenomenon or the Silver Blaze problem in Ref. [Coh03]. When the Silver Blaze phenomenon takes place, bulk observables become independent of μ up to some critical point μ_{c} in the thermodynamic limit with vanishing temperature.

The complex ϕ^4 theory at finite density is expected to show the Silver Blaze phenomenon, so we firstly compute the number density as a function of μ, whose definition is

$$\langle n \rangle = \frac{1}{V}\frac{\partial \ln Z}{\partial \mu}. \tag{5.17}$$

We evaluate this quantity via the impurity tensor method, where the tensor network representation of $\langle n \rangle$ is a network consisting of two impurities along the temporal direction. Fig. 5.4 shows the numerical result. One can confirm that on the larger volume toward the thermodynamic limit with vanishing temperature, the Silver Blaze phenomenon becomes manifest. In other words, the number density $\langle n \rangle$ stays around zero up to $\mu_c \approx 0.65$ and shows rapid increase beyond μ_c. It is instructive to compare $\langle n \rangle$ and $\langle n \rangle_{\mathrm{pq}}$, as shown in Figure 5.5. Both of them are calculated at finite density on the lattice whose volume is $V = 1024^4$. Since $\langle n \rangle_{\mathrm{pq}}$ monotonically increases once the chemical potential is turned on, we can see that the Silver Blaze phenomenon is attributed to the imaginary part of the action.
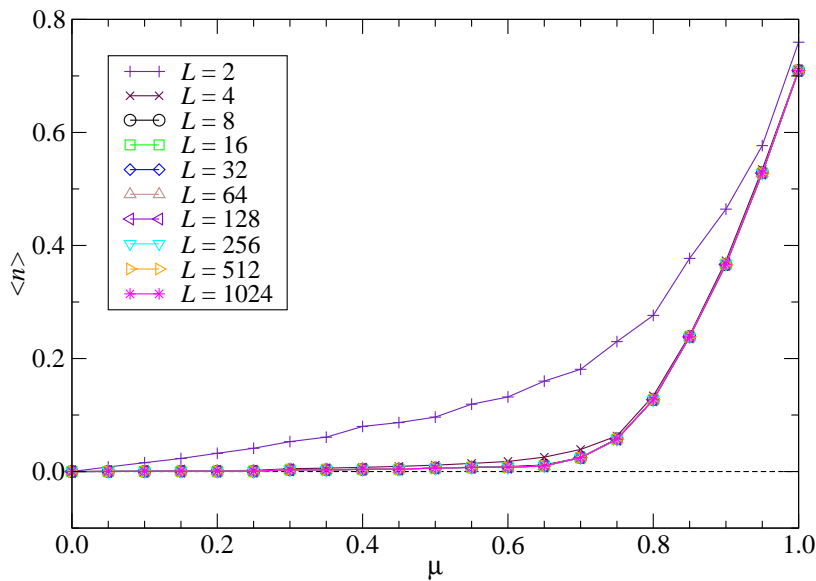
Figure 5.4: Number density as a function of μ with the lattice volume varied from 2^4 to 1024^4. Other parameters of m, λ, K and D are the same as those in Fig. 5.3.

The second observable we focus on is

$$\langle |\phi|^2 \rangle = \frac{1}{V} \frac{\partial \ln Z}{\partial m^2} \tag{5.18}$$

which is also evaluated with the impurity tensor method. The tensor network including one-point impurity gives this quantity. Figure 5.6 plots $\langle |\phi|^2 \rangle$ as a function of μ with the same parameter set as in Fig. 5.4. In Fig. 5.6, we can see that there is little μ dependence for $\mu < \mu_c \approx 0.65$. With $\mu > \mu_c$, $\langle |\phi|^2 \rangle$ rapidly increases. Therefore, we also observe the Silver Blaze phenomenon via the expectation value of $|\phi|^2$. It is worth noting that $\langle |\phi|^2 \rangle$ has a relation to the critical point within the mean-field theory such that

$$4 \sinh^2(\mu_c^{\mathrm{MF}}/2) = m^2 + 4\lambda \langle |\phi|^2 \rangle , \tag{5.19}$$

where μ_c^{MF} denotes the critical point obtained by the mean-field estimation [Aar09b]. Since $\langle |\phi|^2 \rangle \approx 0.125$ at $0 \leq \mu \leq 0.65$ as in Fig. 5.5, we obtain $\mu_c^{\mathrm{MF}} \approx 0.70$, which is comparable with the location of μ_c estimated by the current TRG calculation.
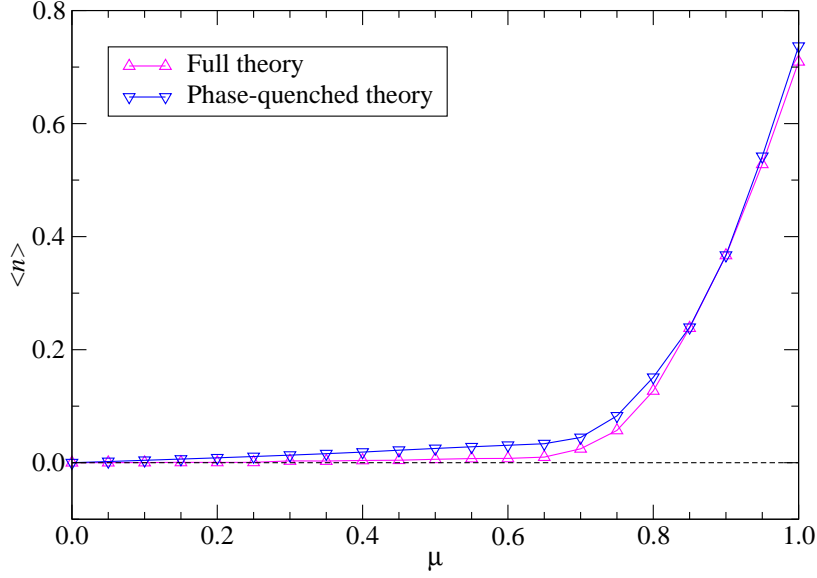
Figure 5.5: Comparison of $\langle n \rangle$ and $\langle n \rangle_{\mathrm{pq}}$ with $m^2 = 0.01$, $\lambda = 1.0$, $K = 64$ and $D = 45$ on $V = 1024^4$.
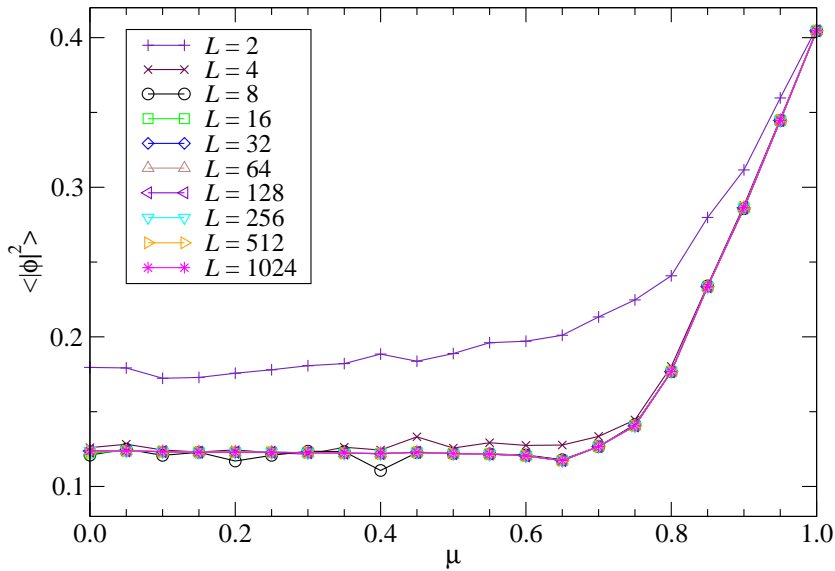
Figure 5.6: $\langle |\phi|^2 \rangle$ as a function of μ with the same parameter set of (m, λ, K, D, V) as in Fig. 5.4.

6 Hubbard model at finite density

In the following, we discuss the application of the TRG to lattice fermions. The path integral for a fermionic system is defined by the Grassmann integral, which is directly evaluated by the TRG approach. Our first target is the Hubbard model, which is a fundamental toy model of the strongly correlated non-relativistic electrons. Although the one-dimensional model is solved exactly by the Bethe ansatz, no exact solution has been known for this model with $d \geq 2$ except $d \to \infty$. In addition, away from the so-called half-filling state, the model encounters the sign problem, so it must be worth being investigated by the TRG.

6.1 The model

The Hubbard model describes interacting electrons in a crystalline solid under the screened long-range Coulomb forces between electrons to an on-site repulsive potential. The model on the d-dimensional lattice is defined by the following Hamiltonian,

$$\hat{H} = \sum_{\boldsymbol{x},\boldsymbol{y} \in \Lambda_d} \sum_{s=\uparrow,\downarrow} t_{\boldsymbol{x},\boldsymbol{y}} c^{\dagger}_{\boldsymbol{x}s} c_{\boldsymbol{y}s} + U \sum_{\boldsymbol{x}} n_{\boldsymbol{x}\uparrow} n_{\boldsymbol{x}\downarrow} - \mu \sum_{\boldsymbol{x}} \sum_{s} n_{\boldsymbol{x}s}, \tag{6.1}$$

where operators $c_{\boldsymbol{x}s}, c^{\dagger}_{\boldsymbol{x}s}$ satisfies

$$[c^{\dagger}_{\boldsymbol{x}s}, c_{\boldsymbol{y}s'}]_+ = \delta_{\boldsymbol{x},\boldsymbol{y}} \delta_{s,s'}, \tag{6.2}$$

$$[c^{\dagger}_{\boldsymbol{x}s}, c^{\dagger}_{\boldsymbol{y}s'}]_+ = [c_{\boldsymbol{x}s}, c_{\boldsymbol{y}s'}]_+ = 0 \tag{6.3}$$

and $n_{\boldsymbol{x}s} = c^{\dagger}_{\boldsymbol{x}s} c_{\boldsymbol{x}s}$. $t_{\boldsymbol{x},\boldsymbol{y}}$ is called the hopping matrix, which is

$$t_{\boldsymbol{x},\boldsymbol{y}} = \begin{cases} -t, & \text{if } \boldsymbol{x} \text{ and } \boldsymbol{y} \text{ are nearest neighbors,} \\ 0, & \text{else.} \end{cases} \tag{6.4}$$

$U > 0$ corresponds to the on-site repulsion. Notice that the first term in Eq. (6.1) is diagonalizable in the momentum space and the second term is diagonalized in the real space. In other words, the former describes electrons as "waves" and the latter does as "particles." For each lattice site $\boldsymbol{x} \in \Lambda_d$, there are four possible states; no electron, occupied with an electron $\uparrow$ or $\downarrow$, or with electrons $\uparrow$ and $\downarrow$. Consequently, the dimension of the state space is $4^{|\Lambda_d|}$. The expectation value of the number operator,

$$\hat{N} = \sum_{\boldsymbol{x}} \sum_{s} n_{\boldsymbol{x}s} \tag{6.5}$$

is restricted to $0 \leq \langle \hat{N} \rangle \leq 2|\Lambda_d|$. The spin operator $\hat{\boldsymbol{S}}_{\boldsymbol{x}} = (\hat{S}^{(x)}_{\boldsymbol{x}}, \hat{S}^{(y)}_{\boldsymbol{x}}, \hat{S}^{(z)}_{\boldsymbol{x}})$ is defined by

$$\hat{S}^{(i)}_{\boldsymbol{x}} = \frac{1}{2} \sum_{\alpha,\beta} c^{\dagger}_{\boldsymbol{x},\alpha} \sigma^{(i)}_{\alpha\beta} c_{\boldsymbol{x},\beta}, \tag{6.6}$$

where $\sigma^{(i)}$ $(i = x, y, z)$ is the Pauli matrices. Note that the total spin operator,

$$\hat{S}^{(i)}_{\text{tot}} = \sum_{\boldsymbol{x}} \hat{S}^{(i)}_{\boldsymbol{x}} \tag{6.7}$$

commutes with the Hamiltonian (6.1). One of the fundamental observables in the Hubbard model is the nearest-neighbor spin-spin correlation function,

$$\langle \hat{\boldsymbol{S}}_{\boldsymbol{x}} \cdot \hat{\boldsymbol{S}}_{\boldsymbol{y}} \rangle . \tag{6.8}$$

$\langle \hat{\boldsymbol{S}}_{\boldsymbol{x}} \cdot \hat{\boldsymbol{S}}_{\boldsymbol{y}} \rangle < 0$ implies that the system favors the antiferromagnetic ordering. In Ref. [FGP$^+$11], the spin-spin correlation function $\langle S_{\boldsymbol{x}}^{(z)} S_{\boldsymbol{x}+\boldsymbol{e}_i}^{(z)} \rangle$ is employed to investigate the regions close to the transition, for instance. [1]

6.2   One-site model

One-site Hubbard model, which is characterized by the vanishing hopping parameter $t = 0$, is easily solved. The Hamiltonian of Eq. (6.1) is reduced to be

$$\hat{H} = U n_\uparrow n_\downarrow - \mu n_\uparrow - \mu n_\downarrow, \tag{6.9}$$

which satisfies

$$\langle 0 | \hat{H} | 0 \rangle = 0, \tag{6.10}$$

$$\langle \uparrow | \hat{H} | \uparrow \rangle = \langle \downarrow | \hat{H} | \downarrow \rangle = -\mu, \tag{6.11}$$

$$\langle \uparrow\downarrow | \hat{H} | \uparrow\downarrow \rangle = U - 2\mu. \tag{6.12}$$

Then, the grand partition function is

$$Z = 1 + 2\mathrm{e}^{\beta\mu} + \mathrm{e}^{2\beta\mu - \beta U}, \tag{6.13}$$

from which one can obtain

$$N = \langle \hat{N} \rangle = \frac{\partial}{\partial \mu} \left(\frac{1}{\beta} \ln Z \right) = \frac{2\mathrm{e}^{\beta\mu} + 2\mathrm{e}^{2\beta\mu - \beta U}}{Z}. \tag{6.14}$$

Now, let us consider the case with $\mu = U/2$. One immediately finds

$$Z|_{\mu=U/2} = 2(1 + \mathrm{e}^{\beta\mu})\Big|_{\mu=U/2}, \tag{6.15}$$

and

$$N|_{\mu=U/2} = \frac{2(\mathrm{e}^{\beta\mu} + 1)}{Z}\Bigg|_{\mu=U/2} = 1. \tag{6.16}$$

This case corresponds to the system at half-filling. The half-filling is an interesting situation also in the case with $t \neq 0$. [2]

---

[1]The Curie temperature is the temperature above which certain systems lose their ferromagnetic ordering. Analogous to the Curie temperature, the Neél temperature is the one above which certain systems lose their antiferromagnetic ordering.

[2]It is convenient to introduce the shifted chemical potential as $\mu' := \mu - U/2$ in Eq. (6.1). Then, the Hamiltonian of Eq. (6.1) is expressed as

$$\hat{H} = \sum_{\boldsymbol{x},\boldsymbol{y}} \sum_{s=\uparrow,\downarrow} t_{\boldsymbol{x},\boldsymbol{y}} c_{\boldsymbol{x}s}^\dagger c_{\boldsymbol{y}s} + U \sum_{\boldsymbol{x}} \left(n_{\boldsymbol{x}\uparrow} - \frac{1}{2} \right) \left(n_{\boldsymbol{x}\downarrow} - \frac{1}{2} \right) - \mu' \sum_{\boldsymbol{x}} \sum_{s} n_{\boldsymbol{x}s} - \frac{U}{4} \sum_{\boldsymbol{x}} 1.$$

6.3 Free-electron model

The Hamiltonian of Eq. (6.1) in the limit $U \to 0$ describes nothing but the ideal Fermi gas. Here, we assume that the model is defined on the finite spatial volume, say $|\Lambda_d| = \prod_{i=1}^{d} N_i$. Expanding the operators in the Fourier modes,

$$c_{\boldsymbol{x},s} = \frac{1}{\sqrt{|\Lambda_d|}} \sum_{\boldsymbol{k}} \tilde{c}_{\boldsymbol{k},s} \exp\left[\sum_{i=1}^{d} \frac{2\pi \mathrm{i} k_i x_i}{N_i}\right], \tag{6.17}$$

$$c_{\boldsymbol{x},s}^{\dagger} = \frac{1}{\sqrt{|\Lambda_d|}} \sum_{\boldsymbol{k}} \tilde{c}_{\boldsymbol{k},s}^{\dagger} \exp\left[-\sum_{i=1}^{d} \frac{2\pi \mathrm{i} k_i x_i}{N_i}\right], \tag{6.18}$$

the Hamiltonian of Eq. (6.1) with $U = 0$ is written as

$$\hat{H} = \sum_{\boldsymbol{k},s} \left[-2t \sum_{i=1}^{d} \cos\left(\frac{2\pi k_i}{N_i}\right) - \mu\right] \tilde{c}_{\boldsymbol{k},s}^{\dagger} \tilde{c}_{\boldsymbol{k},s}. \tag{6.19}$$

[3] Setting

$$\varepsilon_{\boldsymbol{k}} = -2t \sum_{i=1}^{d} \cos\left(\frac{2\pi k_i}{N_i}\right), \tag{6.20}$$

which is nothing but the dispersion relation, the grand partition function is expressed as

$$Z = \prod_{\boldsymbol{k}} \prod_{s} \mathrm{Tr}_{\boldsymbol{k},s} \mathrm{e}^{-\beta(\varepsilon_{\boldsymbol{k}} - \mu)\tilde{c}_{\boldsymbol{k},s}^{\dagger} \tilde{c}_{\boldsymbol{k},s}}. \tag{6.21}$$

Since the eigenvalues of $\tilde{n}_{\boldsymbol{k},s} = \tilde{c}_{\boldsymbol{k},s}^{\dagger} \tilde{c}_{\boldsymbol{k},s}$ is 0 or 1,

$$\mathrm{Tr}_{\boldsymbol{k},s} \mathrm{e}^{-\beta(\varepsilon_{\boldsymbol{k}} - \mu)\tilde{c}_{\boldsymbol{k},s}^{\dagger} \tilde{c}_{\boldsymbol{k},s}} = \sum_{\tilde{n}_{\boldsymbol{k},s}=0,1} \mathrm{e}^{-\beta(\varepsilon_{\boldsymbol{k}} - \mu)\tilde{n}_{\boldsymbol{k},s}} = 1 + \mathrm{e}^{-\beta(\varepsilon_{\boldsymbol{k}} - \mu)} \tag{6.22}$$

holds. Therefore,

$$Z = \prod_{\boldsymbol{k}} \prod_{s} \left(1 + \mathrm{e}^{-\beta(\varepsilon_{\boldsymbol{k}} - \mu)}\right) = \prod_{\boldsymbol{k}} \left(1 + \mathrm{e}^{-\beta(\varepsilon_{\boldsymbol{k}} - \mu)}\right)^2 \tag{6.23}$$

Dropping the last term and redefining $\mu = \mu'$,

$$\hat{H} = \sum_{\boldsymbol{x},\boldsymbol{y}} \sum_{s=\uparrow,\downarrow} t_{\boldsymbol{x},\boldsymbol{y}} c_{\boldsymbol{x}s}^{\dagger} c_{\boldsymbol{y}s} + U \sum_{\boldsymbol{x}} \left(n_{\boldsymbol{x}\uparrow} - \frac{1}{2}\right)\left(n_{\boldsymbol{x}\downarrow} - \frac{1}{2}\right) - \mu \sum_{\boldsymbol{x}} \sum_{s} n_{\boldsymbol{x}s}$$

is obtained as a new form of the Hamiltonian of the Hubbard model. The above expression is also familiar as the Hamiltonian of the Hubbard model.

[3]Note that

$$\sum_{\boldsymbol{x}} \exp\left[\sum_{i=1}^{d} \frac{2\pi \mathrm{i}(k_i - k_i') x_i}{N_i}\right] = |\Lambda_d| \delta(\boldsymbol{k} - \boldsymbol{k}').$$

and

$$\ln Z = 2 \sum_{\boldsymbol{k}} \ln \left(1 + \mathrm{e}^{-\beta(\varepsilon_{\boldsymbol{k}} - \mu)} \right). \tag{6.24}$$

One can obtain the number density N as

$$N = \frac{\partial}{\partial \mu} \left(\frac{1}{\beta} \ln Z \right) = 2 \sum_{\boldsymbol{k}} \frac{1}{1 + \mathrm{e}^{\beta(\varepsilon_{\boldsymbol{k}} - \mu)}}. \tag{6.25}$$

6.4   Path-integral formulation on a $(d+1)$-dimensional lattice

The grand partition function Z in d dimensions is defined by $Z = \mathrm{Tr}(\mathrm{e}^{-\beta \hat{H}})$, which can be expressed by the path integral in $(d+1)$ dimensions over the Grassmann fields, following Ref. [BBW04]. Also see Ref. [Cre87] or Refs. [Tro59, Suz76] for the procedure to convert the operator formalism into the path-integral formalism. Setting the two-component Grassmann fields on $(\boldsymbol{x}, \tau) \in \Lambda_d \times \mathbb{R}$ as

$$\psi(\boldsymbol{x}, \tau) = \left(\begin{array}{c} \psi_\uparrow(\boldsymbol{x}, \tau) \\ \psi_\downarrow(\boldsymbol{x}, \tau) \end{array} \right), \tag{6.26}$$

$$\bar{\psi}(\boldsymbol{x}, \tau) = \left(\bar{\psi}_\uparrow(\boldsymbol{x}, \tau), \bar{\psi}_\downarrow(\boldsymbol{x}, \tau) \right), \tag{6.27}$$

one finds the path-integral representation for the grand partition function generated by Eq. (6.1) as

$$Z = \left(\prod_{n \in \Lambda_d \times \mathbb{R}} \int \int \mathrm{d}\bar{\psi}(\boldsymbol{x}, \tau) \mathrm{d}\psi(\boldsymbol{x}, \tau) \right) \exp \left[-\int_0^\beta \mathrm{d}\tau \left\{ \sum_{\boldsymbol{x} \in \Lambda_d} \bar{\psi}(\boldsymbol{x}, \tau) \frac{\partial}{\partial \tau} \psi(\boldsymbol{x}, \tau) \right. \right.$$
$$\left. \left. + \sum_{\boldsymbol{x}, \boldsymbol{y} \in \Lambda_d} t_{\boldsymbol{x}, \boldsymbol{y}} \bar{\psi}(\boldsymbol{x}, \tau) \psi(\boldsymbol{y}, \tau) + \frac{U}{2} \sum_{\boldsymbol{x} \in \Lambda_d} (\bar{\psi}(\boldsymbol{x}, \tau) \psi(\boldsymbol{x}, \tau))^2 - \mu \sum_{\boldsymbol{x} \in \Lambda_d} \bar{\psi}(\boldsymbol{x}, \tau) \psi(\boldsymbol{x}, \tau) \right\} \right]. \tag{6.28}$$

Now, we approximate the path integral Z via the discretization of the temporal direction by the equal time slice ϵ, with $\beta = N_\tau \epsilon$. This discretization introduces,

$$\int_0^\beta \mathrm{d}\tau \cdots \rightarrow \epsilon \sum_{n_\tau = 0}^{N_\tau - 1} \cdots, \tag{6.29}$$

$$\frac{\partial}{\partial \tau} \psi(\boldsymbol{x}, \tau) \rightarrow \frac{\psi(\boldsymbol{x}, n_\tau + \epsilon) - \psi(\boldsymbol{x}, n_\tau)}{\epsilon}. \tag{6.30}$$

Note that a forward difference in Eq. (6.30) is necessary because we are considering non-relativistic fermions, which have no anti-particle. In other words, all particles must be going forward with respect to the temporal direction. Hereafter, we set $n = (\boldsymbol{x}, n_\tau) = ((n_\sigma)_{\sigma=1,\cdots,d}, n_\tau) \in \Lambda_{d+1}$, which denotes the $(d+1)$-dimensional anisotropic lattice. Then, the "action" of the model is now given by

$$S = \sum_{n \in \Lambda_{d+1}} \epsilon \left\{ \bar{\psi}(n) \left(\frac{\psi(n + \hat{\tau}) - \psi(n)}{\epsilon} \right) - t \sum_{\sigma=1}^d \left(\bar{\psi}(n + \hat{\sigma}) \psi(n) + \bar{\psi}(n) \psi(n + \hat{\sigma}) \right) \right.$$
$$\left. + \frac{U}{2} \left(\bar{\psi}(n) \psi(n) \right)^2 - \mu \bar{\psi}(n) \psi(n) \right\}, \tag{6.31}$$

where $\hat{\sigma}$ denotes spatial unit vectors and $\hat{\tau}$ does the temporal one. Note that the half-filling is realized at $\mu = U/2$ in the current definition. We assume the periodic boundary condition for the spacial directions and the anti-periodic one for the temporal direction.

6.5   Tensor network representation

Since the hopping terms in Eq. (6.31) are all diagonal in the internal space, these are immediately decomposed as

$$e^{t\epsilon\bar{\psi}(n)\psi(n+\hat{\sigma})}$$

$$= \prod_{s=\uparrow,\downarrow} \int\int d\bar{\eta}_{\sigma,s}(n)d\eta_{\sigma,s}(n)\ e^{-\bar{\eta}_{\sigma,s}(n)\eta_{\sigma,s}(n)} \exp\left[\sqrt{t\epsilon}\bar{\psi}_s(n)\eta_{\sigma,s}(n) + \sqrt{t\epsilon}\bar{\eta}_{\sigma,s}(n)\psi_s(n+\hat{\sigma})\right], \quad (6.32)$$

$$e^{t\epsilon\bar{\psi}(n+\hat{\sigma})\psi(n)}$$

$$= \prod_{s=\uparrow,\downarrow} \int\int d\bar{\zeta}_{\sigma,s}(n)d\zeta_{\sigma,s}(n)\ e^{-\bar{\zeta}_{\sigma,s}(n)\zeta_{\sigma,s}(n)} \exp\left[-\sqrt{t\epsilon}\bar{\psi}_s(n+\hat{\sigma})\bar{\zeta}_{\sigma,s}(n) + \sqrt{t\epsilon}\zeta_{\sigma,s}(n)\psi_s(n)\right], \quad (6.33)$$

$$e^{-\bar{\psi}(n)\psi(n+\hat{\tau})}$$

$$= \prod_{s=\uparrow,\downarrow} \int\int d\bar{\eta}_{\tau,s}(n)d\eta_{\tau,s}(n)\ e^{-\bar{\eta}_{\tau,s}(n)\eta_{\tau,s}(n)} \exp\left[-\bar{\psi}_s(n)\eta_{\tau,s}(n) + \bar{\eta}_{\tau,s}(n)\psi_s(n+\hat{\tau})\right]. \quad (6.34)$$

One is now allowed to integrate out ψ and $\bar{\psi}$ at the each site $n \in \Lambda_{d+1}$ independently. The Grassmann tensor is then defined as a result of the integration,

$$\mathcal{T}_{\Psi_1(n)\cdots\Psi_d(n)\Psi_\tau(n)\bar{\Psi}_\tau(n-\hat{\tau})\bar{\Psi}_d(n-\hat{d})\cdots\bar{\Psi}_1(n-\hat{1})}$$

$$= \left(\prod_{s=\uparrow,\downarrow} \int\int d\bar{\psi}_s d\psi_s\right)\ e^{-U\epsilon\bar{\psi}_\uparrow\psi_\uparrow\bar{\psi}_\downarrow\psi_\downarrow+(\mu\epsilon+1)\bar{\psi}_\uparrow\psi_\uparrow+(\mu\epsilon+1)\bar{\psi}_\downarrow\psi_\downarrow}$$

$$\times\ \exp\left[\sum_{\sigma=1}^{d}\sum_{s=\uparrow,\downarrow}\left\{-\sqrt{t\epsilon}\bar{\psi}_s\bar{\zeta}_{\sigma,s}(n-\hat{\sigma}) + \sqrt{t\epsilon}\zeta_{\sigma,s}(n)\psi_s\right\}\right]$$

$$\times\ \exp\left[\sum_{\sigma=1}^{d}\sum_{s=\uparrow,\downarrow}\left\{\sqrt{t\epsilon}\bar{\psi}_s\eta_{\sigma,s}(n) + \sqrt{t\epsilon}\bar{\eta}_{\sigma,s}(n-\hat{\sigma})\psi_s\right\}\right]$$

$$\times\ \exp\left[\sum_{s=\uparrow,\downarrow}\left\{-\bar{\psi}_s\eta_{\tau,s}(n) + \bar{\eta}_{\tau,s}(n-\hat{\tau})\psi_s\right\}\right], \quad (6.35)$$

with $\Psi_\sigma = (\eta_{\sigma,\uparrow}, \eta_{\sigma,\downarrow}, \zeta_{\sigma,\uparrow}, \zeta_{\sigma,\downarrow})$, $\bar{\Psi}_\sigma = (\bar{\eta}_{\sigma,\uparrow}, \bar{\eta}_{\sigma,\downarrow}, \bar{\zeta}_{\sigma,\uparrow}, \bar{\zeta}_{\sigma,\downarrow})$, $\Psi_\tau = (\eta_{\tau,\uparrow}, \eta_{\tau,\downarrow})$, and $\bar{\Psi}_\tau = (\bar{\eta}_{\tau,\uparrow}, \bar{\eta}_{\tau,\downarrow})$. Using this Grassmann tensor $\mathcal{T}$, one obtains the tensor network representation for the path integral Z of the $(d+1)$-dimensional Hubbard model as

$$Z = \left(\prod_{n\in\Lambda_{d+1}} \int\int d\bar{\Psi}_\tau(n)d\Psi_\tau(n)\ e^{-\bar{\Psi}_\tau(n)\Psi_\tau(n)} \prod_{\sigma=1}^{d} \int\int d\bar{\Psi}_\sigma(n)d\Psi_\sigma(n)\ e^{-\bar{\Psi}_\sigma(n)\Psi_\sigma(n)}\right)$$

$$\times \prod_{n\in\Lambda_{d+1}} \mathcal{T}_{\Psi_1(n)\cdots\Psi_d(n)\Psi_\tau(n)\bar{\Psi}_\tau(n-\hat{\tau})\bar{\Psi}_d(n-\hat{d})\cdots\bar{\Psi}_1(n-\hat{1})}. \quad (6.36)$$

56

Since this form is nothing but the Grassmann tensor network as shown in Eq. (2.80), we also write Eq. (6.36) as

$$Z = \text{gTr} \left[\prod_{n \in \Lambda_{d+1}} \mathcal{T}_{\Psi_1(n) \cdots \Psi_d(n) \Psi_\tau(n) \bar{\Psi}_\tau(n-\hat{\tau}) \bar{\Psi}_d(n-\hat{d}) \cdots \bar{\Psi}_1(n-\hat{1})} \right]. \tag{6.37}$$

Let us explicitly carry out the integration over ψ and $\bar{\psi}$ in Eq. (6.35). One finds the expression,

$$
\begin{aligned}
&\mathcal{T}_{\Psi_1 \cdots \Psi_d \Psi_\tau \bar{\Psi}_\tau \bar{\Psi}_d \cdots \bar{\Psi}_1} \\
&= \left(\prod_{\sigma=1}^{d} \sum_{i_{\sigma,\uparrow}, i_{\sigma,\downarrow}, j_{\sigma,\uparrow}, j_{\sigma,\downarrow}} \right) \sum_{i_{\tau,\uparrow}, i_{\tau,\downarrow}} \left(\prod_{\sigma=1}^{d} \sum_{i'_{\sigma,\uparrow}, i'_{\sigma,\downarrow}, j'_{\sigma,\uparrow}, j'_{\sigma,\downarrow}} \right) \sum_{i'_{\tau,\uparrow}, i'_{\tau,\downarrow}} \\
&\times (-1)^{\sum_{\sigma,s} i_{\sigma,s}} (\sqrt{t\epsilon})^{\sum_{\sigma,s}(i_{\sigma,s}+j_{\sigma,s}+i'_{\sigma,s}+j'_{\sigma,s})} \\
&\times \Big[\delta_{1, i_{\tau,\downarrow} + \sum_\sigma (i_{\sigma,\downarrow}+j'_{\sigma,\downarrow})} \delta_{1, i'_{\tau,\downarrow} + \sum_\sigma (i'_{\sigma,\downarrow}+j_{\sigma,\downarrow})} \delta_{1, i_{\tau,\uparrow} + \sum_\sigma (i_{\sigma,\uparrow}+j'_{\sigma,\uparrow})} \delta_{1, i'_{\tau,\uparrow} + \sum_\sigma (i'_{\sigma,\uparrow}+j_{\sigma,\uparrow})} \\
&\quad - (\mu\epsilon+1) \delta_{0, i_{\tau,\downarrow} + \sum_\sigma (i_{\sigma,\downarrow}+j'_{\sigma,\downarrow})} \delta_{0, i'_{\tau,\downarrow} + \sum_\sigma (i'_{\sigma,\downarrow}+j_{\sigma,\downarrow})} \delta_{1, i_{\tau,\uparrow} + \sum_\sigma (i_{\sigma,\uparrow}+j'_{\sigma,\uparrow})} \delta_{1, i'_{\tau,\uparrow} + \sum_\sigma (i'_{\sigma,\uparrow}+j_{\sigma,\uparrow})} \\
&\quad - (\mu\epsilon+1) \delta_{1, i_{\tau,\downarrow} + \sum_\sigma (i_{\sigma,\downarrow}+j'_{\sigma,\downarrow})} \delta_{1, i'_{\tau,\downarrow} + \sum_\sigma (i'_{\sigma,\downarrow}+j_{\sigma,\downarrow})} \delta_{0, i_{\tau,\uparrow} + \sum_\sigma (i_{\sigma,\uparrow}+j'_{\sigma,\uparrow})} \delta_{0, i'_{\tau,\uparrow} + \sum_\sigma (i'_{\sigma,\uparrow}+j_{\sigma,\uparrow})} \\
&\quad - \left\{ U\epsilon - (\mu\epsilon+1)^2 \right\} \delta_{0, i_{\tau,\downarrow} + \sum_\sigma (i_{\sigma,\downarrow}+j'_{\sigma,\downarrow})} \delta_{0, i'_{\tau,\downarrow} + \sum_\sigma (i'_{\sigma,\downarrow}+j_{\sigma,\downarrow})} \delta_{0, i_{\tau,\uparrow} + \sum_\sigma (i_{\sigma,\uparrow}+j'_{\sigma,\uparrow})} \delta_{0, i'_{\tau,\uparrow} + \sum_\sigma (i'_{\sigma,\uparrow}+j_{\sigma,\uparrow})} \Big] \\
&\times \eta_{\tau,\uparrow}^{i_{\tau,\uparrow}} \left(\prod_\sigma \eta_{\sigma,\uparrow}^{i_{\sigma,\uparrow}} \bar{\zeta}_{\sigma,\uparrow}^{j_{\sigma,\uparrow}} \right) \bar{\eta}_{\tau,\uparrow}^{i'_{\tau,\uparrow}} \left(\prod_\sigma \bar{\eta}_{\sigma,\uparrow}^{i'_{\sigma,\uparrow}} \zeta_{\sigma,\uparrow}^{j_{\sigma,\uparrow}} \right) \eta_{\tau,\downarrow}^{i_{\tau,\downarrow}} \left(\prod_\sigma \eta_{\sigma,\downarrow}^{i_{\sigma,\downarrow}} \bar{\zeta}_{\sigma,\downarrow}^{j_{\sigma,\downarrow}} \right) \bar{\eta}_{\tau,\downarrow}^{i'_{\tau,\downarrow}} \left(\prod_\sigma \bar{\eta}_{\sigma,\downarrow}^{i'_{\sigma,\downarrow}} \zeta_{\sigma,\downarrow}^{j_{\sigma,\downarrow}} \right),
\end{aligned} \tag{6.38}
$$

where we have assigned the subscripts $i_{\sigma,s}(n)$, $j_{\sigma,s}(n)$, and $i_{\tau,s}(n)$ to label those in the Taylor expansion for Eq. (6.32), Eq. (6.33), and Eq. (6.34), respectively. They take just 0 or 1 because of the nilpotency of the Grassmann variables. We sort the auxiliary Grassmann fields in Eq. (6.38) as those in Eq. (6.39) and the Grassmann tensor $\mathcal{T}$ is finally written as

$$
\begin{aligned}
&\mathcal{T}_{\Psi_1 \cdots \Psi_d \Psi_\tau \bar{\Psi}_\tau \bar{\Psi}_d \cdots \bar{\Psi}_1} \\
&= \left(\prod_{\sigma=1}^{d} \sum_{i_{\sigma,\uparrow}, i_{\sigma,\downarrow}, j_{\sigma,\uparrow}, j_{\sigma,\downarrow}} \right) \sum_{i_{\tau,\uparrow}, i_{\tau,\downarrow}} \left(\prod_{\sigma=1}^{d} \sum_{i'_{\sigma,\uparrow}, i'_{\sigma,\downarrow}, j'_{\sigma,\uparrow}, j'_{\sigma,\downarrow}} \right) \sum_{i'_{\tau,\uparrow}, i'_{\tau,\downarrow}} \\
&\times T_{(i_{1,\uparrow}, i_{1,\downarrow}, j_{1,\uparrow}, j_{1,\downarrow}) \cdots (i_{d,\uparrow}, i_{d,\downarrow}, j_{d,\uparrow}, j_{d,\downarrow})(i_{\tau,\uparrow}, i_{\tau,\downarrow})(i'_{1,\uparrow}, i'_{1,\downarrow}, j'_{1,\uparrow}, j'_{1,\downarrow}) \cdots (i'_{d,\uparrow}, i'_{d,\downarrow}, j'_{d,\uparrow}, j'_{d,\downarrow})(i'_{\tau,\uparrow}, i'_{\tau,\downarrow})} \\
&\times \left(\eta_{1,\uparrow}^{i_{1,\uparrow}} \eta_{1,\downarrow}^{i_{1,\downarrow}} \zeta_{1,\uparrow}^{j_{1,\uparrow}} \zeta_{1,\downarrow}^{j_{1,\downarrow}} \right) \cdots \left(\eta_{d,\uparrow}^{i_{d,\uparrow}} \eta_{d,\downarrow}^{i_{d,\downarrow}} \zeta_{d,\uparrow}^{j_{d,\uparrow}} \zeta_{d,\downarrow}^{j_{d,\downarrow}} \right) \left(\eta_{\tau,\uparrow}^{i_{\tau,\uparrow}} \eta_{\tau,\downarrow}^{i_{\tau,\downarrow}} \right) \\
&\times \left(\bar{\eta}_{\tau,\downarrow}^{i'_{\tau,\downarrow}} \bar{\eta}_{\tau,\uparrow}^{i'_{\tau,\uparrow}} \right) \left(\bar{\zeta}_{d,\downarrow}^{j'_{d,\downarrow}} \bar{\zeta}_{d,\uparrow}^{j'_{d,\uparrow}} \bar{\eta}_{d,\downarrow}^{i'_{d,\downarrow}} \bar{\eta}_{d,\uparrow}^{i'_{d,\uparrow}} \right) \cdots \left(\bar{\zeta}_{1,\downarrow}^{j'_{1,\downarrow}} \bar{\zeta}_{1,\uparrow}^{j'_{1,\uparrow}} \bar{\eta}_{1,\downarrow}^{i'_{1,\downarrow}} \bar{\eta}_{1,\uparrow}^{i'_{1,\uparrow}} \right).
\end{aligned} \tag{6.39}
$$

In the above expression, the coefficients of the auxiliary Grassmann fields are identified as a multi-rank tensor T. As we explained previously, when one applies the TRG approach to evaluate the path integral over the Grassmann fields, it is practically useful to encode the Grassmann parity of the auxiliary Grassmann fields into the subscripts of the coefficient tensor. We identify the coefficient tensor in Eq. (6.39) as a $2(d+1)$-rank tensor $T_{I_1 \cdots I_d I_\tau I'_1 \cdots I'_d I'_\tau}$, where $I_\sigma^{(')} = 1, \cdots, 2^4$ and $I_\tau^{(')} = 1, \cdots, 2^2$. We define $I_\sigma^{(')}$ and $I_\tau^{(')}$ as in Tables 6.1 and 6.2. Notice that $I_\sigma^{(')} = 1, \cdots, 8$ correspond to the Grassmann-even sector and $I_\sigma^{(')} = 9, \cdots, 16$ to the Grassmann-odd one in Ψ_σ ($\bar{\Psi}_\sigma$). Similarly, $I_\tau^{(')} = 1, 2$ correspond to the Grassmann-even sector and $I_\tau^{(')} = 3, 4$ to the Grassmann-odd one in Ψ_τ ($\bar{\Psi}_\tau$).

Table 6.1: Mapping of spatial subscripts.

$I_\sigma^{(\prime)}$	1	2	3	4	5	6	7	8	9	10	11	12	13	14	15	16
$i_{\sigma,\uparrow}^{(\prime)}$	0	1	1	1	0	0	0	1	1	0	0	1	0	1	1	0
$i_{\sigma,\downarrow}^{(\prime)}$	0	1	0	0	1	1	0	1	0	1	0	1	0	1	0	1
$j_{\sigma,\uparrow}^{(\prime)}$	0	0	1	0	1	0	1	1	0	0	1	1	0	0	1	1
$j_{\sigma,\downarrow}^{(\prime)}$	0	0	0	1	0	1	1	1	0	0	0	0	1	1	1	1

Table 6.2: Mapping of temporal subscripts.

$I_\tau^{(\prime)}$	1	2	3	4
$i_{\tau,\uparrow}^{(\prime)}$	0	1	1	0
$i_{\tau,\downarrow}^{(\prime)}$	0	1	0	1

6.6   The model in $(1+1)$ dimensions

Since the one-dimensional Hubbard model is exactly solved by the Bethe ansatz [LW68, LW03], we begin with investigating the model in $(1+1)$ dimensions. This study serves as a testbed whether the TRG method works efficiently for the Hubbard model. The Grassmann tensor network representation is

$$Z = \mathrm{gTr}\left[\prod_{n\in\Lambda_{1+1}} \mathcal{T}_{\Psi_\sigma(n)\Psi_\tau(n)\bar\Psi_\tau(n-\hat\tau)\bar\Psi_\sigma(n-\hat\sigma)}\right], \tag{6.40}$$

where $\mathcal{T}$ is obtained by Eq. (6.39) with $d = 1$. The following numerical study is based on Ref. [AK21b].

6.6.1   Numerical strategy

We employ the HOTRG algorithm to evaluate the Grassmann tensor network generated by Eq. (6.40). Using the HOTRG, we firstly carry out $m_\tau(\in \mathbb{N})$ times of renormalization-group transformation just along the temporal direction. This procedure, corresponding to the imaginary-time evolution, converts the initial Grassmann tensor $\mathcal{T}_{\Psi_\sigma\Psi_\tau\bar\Psi_\tau\bar\Psi_\sigma}$ into the coarse-grained one $\mathcal{T}_{\Xi_\sigma\Psi_\tau\bar\Psi_\tau\bar\Xi_\sigma}$. The initial Grassmann tensor $\mathcal{T}_{\Psi_\sigma\Psi_\tau\bar\Psi_\tau\bar\Psi_\sigma}$ corresponds to a system at inverse temperature $\beta = \epsilon$ and $\mathcal{T}_{\Xi_\sigma\Psi_\tau\bar\Psi_\tau\bar\Xi_\sigma}$ does to one at $\beta = 2^{m_\tau}\epsilon$. Secondly, we employ the HOTRG to carry out $2m(\in \mathbb{N})$ times of spacetime coarse-graining, regarding $\mathcal{T}_{\Xi_\sigma\Psi_\tau\bar\Psi_\tau\bar\Xi_\sigma}$ as the initial tensor. As a result, the path integral is evaluated on the lattice whose physical volume is given by $V = N_\sigma \times (\epsilon N_\tau)$ with $(N_\sigma, N_\tau) = (2^m, 2^{m+m_\tau})$. With sufficiently small $\epsilon(< 1)$, little truncation error is accumulated with the first m_τ times of renormalization along τ-direction. This is because the contribution from the spatial hopping terms, which are of $\mathcal{O}(\epsilon)$, is smaller than that from the temporal one, which is of $\mathcal{O}(1)$. In other words, spatially adjacent Grassmann tensors in Eq. (6.40) are almost free and the approximation based on the SVD is not efficient. On the other hand, temporally adjacent tensors in Eq. (6.40) have strongly interacted and it works very well. [4] For the $(1+1)$-dimensional Hubbard model, we found that the optimal m_τ

---

[4]A similar remark is also mentioned in Ref. [XCQ$^+$12], where the three-dimensional HOTRG is applied to the two-dimensional quantum transverse Ising model in the path-integral formalism.

satisfied the condition $\epsilon 2^{m_\tau} \sim \mathcal{O}(10^{-1})$. Note that optimal m_τ does depend on ϵ.

6.6.2   Comparison with exact solutions

Firstly, we consider the one-site model explained previously. We numerically evaluate the number density as a function of μ via

$$\langle n \rangle = \frac{1}{V} \frac{\partial \ln Z}{\partial \mu} \approx \frac{1}{V} \frac{\ln Z(\mu + \Delta\mu) - \ln Z(\mu - \Delta\mu)}{2\Delta\mu}. \tag{6.41}$$

The thermodynamic potential is evaluated by the TRG approach. The exact result of $\langle n \rangle$ has been already obtained in Eq. (6.14). Setting $(U, t) = (4, 0)$, we obtain the result shown in Fig. 6.1. Since the one-site model describes a spatially decoupled electron, we set $m = 0$ and all we have to do is m_τ times of imaginary-time evolution. Thanks to the vanishing hopping structure in the spatial direction, we can always carry out contractions between Grassmann tensors without the decimation based on the SVD. In Fig. 6.1, we set $\epsilon = 10^{-4}$ and $m_\tau = 24$. As you can see, the TRG calculation restores the exact result. In addition, the one-site model exhibits the Mott insulating phase, which is characterized by the plateau of $\langle n \rangle = 1$.
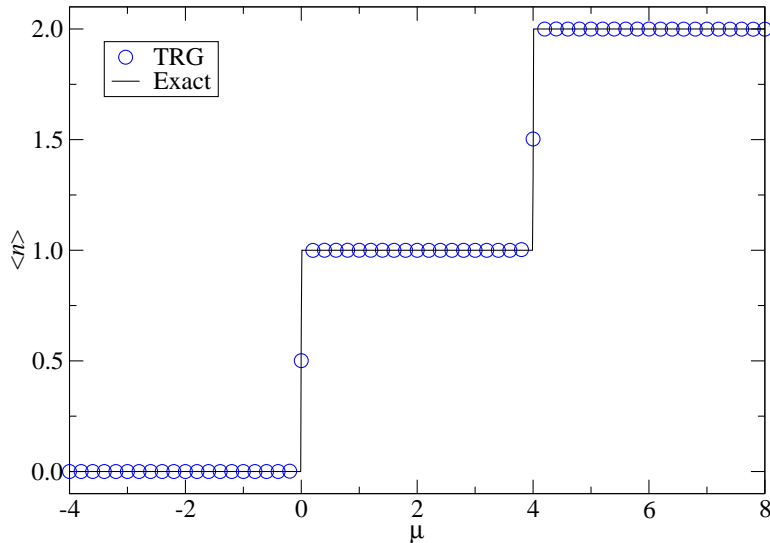
Figure 6.1: Electron density $\langle n \rangle$ in the $(U, t) = (4, 0)$ case at $\beta = 1677.7216$ with $\epsilon = 10^{-4}$ as a function of μ. The solid line shows the exact solution and the blue circles are the results obtained by the TRG approach.

Secondly, we investigate the free-electron model, which is given by setting $U = 0$. The number density is easily obtained as in Eq. (6.25). Setting $t = 1$, $\epsilon = 10^{-4}$, and $m_\tau = m = 12$, we obtain Figure 6.2. The TRG results is again derived by Eq. (6.41) and the finer resolution $\Delta\mu$ is employed around $1 \lesssim |\mu| \lesssim 2$. Fig. 6.2 shows that the imaginary-time evolution followed by the two-dimensional coarse-graining works well. Of course, there is no Mott insulating phase in the free-field theory.

We now move on to the case where U/t takes a finite value. This is a physically interesting situation, because electrons do become itinerant. Here, we consider $(U, t) = (4, 1)$. In Fig. 6.3, we
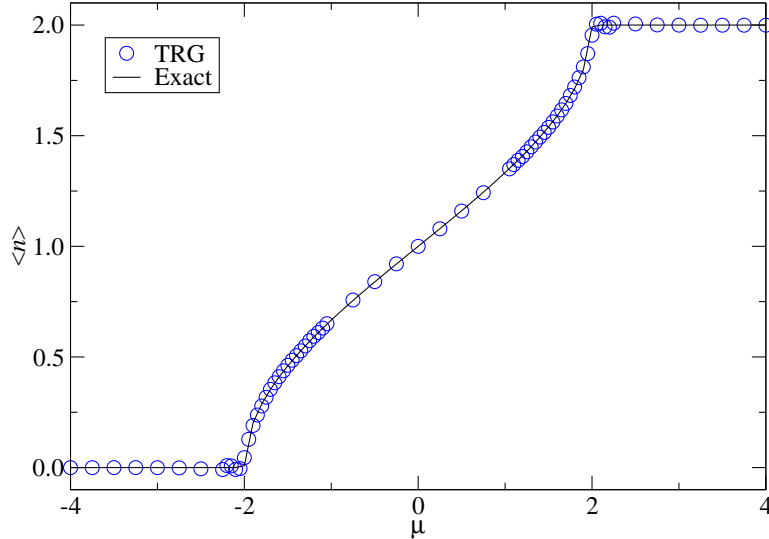
Figure 6.2: Electron density $\langle n \rangle$ in the $(U, t) = (0, 1)$ case at $N_\sigma = 4096$ and $\beta = 1677.7216$ with $\epsilon = 10^{-4}$ as a function of μ. The solid line shows the exact solution on $N_\sigma = 4096$ and the blue circles are the results obtained by the TRG approach with $D = 80$.

plot the thermodynamic potential $\ln Z / V$, as a function of μ, on $V = 4096 \times 1677.7216$ with the bond dimension $D = 80$, choosing $\epsilon = 2^{12} \times 10^{-4}, 2^8 \times 10^{-4}, 2^4 \times 10^{-4}, 10^{-4}$. For each ϵ, m_τ is decided via the condition $\epsilon 2^{m_\tau} = 2^{12} \times 10^{-4} = \mathcal{O}(10^{-1})$. With $\epsilon = 2^{12} \times 10^{-4}$, there is a clear discretization error. On the other hand, the results with $\epsilon = 2^4 \times 10^{-4}$ and 10^{-4} show good consistency, which means that the discretization effect with $\epsilon = 10^{-4}$ is negligible and we are allowed to regard Λ_{1+1} as $\Lambda_1 \times \mathbb{R}$. Next, we investigate the convergence behavior of the thermodynamic potential via the relative error defined by

$$\delta_D = \left| \frac{\ln Z(D) - \ln Z(D = 80)}{\ln Z(D = 80)} \right| \tag{6.42}$$

on $V = 4096 \times 1677.7216$ lattice with $\epsilon = 10^{-4}$. In Fig. 6.4, we plot the D dependence of δ_D at $\mu = 2.75$ and 2.00, which are near and far away from the critical point μ_c, respectively, as we will see below. We observe that δ_D decreases as a function of D and reaches $\mathcal{O}(10^{-4})$ at $D = 75$ for both values of μ.

Having confirmed the converging behaviors both for ϵ and D, we evaluate the number density via Eq. (6.41). Figure 6.5 shows the physical volume dependence of $\langle n \rangle$ with $\epsilon = 10^{-4}$ and $m_\tau = 12$. The results indicate that the size $(N_\sigma, N_\tau) = (2^{12}, 2^{24})$, which corresponds to $V = 4096 \times 1677.7216$, is sufficiently large to be identified as the thermodynamic and zero-temperature limit. We can see a clear signal of the Mott insulating phase, which is characterized by the plateau with $\langle n \rangle = 1$ over the range of $1.3 \lesssim \mu \lesssim 2.7$. We also observe that the number density continuously changes from $\langle n \rangle = 1$ to $\langle n \rangle = 2$ over the range of $2.7 \lesssim \mu \lesssim 6.5$. Figure 6.6 also shows $\langle n \rangle$ as a function of μ, but in the vicinity of criticality on $V = 4096 \times 1677.7216$. The abrupt change of $\langle n \rangle$ at $\mu \approx 2.70$ in Fig. 6.6 indicates the metal-insulator transition. Note that this transition is not observed in the free-field case
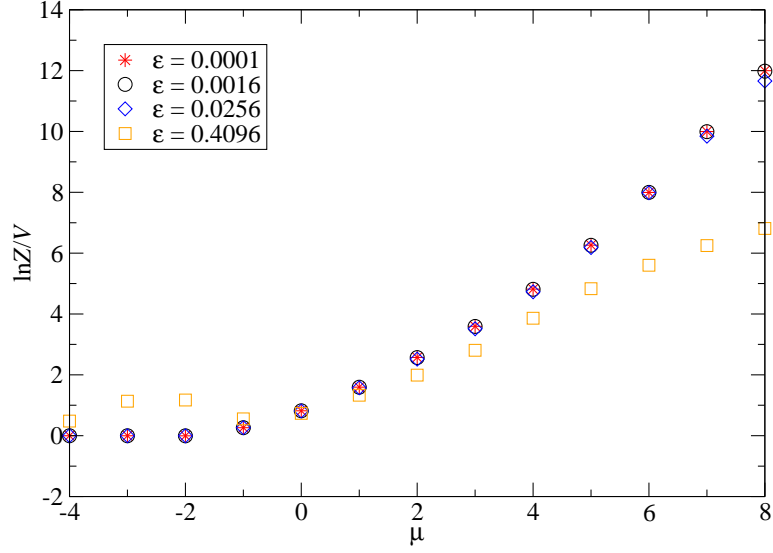
Figure 6.3: Thermodynamic potential at $U/t = 4$ on $V = 4096 \times 1677.7216$ lattice as a function of chemical potential μ. β is divided with $\epsilon = 2^{12} \times 10^{-4}, 2^8 \times 10^{-4}, 2^4 \times 10^{-4}$, and 10^{-4}. The bond dimension is chosen to be $D = 80$.
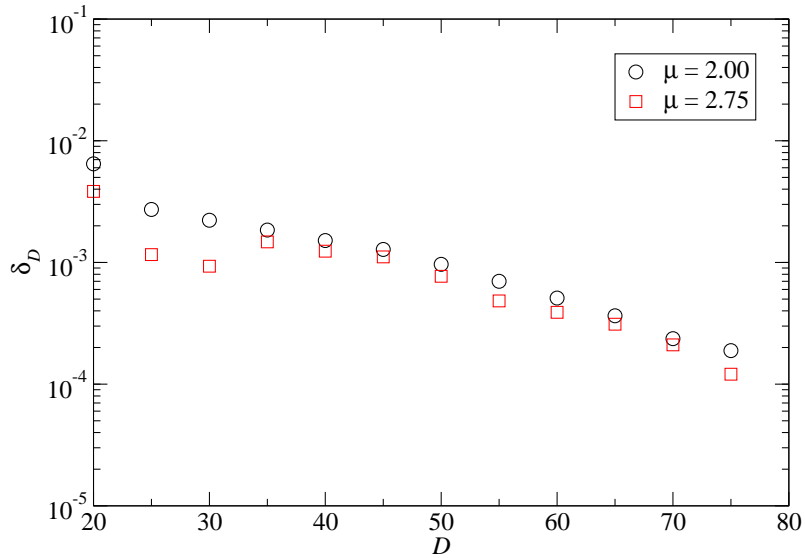
Figure 6.4: Convergence behavior of thermodynamic potential with δ of Eq. (6.42) at $\mu = 2.00$ and 2.75 as a function of D on $V = 4096 \times 1677.7216$ lattice.

as shown in Fig. 6.2.
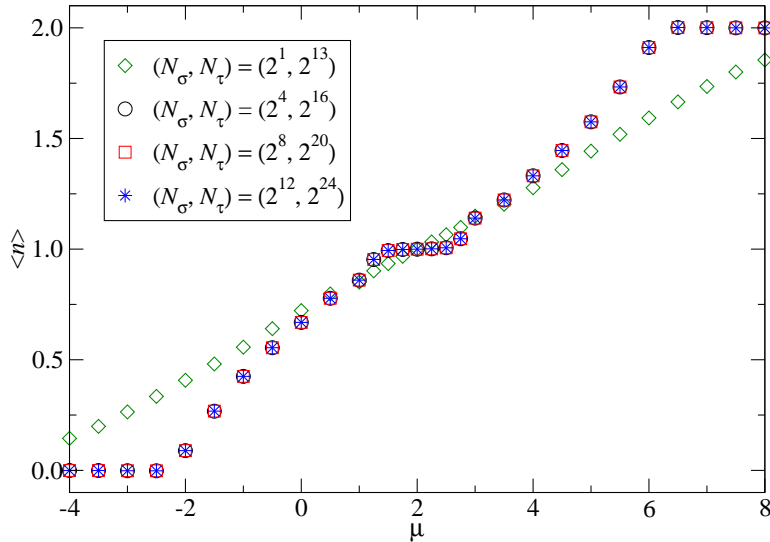
Figure 6.5: Electron density $\langle n \rangle$ at several lattice sizes with $\epsilon = 10^{-4}$ as a function of μ. The bond dimension is chosen to be $D = 80$.

We determine the critical chemical potential $\mu_c(D)$ and the critical exponent ν on $V = 4096 \times 1677.7216$ lattice by fitting $\langle n \rangle$ in the metallic phase around the criticality with the fitting ansatz,

$$\langle n \rangle = A + B \left| \mu - \mu_c(D) \right|^\nu, \tag{6.43}$$

where A, B, $\mu_c(D)$, and ν are the fit parameters. The solid curve in Fig. 6.6 shows the fitting result over the range of $2.68 \leq \mu \leq 3.00$. We obtain $\mu_c(D) = 2.698(1)$ and $\nu = 0.51(2)$ at $D = 80$. Our result for the critical exponent is consistent with the theoretical prediction of $\nu = 1/2$. A previous Quantum MC simulation with small spatial extension up to $L = 24$ also yielded the same conclusion [AI96]. To

Table 6.3: Critical chemical potential $\mu_c(D)$ and critical exponent ν at each D.

D	60	65	70	75	80	∞
fit range	[2.72,3.00]	[2.70,3.00]	[2.70,3.00]	[2.69,3.00]	[2.68,3.00]	–
$\mu_c(D)$	2.720(3)	2.710(1)	2.7068(8)	2.701(1)	2.698(1)	2.642(05)(13)
ν	0.49(3)	0.52(1)	0.50(2)	0.51(2)	0.51(2)	–

extrapolate the result of $\mu_c(D)$ to the limit $D \to \infty$, we repeat the calculation of $\langle n \rangle$, varying the bond dimension D and its fitting. The fitting results are summarized in Table 6.3. In Fig. 6.7, we plot $\mu_c(D)$ as a function of $1/D$, performing two types of fittings. The solid line shows the fitting result with the function $\mu_c(D) = \mu_c + aD^{-1}$, which results in $\mu_c = 2.642(5)$ and $a = 4.5(4)$ with $\chi^2/\text{d.o.f} = 0.447093$. We have also fitted the data with the function $\mu_c(D) = \mu_c + bD^{-c}$, shown as
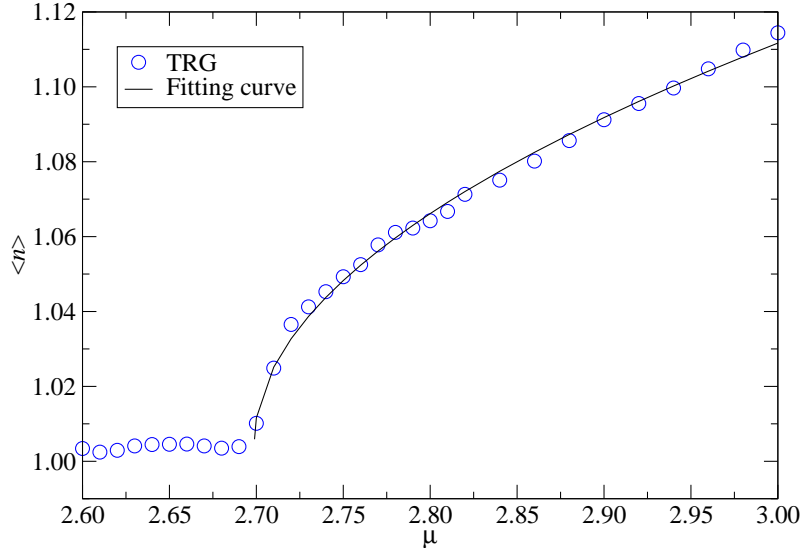
Figure 6.6: Electron density $\langle n \rangle$ at $\beta = 1677.7216$ with $\epsilon = 10^{-4}$ as a function of μ. The bond dimension is chosen to be $D = 80$.

the dotted curve in Fig. 6.7, to estimate an uncertainty in the choice of the fitting ansatz. We regard the difference between the central values of μ_c obtained by these two types of fittings as a systematic error. We obtain $\mu_c = 2.642(05)(13)$ as the value of $\lim_{D \to \infty} \mu_c(D)$, which shows good consistency with the exact solution of $\mu_c = 2.643 \cdots$ given by the Bethe ansatz [LW68,LW03].

6.7   The model in $(2+1)$ dimensions

No exact solution has been known for the two-dimensional Hubbard model. Although various numerical investigations have been performed, there is little consensus about its thermodynamic limit in low-temperature regimes among different numerical methods. [5] According to Ref. [Hir85], the MC simulation based on the Hubbard-Stratonovich transformation made a prediction that the two-dimensional system is always paramagnetic away from the half-filling state, which is in contradiction with the Hartree-Fock calculation, where the system can be antiferromagnetic, ferromagnetic, and paramagnetic, depending on the number density and the value of U/t. Moreover, a recent Quantum MC study in Ref. [PBH$^+$07] provides us with a scenario in which there can be an antiferromagnetic insulating phase for all U. This is in contrast with the prediction by the DMFT calculation, where no metal-insulator transition takes place with $U < U_c$ [GKKR96]. Several recent DMFT calculations suggest that there is a transition from band insulator to metal at a critical coupling $U_{c,1}$ and at $U_{c,2} > U_{c,1}$, there is a second transition from the metal to the Mott insulating phase [GKR06,SHT10].

Here, we would like to investigate the model with the TRG approach, which has not been applied to $(2+1)$-dimensional Hubbard model so far. Since we can access the thermodynamic limit directly within the TRG approach, the method can give us an insight into such a complicated status. The

---

[5]Various numerical methods are explained in Ref. [LAB$^+$15], where an assessment of the ability to compute the thermodynamic limit is provided via several calculations of the systems with a small number of sites.
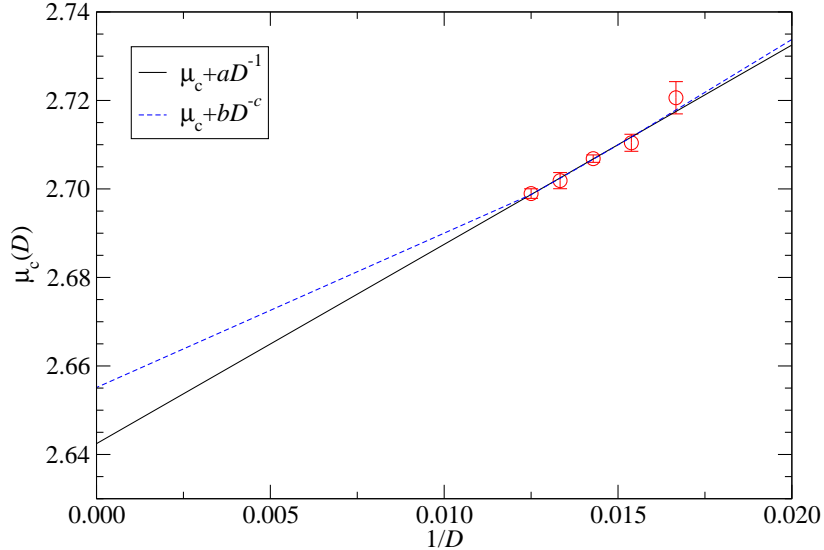
Figure 6.7: Critical chemical potential $\mu_c(D)$ as a function of $1/D$. Solid line represents the fitting result with the function $\mu_c(D) = \mu_c + aD^{-1}$. Dotted curve also shows the fitting result with the function $\mu_c(D) = \mu_c + bD^{-c}$.

applicability of the TRG to higher-dimensional lattice systems is another important property in this study. We can straightforwardly extend the previous numerical strategy in (1+1)-dimensional Hubbard model with a certain choice of the algorithm. The Grassmann tensor network representation of the path integral is of the form

$$Z = \text{gTr}\left[\prod_{n \in \Lambda_{2+1}} \mathcal{T}_{\Psi_x(n)\Psi_y(n)\Psi_\tau(n)\bar{\Psi}_\tau(n-\hat{\tau})\bar{\Psi}_y(n-\hat{y})\bar{\Psi}_x(n-\hat{x})}\right], \tag{6.44}$$

where the Grassmann tensor $\mathcal{T}$ is obtained by Eq. (6.39) with $d = 2$. The following numerical study is based on Ref. [AKY21a].

6.7.1   Numerical strategy

The initial Grassmann tensor $\mathcal{T}_{\Psi_x\Psi_y\Psi_\tau\bar{\Psi}_\tau\bar{\Psi}_y\bar{\Psi}_x}$ is of rank 6 and we evaluate Eq. (6.44) with the ATRG algorithm. We also follow the strategy employed in the previous study of $(1+1)d$ Hubbard model. Firstly, we carry out m_τ times of renormalization-group transformation along the temporal direction, which can be regarded as the imaginary-time evolution. Secondly, the three-dimensional ATRG procedure is applied as a sequential spacetime coarse-graining, which is iterated $3m$ ($m \in \mathbb{N}$) times. As in the case of $(1 + 1)d$ Hubbard model, we found that the optimal m_τ satisfies the condition $\epsilon 2^{m_\tau} \sim \mathcal{O}(10^{-1})$, checking the history of preserved tensor norm under the renormalization-group transformations. As a result of this ATRG calculation, the path integral on the lattice whose physical volume is $V = N_x \times N_y \times \epsilon N_\tau$ with $(N_x, N_y, N_\tau) = (2^m, 2^m, 2^{m+m_\tau})$ is obtained.

6.7.2   Algorithmic-parameter dependence

Let us begin with checking how the resulting value of Z is affected by algorithmic parameters. As in the study of $(1+1)d$ Hubbard model, we have two algorithmic parameters, the time slice ϵ and the bond dimension D. In Fig. 6.8, we plot the thermodynamic potential $\ln Z/V$ as a function of μ at $U = 8$ on $V = 4096^2 \times 1677.7216$ with $D = 80$, choosing $\epsilon = 2^{12} \times 10^{-4}, 2^8 \times 10^{-4}, 2^4 \times 10^{-4}, 10^{-4}$. For each ϵ, m_τ is chosen via the condition $\epsilon 2^{m_\tau} = 2^{12} \times 10^{-4} = \mathcal{O}(10^{-1})$. Convergence with respect to ϵ is almost similar to Fig. 6.3. Since the results with $\epsilon = 2^4 \times 10^{-4}$ and 10^{-4} show good consistency, hereafter we set $\epsilon = 10^{-4}$, which allows us to regard Λ_{2+1} as $\Lambda_2 \times \mathbb{R}$. We also investigate the finite-D
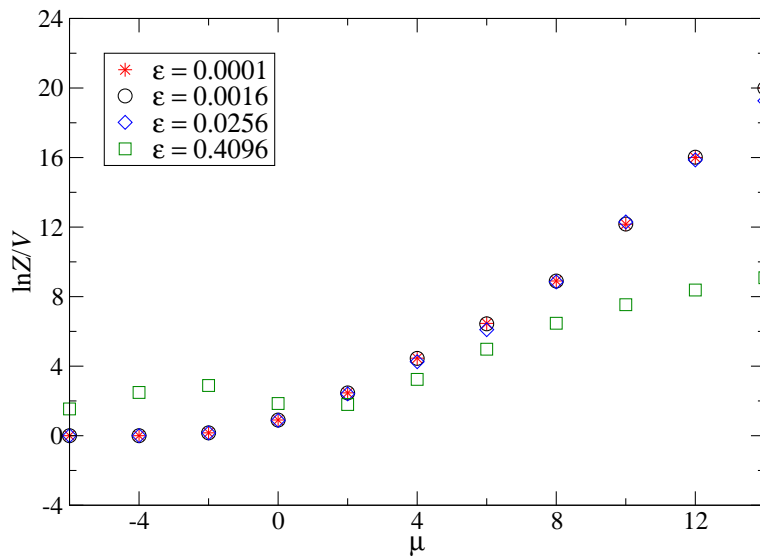
Figure 6.8: Thermodynamic potential at $U = 8$ on $V = 4096^2 \times 1677.7216$ lattice. β is divided with $\epsilon = 2^{12} \times 10^{-4} = 0.4096$, $2^8 \times 10^{-4} = 0.0256$, $2^4 \times 10^{-4} = 0.0016$ and $10^{-4} = 0.0001$. The bond dimension is set to be $D = 80$.

effect by defining the quantity

$$\delta_D = \left| \frac{\ln Z(D) - \ln Z(D = 80)}{\ln Z(D = 80)} \right| \tag{6.45}$$

on $V = 4096^2 \times 1677.7216$ lattice with $\epsilon = 10^{-4}$. In Fig. 6.9, we plot δ_D at $(U, t) = (8, 1)$ with the choices of $\mu = 6.0, 7.5$ and 8.5. As we will see below, $\mu = 6.0$ corresponds to $\langle n \rangle \approx 1.0$ and $\mu = 8.5$ does to $\langle n \rangle \approx 1.5$. We observe that δ_D's at these values of μ decrease as a function of D, though some of them are fluctuating.

6.7.3   Strong coupling regime

We firstly check the numerical strategy explained above via calculating the one-site model. Setting $(U, t) = (8, 0)$ and $m_\tau = 24$, we evaluate the number density $\langle n \rangle$ based on Eq. (6.41). In Fig. 6.10, we plot the resulting $\langle n \rangle$ as a function of μ. The validity of the imaginary-time evolution must be clear.
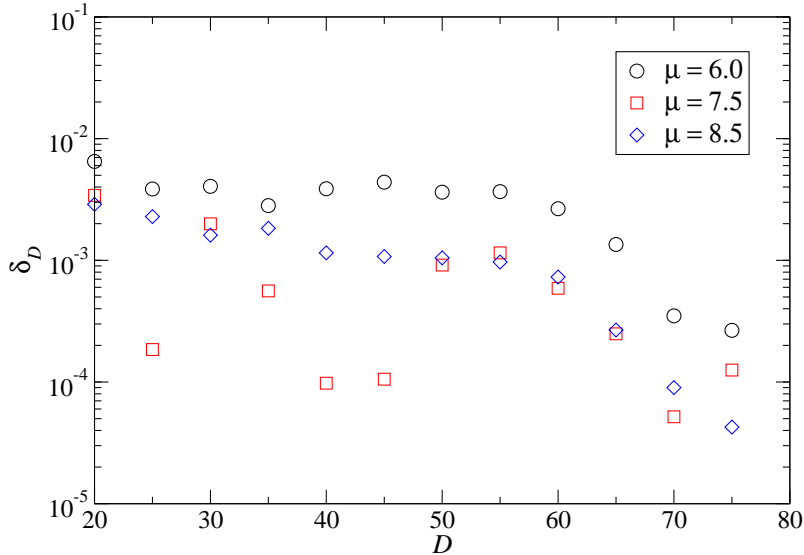
Figure 6.9: Convergence behavior of thermodynamic potential with δ_D of Eq. (6.45) at $U = 8$ with $\mu = 6.0$, 7.5, and 8.5 as a function of D on $V = 4096^2 \times 1677.7216$ lattice.

The deviation from the exact value can be estimated via the relative error,

$$\delta_{\text{exact}}(D) = \left| \frac{\ln Z(D) - \ln Z_{\text{exact}}}{\ln Z_{\text{exact}}} \right|. \tag{6.46}$$

In the computation shown in Fig. 6.10, we found that $\delta_{\text{exact}}(D)$ is at most $\mathcal{O}(10^{-4})$ in the range of $0 \leq \mu \leq 16$. For $\mu < 0$, the thermodynamic potential vanishes exactly and the TRG results are also equal to zero within a level of double precision. Although the one-site model is characterized by the vanishing hopping parameter t, this model can also be regarded as the infinite coupling limit, because $U/t \to \infty$ with $t \to 0$.

    As a finite-U/t generalization, we carry out the similar ATRG computation setting $(U, t) = (80, 1)$. Fig. 6.11 shows the number density in the vicinity of $\mu \sim U$ with $D = 80$. The convergence behavior of δ_D at $U = 80$ is better than that at $U = 8$. We can see that the number density starts to increase from $\langle n \rangle = 1$ at $\mu = 77.0(2)$, which is equivalent to $\mu/U = 0.9625(25)$, and it reaches $\langle n \rangle = 2$ with $\mu \gtrsim 83.0$, or equally to $\mu/U \gtrsim 1.04$. We expect that the critical chemical potential μ_{c} at the doping-driven metal-insulator transition approaches to $\mu_{\text{c}}/U = 1$, toward the one-site model ($U \to \infty$), and the transition from $\langle n \rangle = 1$ to $\langle n \rangle = 2$ will be described by a step function of μ/U as in Fig. 6.10. Note that μ dependence shown in Fig. 6.11 seems smooth and continuous and no signal of the first-order phase transition is found.

6.7.4 Intermediate and weak coupling regimes

Next, we investigate the metal-insulator transition in the intermediate coupling regime, choosing $(U, t) = (8, 1)$. Since we are interested in the thermodynamic limit at zero temperature, we start with checking the volume dependence of the number density $\langle n \rangle$. Fig. 6.12 shows $\langle n \rangle$ as a function
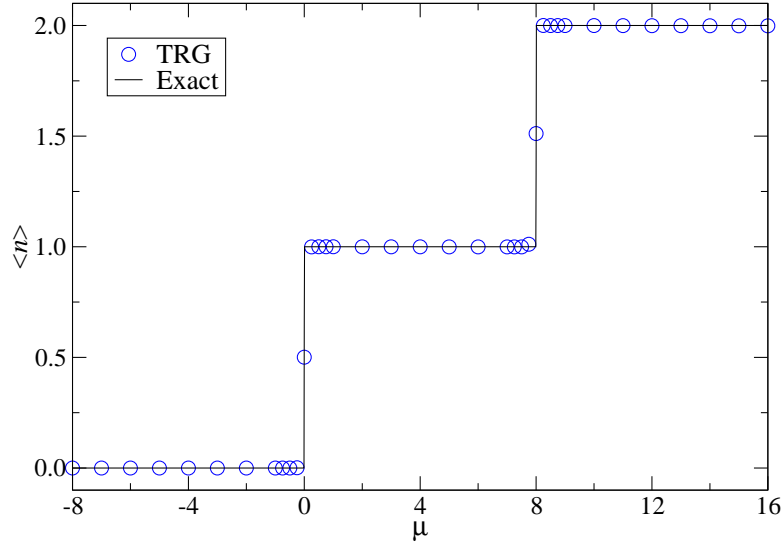
Figure 6.10: Electron density $\langle n \rangle$ in the $(U, t) = (8, 0)$ case at $\beta = 1677.7216$ with $\epsilon = 10^{-4}$ as a function of μ. The solid line shows the exact solution and the blue circles are the results obtained by the TRG.
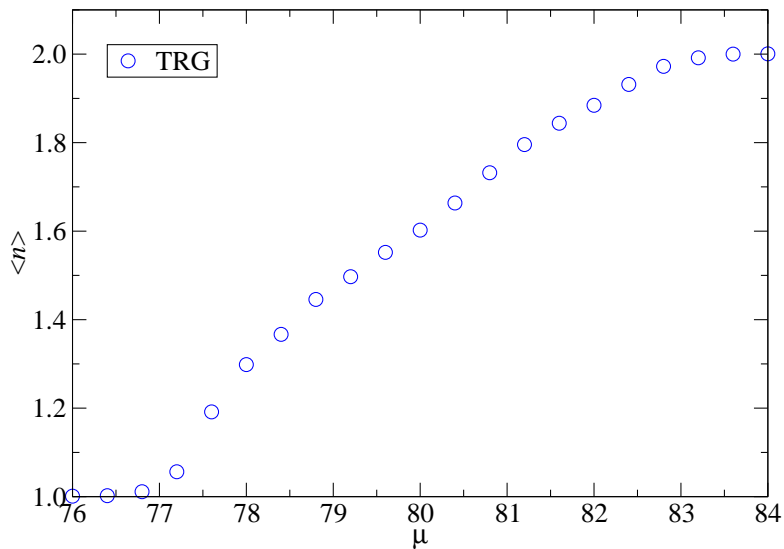
Figure 6.11: Electron density $\langle n \rangle$ as a function of μ at $(U, t) = (80, 1)$ on $V = 4096^2 \times 1677.7216$ with $\epsilon = 10^{-4}$. The bond dimension is set to be $D = 80$.

of μ, varying the lattice volumes, with $\epsilon = 10^{-4}$, $m_\tau = 12$ and $D = 80$. Fig. 6.12 confirms that the lattice whose volume is $(N_x, N_y, N_\tau) = (2^{12}, 2^{12}, 2^{24})$, which corresponds to $V = 4096^2 \times 1677.7216$, is sufficiently large to be identified as the thermodynamic limit at vanishing temperature. The plateau of $\langle n \rangle = 0$ is realized in $\mu \lesssim -4$ and that of $\langle n \rangle = 2$ is in $12 \lesssim \mu$. The half-filling state is characterized by the plateau of $\langle n \rangle = 1$ over the range of $2 \lesssim \mu \lesssim 6$. In these parameter regimes, the compressibility,

$$\kappa = \frac{\partial \langle n \rangle}{\partial \mu}, \tag{6.47}$$

vanishes and this indicates that the insulating phases take place. In order to determine the critical
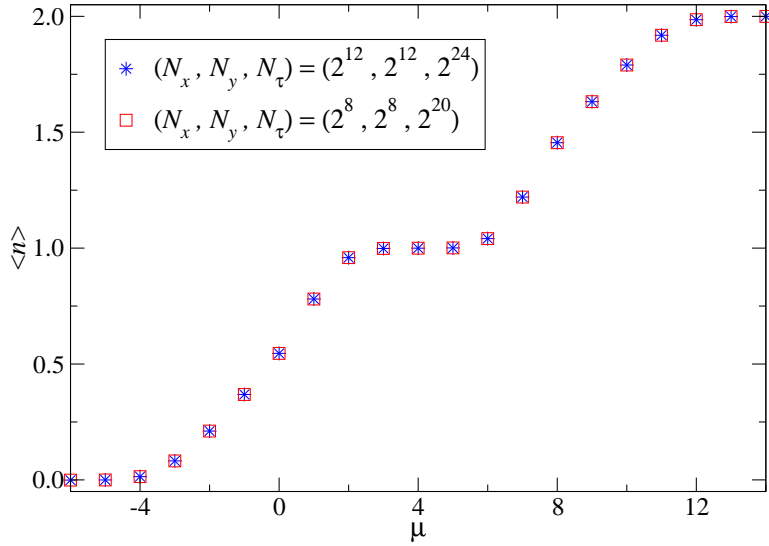
Figure 6.12: Electron density $\langle n \rangle$ at $U = 8$ on two lattice sizes, $V = 256^2 \times 104.8576$ and $4096^2 \times 1677.7216$, as a function of μ. The bond dimension is set to be $D = 80$.

chemical potential μ_c in the limit of $D \to \infty$ at $U = 8$ on $V = 4096^2 \times 1677.7216$ lattice, we perform a global fit of $\langle n \rangle$ with $D = 80$, 72, 64 and 56 in the metallic phase near the criticality. In Fig. 6.13, we plot $\langle n \rangle$, varying the bond dimension as $D = 80$, 72, 64 and 56 with a much finer resolution of $\Delta\mu$ than Fig. 6.12, focusing on $6.0 \leq \mu \leq 8.2$ to cover the region of $1 \leq \langle n \rangle \leq 1.5$. The results at $D = 80$, 72, 64, and 56 show similar μ dependence, we expect that the finite-D effect is sufficiently suppressed in the scope of this study. Employing

$$\langle n \rangle = 1 + \alpha \left(\mu - \mu_c(D) \right) + \beta \left(\mu - \mu_c(D) \right)^2, \tag{6.48}$$

as a fitting ansatz with $\mu_c(D) = \mu_c + \gamma/D$, where α, β, γ, and μ_c are the fitting parameters. The solid curves shown in Fig. 6.13 represent the results of fitting over $6.3 \leq \mu \leq 8.0$. We obtain $\mu_c = 6.43(4)$, which is presented in Table 6.4 together with other fitting results.

We repeat the same analysis in the weak coupling regime, setting $U = 2$. We apply the fit function in Eq. (6.48) to four data sets with $D = 80$, 72, 64, and 56. Numerical results and their fitting curves are shown in Fig. 6.14 and their fitting results are summarized in Table 6.4. Table 6.4 may imply
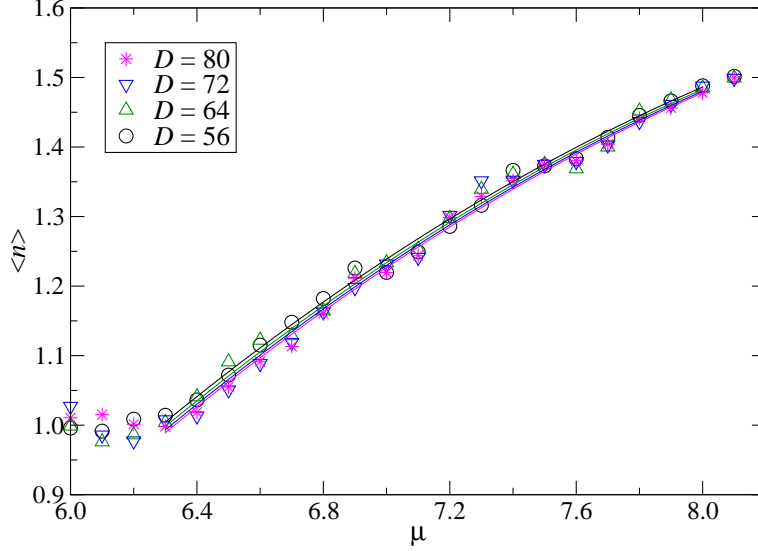
Figure 6.13: Electron density $\langle n \rangle$ at $U = 8$ on $V = 4096^2 \times 1677.7216$ with $\epsilon = 10^{-4}$ as a function of μ. The bond dimensions are $D = 80, 72, 64$ and 56. Fit results are drawn by the solid lines for each bond dimension.

that the deviation of $|\mu_{\mathrm{c}}(D) - U/2|$ diminishes as the Coulomb potential parameter U decreases and it is likely that $|\mu_{\mathrm{c}}(D) - U/2|$ vanishes only at $U = 0$. This provides us with a scenario of the phase diagram, where the two-dimensional Hubbard model may exhibit the metal-insulator transition over the wide regime of the finite coupling, including the weak coupling region. Although we did not discuss the magnetic ordering, this result is partially consistent with a recent Quantum MC calculation in Ref. [PBH+07].

Table 6.4: Critical chemical potential μ_{c} at $U = 8$ and 2 determined by the global fit of the data at $D = 80, 72, 64$, and 56.

U	8	2
fit range	[6.3, 8.0]	[1.2, 3.4]
μ_{c}	6.43(4)	1.30(6)
α	0.372(9)	0.39(1)
β	$-0.051(6)$	$-0.054(5)$
γ	$-7(2)$	$-13(4)$

6.8   Discussion

We applied the Grassmann TRG method to investigate the Hubbard model at finite density based on the path-integral formalism. To deal with a highly anisotropic lattice, we used the TRG algorithms
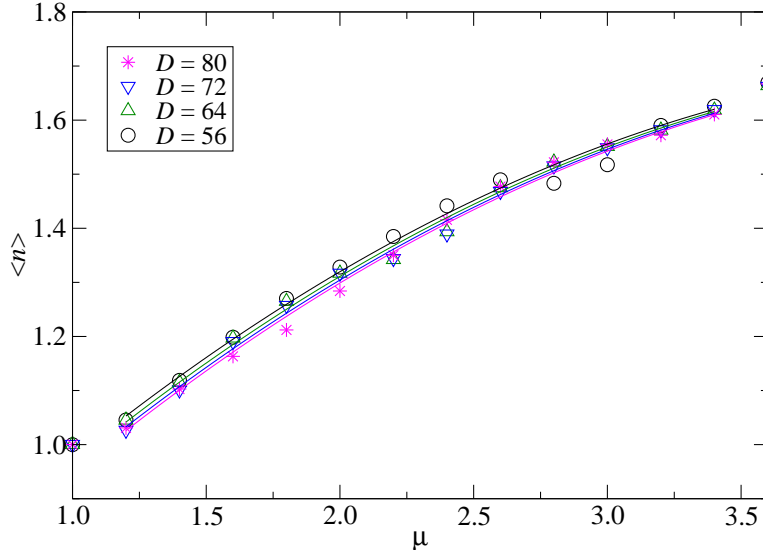
Figure 6.14: Electron density $\langle n \rangle$ at $U = 2$ on $V = 4096^2 \times 1677.7216$ with $\epsilon = 10^{-4}$ as a function of μ. The bond dimensions are $D = 80$, 72, 64 and 56. Fit results are drawn by the solid lines for each bond dimension.

firstly to consider the imaginary-time evolution and secondly to the spacetime coarse-graining. The efficiency of this treatment was confirmed in the $(1 + 1)$-dimensional study, where we investigated the one-site model, free field theory, and the model at $U = 4$. All results agree with their exact solutions, including the location of the critical chemical potential even in the presence of finite U/t. The scaling with respect to the bond dimension was necessary to restore the exact critical point in $(1+1)$ dimensions. The study was extended to the $(2 + 1)$-dimensional model, where we found a non-monotonic convergence of the thermodynamic potential with respect to the bond dimension as shown in Fig. 6.9. However, the TRG computation also found a clear signal of metal-insulator transition, identifying the Mott insulating phase characterized by $\langle n \rangle = 1$ as in Fig. 6.12. In addition, the current result seems consistent with a recent Quantum MC study [PBH+07] which implies the metal-insulator transition takes place at any finite U, including the weak coupling regime.

Investigation of the magnetic ordering in $(2+1)$-dimensional Hubbard model is one of the important future works. This can be carried out by using the impurity tensor method within the Grassmann TRG approach as demonstrated in Ref. [YKN+18]. Another research direction is the study of the $(3 + 1)$-dimensional Hubbard model at finite density, which may give us some insight also in the context of particle physics. This is because the structure of the Hubbard model is similar to the Nambu–Jona-Lasinio (NJL) model. Both models' actions are characterized by hopping terms, one-site terms, and four-point interactions, although the Hubbard model describes the non-relativistic fermions, the NJL model does the relativistic ones. This similarity introduces similar tensor network representations for them, so the similar efficiency of the TRG approach can be expected. It may be interesting to explore the phase diagrams of these models complementarily.

7   Nambu–Jona-Lasinio model at finite density

The last model we investigate is the Nambu–Jona-Lasinio (NJL) model [NJL61a, NJL61b]. The continuum NJL model is defined by the Lagrangian density,

$$\mathcal{L} = \sum_{\nu=1}^{4} \bar{\psi}(x)\gamma_\nu\partial_\nu\psi(x) - g_0\left\{(\bar{\psi}(x)\psi(x))^2 + (\bar{\psi}(x)\mathrm{i}\gamma_5\psi(x))^2\right\}, \tag{7.1}$$

which has the U(1) chiral symmetry with $\psi(x) \mapsto \mathrm{e}^{\mathrm{i}\alpha\gamma_5}\psi(x)$ and $\bar{\psi}(x) \mapsto \bar{\psi}(x)\mathrm{e}^{\mathrm{i}\alpha\gamma_5}$ ($\alpha \in \mathbb{R}$). Originally, Nambu and Jona-Lasinio employed the Hartree-Fock approximation to see that this model described the dynamical creation of a condensate from fermion interactions, which is nothing but the spontaneous breaking of chiral symmetry. Once the strength of the coupling constant g_0 exceeds a certain critical value, the system generates a non-trivial vacuum with finite $\langle\bar{\psi}(x)\psi(x)\rangle$. Since the NJL model is an effective theory of the Quantum Chromodynamics (QCD), the model at finite temperature T and finite chemical potential μ is of great importance in the context of the QCD phase diagram in the T-μ plane. In addition, the equation of state for the QCD at finite temperature and density is an essential ingredient to understand the evolution and the current state of our universe, quantitatively. To this aim, the lattice QCD simulation has been playing a significant role to study the non-perturbative physics in the QCD. However, it has not been successful to reveal the nature of the QCD at finite density, due to the sign problem. This is because the lattice QCD simulation is based on the MC method and once the finite chemical potential is introduced, the lattice QCD simulation encounters the sign problem. For a recent status of the lattice QCD simulation at finite density, see Refs. [dF09, Nag21], for example.

The chiral phase structure of the NJL model on the T-μ plane has been discussed by some analytical methods such as the mean-field approximation [Bub05] or the functional renormalization group (FRG) [AKY18]. Figure 7.1 shows a schematic illustration of the expected phase structure. One of the characteristic features is the first-order chiral phase transition in the dense region at very low temperature, where the chiral symmetry is expected to be restored [AY89]. Our primary target is this chiral phase transition. The TRG analysis of this phase structure would help us understand the QCD thermodynamics and will pave the way toward a direct study of the QCD at finite temperature and density with the TRG in the future. The following is based on Ref. [AKYY21], which is the first application of the TRG approach to the four-dimensional fermionic theory.

7.1   Staggered formulation on a $(3+1)$-dimensional lattice

Since the chiral symmetry plays a crucial role in this study, we use the staggered fermion [KS75] to formulate the NJL model on the lattice. Following Refs. [LS87, BKP89], we define the model at finite chemical potential μ as

$$S = \frac{1}{2}a^3 \sum_{n\in\Lambda_{3+1}} \sum_{\nu=1}^{4} \eta_\nu(n) \left[\mathrm{e}^{\mu a\delta_{\nu,4}}\bar{\chi}(n)\chi(n+\hat{\nu}) - \mathrm{e}^{-\mu a\delta_{\nu,4}}\bar{\chi}(n+\hat{\nu})\chi(n)\right]$$

$$+ ma^4 \sum_{n\in\Lambda_{3+1}} \bar{\chi}(n)\chi(n) - g_0 a^4 \sum_{n\in\Lambda_{3+1}} \sum_{\nu=1}^{4} \bar{\chi}(n)\chi(n)\bar{\chi}(n+\hat{\nu})\chi(n+\hat{\nu}), \tag{7.2}$$

with the lattice spacing a. m denote mass of the fermion. $\chi(n)$ and $\bar{\chi}(n)$ are Grassmann-valued fields without the Dirac structure. Since they describe the staggered fermions, $\chi(n)$ and $\bar{\chi}(n)$ are single-component Grassmann fields. We regard 1-, 2-, and 3-directions as spatial directions and assume

71
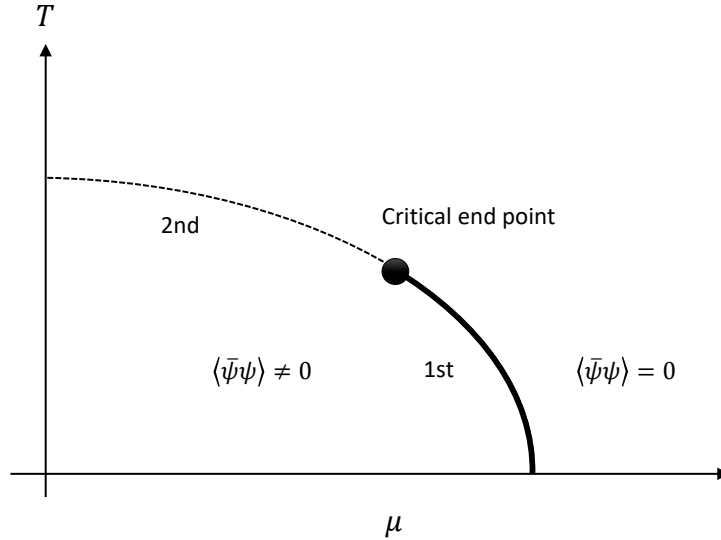
Figure 7.1: Schematic view of expected phase diagram of the NJL model on the T-μ plane. Solid and broken curves represent the first- and second-order phase transitions, respectively. Closed circle denotes the critical end point (CEP) where the first-order phase transition line terminates.

the periodic boundary conditions. 4-direction is identified as a temporal direction, where we assume anti-periodic boundary condition. $\eta_\nu(n)$ is the staggered sign function defined by

$$\eta_\nu(n) = (-1)^{n_1 + \cdots + n_{\nu-1}}, \tag{7.3}$$

with $\eta_1(n) = 1$. We assume the periodic boundary conditions for 1-, 2-, 3-directions and the anti-periodic boundary condition for 4-direction. With vanishing mass m, Eq. (7.2) is invariant under the following continuous chiral transformations,

$$\chi(n) \mapsto e^{i\alpha\epsilon(n)}\chi(n), \tag{7.4}$$

$$\bar\chi(n) \mapsto \bar\chi(n)e^{i\alpha\epsilon(n)}, \tag{7.5}$$

with $\alpha \in \mathbb{R}$ and $\epsilon(n) = (-1)^{n_1 + n_2 + n_3 + n_4}$. The path integral generated by Eq. (7.2) is

$$Z = \left(\prod_{n \in \Lambda_{3+1}} \int \int d\chi(n)d\bar\chi(n) \right) e^{-S}. \tag{7.6}$$

For those who are interested in the relation between the staggered fermions and the Dirac fermions, see Appendix C.

7.2 Tensor network representation

The tensor network representation of Eq. (7.6) is straightforwardly obtained as in the case of the Hubbard model. [1] Hereafter, we set $a = 1$. Decomposing hopping structures via

$$\exp\left[-\frac{e^{\mu\delta_{\nu,4}}}{2}\eta_\nu(n)\bar{\chi}(n)\chi(n+\hat{\nu})\right]$$
$$= \int\int d\bar{\zeta}_\nu(n)d\zeta_\nu(n)\ e^{-\bar{\zeta}_\nu(n)\zeta_\nu(n)}\exp\left[-\frac{e^{\frac{\mu}{2}\delta_{\nu,4}}}{\sqrt{2}}\eta_\nu(n)\bar{\chi}(n)\zeta_\nu(n) - \frac{e^{\frac{\mu}{2}\delta_{\nu,4}}}{\sqrt{2}}\chi(n+\hat{\nu})\bar{\zeta}_\nu(n)\right], \qquad (7.7)$$

$$\exp\left[\frac{e^{-\mu\delta_{\nu,4}}}{2}\eta_\nu(n)\bar{\chi}(n+\hat{\nu})\chi(n)\right]$$
$$= \int\int d\bar{\xi}_\nu(n)d\xi_\nu(n)\ e^{-\bar{\xi}_\nu(n)\xi_\nu(n)}\exp\left[-\frac{e^{-\frac{\mu}{2}\delta_{\nu,4}}}{\sqrt{2}}\bar{\chi}(n+\hat{\nu})\bar{\xi}_\nu(n) - \frac{e^{-\frac{\mu}{2}\delta_{\nu,4}}}{\sqrt{2}}\eta_\nu(n)\chi(n)\xi_\nu(n)\right], \quad (7.8)$$

$$e^{g_0\bar{\chi}(n)\chi(n)\bar{\chi}(n+\hat{\nu})\chi(n+\hat{\nu})} = \int\int d\bar{\phi}_\nu(n)d\phi_\nu(n)\ e^{-\bar{\phi}_\nu(n)\phi_\nu(n)}\int\int d\bar{\omega}_\nu(n)d\omega_\nu(n)\ e^{-\bar{\omega}_\nu(n)\omega_\nu(n)}$$
$$\times \exp\left[\sqrt{g_0}\bar{\chi}(n)\chi(n)\phi_\nu(n)\omega_\nu(n) + \sqrt{g_0}\bar{\chi}(n+\hat{\nu})\chi(n+\hat{\nu})\bar{\omega}_\nu(n)\bar{\phi}_\nu(n)\right]. \quad (7.9)$$

In Eq. (7.9), two kinds of auxiliary Grassmann fields are introduced in order to make the resulting exponential factors Grassmann-even. Integrating out χ and $\bar{\chi}$ at each lattice site n independently, we can define

$$\mathcal{T}_{\Psi_1(n)\Psi_2(n)\Psi_3(n)\Psi_4(n)\bar{\Psi}_4(n-\hat{4})\bar{\Psi}_3(n-\hat{3})\bar{\Psi}_2(n-\hat{2})\bar{\Psi}_1(n-\hat{1})}$$
$$= \int\int d\chi d\bar{\chi}\ e^{-m\bar{\chi}\chi}\exp\left[-\frac{e^{\frac{\mu}{2}\delta_{\nu,4}}}{\sqrt{2}}\eta_\nu(n)\bar{\chi}\zeta_\nu(n) - \frac{e^{\frac{\mu}{2}\delta_{\nu,4}}}{\sqrt{2}}\chi\bar{\zeta}_\nu(n-\hat{\nu})\right]$$
$$\times \exp\left[-\frac{e^{-\frac{\mu}{2}\delta_{\nu,4}}}{\sqrt{2}}\bar{\chi}\bar{\xi}_\nu(n-\hat{\nu}) - \frac{e^{-\frac{\mu}{2}\delta_{\nu,4}}}{\sqrt{2}}\eta_\nu(n)\chi\xi_\nu(n)\right]$$
$$\times \exp\left[\sqrt{g_0}\bar{\chi}\chi\phi_\nu(n)\omega_\nu(n) + \sqrt{g_0}\bar{\chi}\chi\bar{\omega}_\nu(n-\hat{\nu})\bar{\phi}_\nu(n-\hat{\nu})\right], \qquad (7.10)$$

with $\Psi_\nu = (\zeta_\nu, \xi_\nu, \phi_\nu, \omega_\nu)$ and $\bar{\Psi}_\nu = (\bar{\zeta}_\nu, \bar{\xi}_\nu, \bar{\phi}_\nu, \bar{\omega}_\nu)$. Eq. (7.6) is now expressed by the Grassmann tensor network,

$$Z = \mathrm{gTr}\left[\prod_{n\in\Lambda_{3+1}}\mathcal{T}_{\Psi_1(n)\Psi_2(n)\Psi_3(n)\Psi_4(n)\bar{\Psi}_4(n-\hat{4})\bar{\Psi}_3(n-\hat{3})\bar{\Psi}_2(n-\hat{2})\bar{\Psi}_1(n-\hat{1})}\right]. \qquad (7.11)$$

---

[1]In Ref. [AKYY21], we present an alternative derivation based on Refs. [TY15, KKN⁺18]. See Ref. [BCM⁺20] for a different TRG approach with the staggered fermion, where the TRG is applied to the Schwinger model after integrating out the fermion fields analytically.

Let us explicitly carry out the integration in Eq. (7.10).

$$
\mathcal{T}_{\Psi_1\Psi_2\Psi_3\Psi_4\bar{\Psi}_4\bar{\Psi}_3\bar{\Psi}_2\bar{\Psi}_1} = \left(\prod_{\nu=1}^{4} \sum_{i_\nu, j_\nu, k_\nu} \sum_{i'_\nu, j'_\nu, k'_\nu} \right)
$$
$$
\times \left(\prod_\nu \eta_\nu(n)^{i_\nu+j_\nu} \left(\frac{\mathrm{e}^{\frac{\mu}{2}\delta_{\nu,4}}}{\sqrt{2}} \right)^{i_\nu+i'_\nu} \left(\frac{\mathrm{e}^{-\frac{\mu}{2}\delta_{\nu,4}}}{\sqrt{2}} \right)^{j_\nu+j'_\nu} \right) \sqrt{g_0}^{\sum_\nu(k_\nu+k'_\nu)}
$$
$$
\times \left[\delta_{1,\sum_\nu(i_\nu+j'_\nu+k_\nu+k'_\nu)}\delta_{1,\sum_\nu(i'_\nu+j_\nu+k_\nu+k'_\nu)} - m\delta_{0,\sum_\nu(i_\nu+j'_\nu+k_\nu+k'_\nu)}\delta_{0,\sum_\nu(i'_\nu+j_\nu+k_\nu+k'_\nu)} \right]
$$
$$
\times \left(\prod_\nu \bar{\zeta}_\nu^{i'_\nu} \right) \left(\prod_\nu \xi_\nu^{j_\nu} \right) \left(\prod_\nu (\bar{\omega}_\nu\bar{\phi}_\nu)^{k'_\nu} \right) \left(\prod_\nu (\phi_\nu\omega_\nu)^{k_\nu} \right) \left(\prod_\nu \bar{\xi}_\nu^{j'_\nu} \right) \left(\prod_\nu \zeta_\nu^{i_\nu} \right),
$$
$$(7.12)$$

where we assigned the subscripts $i_\nu(n)$, $j_\nu(n)$, and $k_\nu(n)$ as the labels of the Taylor expansion for Eqs. (7.7), (7.8), and (7.9), respectively. As we defined previously, $i'_\nu(n) = i_\nu(n-\hat{\nu})$ and so on. We sort the auxiliary Grassmann fields in Eq. (7.12) as those in Eq. (7.13), which is

$$
\mathcal{T}_{\Psi_1\Psi_2\Psi_3\Psi_4\bar{\Psi}_4\bar{\Psi}_3\bar{\Psi}_2\bar{\Psi}_1} = \left(\prod_{\nu=1}^{4} \sum_{i_\nu, j_\nu, k_\nu} \sum_{i'_\nu, j'_\nu, k'_\nu} \right)
$$
$$
\times T_{(i_1,j_1,k_1)(i_2,j_2,k_2)(i_3,j_3,k_3)(i_4,j_4,k_4)(i'_1,j'_1,k'_1)(i'_2,j'_2,k'_2)(i'_3,j'_3,k'_3)(i'_4,j'_4,k'_4)}
$$
$$
\times \left(\zeta_1^{i_1}\xi_1^{j_1}(\phi_1\omega_1)^{k_1} \right) \left(\zeta_2^{i_2}\xi_2^{j_2}(\phi_2\omega_2)^{k_2} \right) \left(\zeta_3^{i_3}\xi_3^{j_3}(\phi_3\omega_3)^{k_3} \right) \left(\zeta_4^{i_4}\xi_4^{j_4}(\phi_4\omega_4)^{k_4} \right)
$$
$$
\times \left((\bar{\omega}_4\bar{\phi}_4)^{k'_4}\bar{\xi}_4^{j'_4}\bar{\zeta}_4^{i'_4} \right) \left((\bar{\omega}_3\bar{\phi}_3)^{k'_3}\bar{\xi}_3^{j'_3}\bar{\zeta}_3^{i'_3} \right) \left((\bar{\omega}_2\bar{\phi}_2)^{k'_2}\bar{\xi}_2^{j'_2}\bar{\zeta}_2^{i'_2} \right) \left((\bar{\omega}_1\bar{\phi}_1)^{k'_1}\bar{\xi}_1^{j'_1}\bar{\zeta}_1^{i'_1} \right). \quad (7.13)
$$

The coefficient tensor T in Eq. (7.13) is given by

$$
T_{(i_1,j_1,k_1)(i_2,j_2,k_2)(i_3,j_3,k_3)(i_4,j_4,k_4)(i'_1,j'_1,k'_1)(i'_2,j'_2,k'_2)(i'_3,j'_3,k'_3)(i'_4,j'_4,k'_4)}
$$
$$
= \left(\prod_\nu \eta_\nu(n)^{i_\nu+j_\nu} \left(\frac{\mathrm{e}^{\frac{\mu}{2}\delta_{\nu,4}}}{\sqrt{2}} \right)^{i_\nu+i'_\nu} \left(\frac{\mathrm{e}^{-\frac{\mu}{2}\delta_{\nu,4}}}{\sqrt{2}} \right)^{j_\nu+j'_\nu} \right) \sqrt{g_0}^{\sum_\nu(k_\nu+k'_\nu)}
$$
$$
\times \left[\delta_{1,\sum_\nu(i_\nu+j'_\nu+k_\nu+k'_\nu)}\delta_{1,\sum_\nu(i'_\nu+j_\nu+k_\nu+k'_\nu)} - m\delta_{0,\sum_\nu(i_\nu+j'_\nu+k_\nu+k'_\nu)}\delta_{0,\sum_\nu(i'_\nu+j_\nu+k_\nu+k'_\nu)} \right]
$$
$$
\times (-1)^{R_{(i_1,j_1,k_1)(i_2,j_2,k_2)(i_3,j_3,k_3)(i_4,j_4,k_4)(i'_1,j'_1,k'_1)(i'_2,j'_2,k'_2)(i'_3,j'_3,k'_3)(i'_4,j'_4,k'_4)}}, \quad (7.14)
$$

with

$$
R_{(i_1,j_1,k_1)(i_2,j_2,k_2)(i_3,j_3,k_3)(i_4,j_4,k_4)(i_1',j_1',k_1')(i_2',j_2',k_2')(i_3',j_3',k_3')(i_4',j_4',k_4')}
$$

$$
= i_1 \left(\sum_{\nu=1}^{4} i_\nu' + \sum_{\nu=1}^{4} j_\nu + \sum_{\nu=1}^{4} k_\nu' + \sum_{\nu=1}^{4} k_\nu + \sum_{\nu=1}^{4} j_\nu' \right) + j_1 \sum_{\nu=1}^{4} i_\nu' + k_1 \left(\sum_{\nu=1}^{4} i_\nu' + \sum_{\nu=2}^{4} j_\nu + \sum_{\nu=1}^{4} k_\nu' \right)
$$

$$
+ i_2 \left(\sum_{\nu=1}^{4} i_\nu' + \sum_{\nu=2}^{4} j_\nu + \sum_{\nu=1}^{4} k_\nu' + \sum_{\nu=2}^{4} k_\nu + \sum_{\nu=1}^{4} j_\nu' \right) + j_2 \sum_{\nu=1}^{4} i_\nu' + k_2 \left(\sum_{\nu=1}^{4} i_\nu' + \sum_{\nu=3}^{4} j_\nu + \sum_{\nu=1}^{4} k_\nu' \right)
$$

$$
+ i_3 \left(\sum_{\nu=1}^{4} i_\nu' + \sum_{\nu=3}^{4} j_\nu + \sum_{\nu=1}^{4} k_\nu' + \sum_{\nu=3}^{4} k_\nu + \sum_{\nu=1}^{4} j_\nu' \right) + j_3 \sum_{\nu=1}^{4} i_\nu' + k_3 \left(\sum_{\nu=1}^{4} i_\nu' + j_4 + \sum_{\nu=1}^{4} k_\nu' \right)
$$

$$
+ i_4 \left(\sum_{\nu=1}^{4} i_\nu' + j_4 + \sum_{\nu=3}^{4} k_\nu' + \sum_{\nu=1}^{4} k_\nu + \sum_{\nu=1}^{4} j_\nu' \right) + j_4 \sum_{\nu=1}^{4} i_\nu' + k_4 \left(\sum_{\nu=1}^{4} i_\nu' + \sum_{\nu=1}^{4} k_\nu' \right)
$$

$$
+ k_4' \left(\sum_{\nu=1}^{4} i_\nu' + \sum_{\nu=1}^{3} k_\nu' \right) + j_4' \left(\sum_{\nu=1}^{4} i_\nu' + \sum_{\nu=1}^{3} k_\nu' + \sum_{\nu=1}^{3} j_\nu' \right) + i_4' \sum_{\nu=1}^{3} i_\nu'
$$

$$
+ k_3' \left(\sum_{\nu=1}^{3} i_\nu' + \sum_{\nu=1}^{2} k_\nu' \right) + j_3' \left(\sum_{\nu=1}^{3} i_\nu' + \sum_{\nu=1}^{2} k_\nu' + \sum_{\nu=1}^{2} j_\nu' \right) + i_3' \sum_{\nu=1}^{2} i_\nu'
$$

$$
+ k_2' \left(\sum_{\nu=1}^{2} i_\nu' + k_1' \right) + j_2' \left(\sum_{\nu=1}^{2} i_\nu' + k_1' + j_1' \right) + i_2' i_1'
$$

$$
+ k_1' i_1' + j_1' i_1'. \tag{7.15}
$$

As we explained previously, it is practically useful to encode the Grassmann parity of the auxiliary Grassmann fields into the subscripts of the coefficient tensor T, which is identified as a $2d$-rank tensor $T_{I_1 I_2 I_3 I_4 I_1' I_2' I_3' I_4'}$, where $I_\nu^{(')} = 1, \cdots, 8$ for all ν. We define $I_\nu^{(')}$ as in Table 7.1. Notice that $I_\nu^{(')} = 1, \cdots, 4$ correspond to the Grassmann-even sector and $I_\nu^{(')} = 5, \cdots, 8$ to the Grassmann-odd one in Ψ_ν ($\bar{\Psi}_\nu$). As shown in Table 7.1, the Grassmann parity is independent of $k_\nu^{(')}$. This fact is understood by looking at Eq. (7.13), where $k_\nu^{(')}$ always appears as an exponent of $\phi_\nu \omega_\nu$ ($\bar{\omega}_\nu \bar{\phi}_\nu$) whose Grassmann parity is even. Reflecting on the stagger phase function $\eta_\nu(n)$, the resulting Grassmann tensor network also

Table 7.1: Mapping of subscripts.

$I_\nu^{(')}$	1	2	3	4	5	6	7	8
$i_\nu^{(')}$	0	1	0	1	1	0	1	0
$j_\nu^{(')}$	0	1	0	1	0	1	0	1
$k_\nu^{(')}$	0	0	1	1	0	1	0	1

has a staggered structure. As in Eq. (7.14), the resulting Grassmann tensor $\mathcal{T}$ does depend on the parity of $n \in \Lambda_{3+1}$. Since we defined $\eta_\nu(n)$ by Eq. (7.3), there is a periodic structure for the spatial parity and a uniform structure along the temporal direction. A schematic demonstration is found in Fig. 7.2 (A).
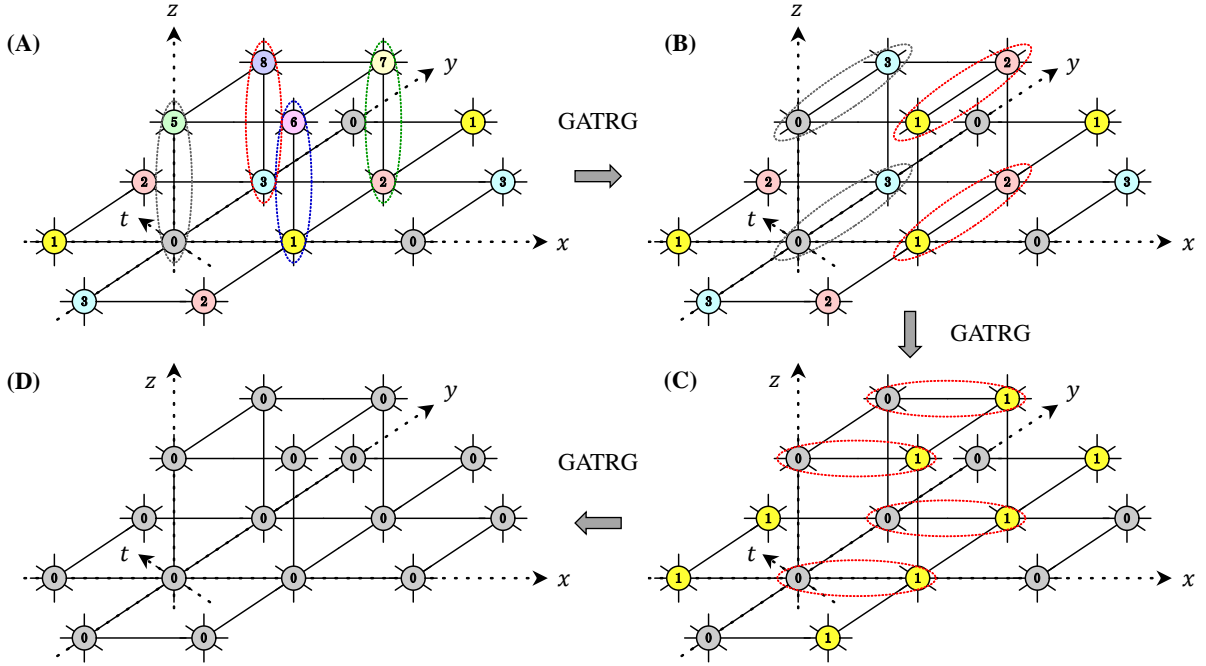
Figure 7.2: Schematic illustration of the Grassmann ATRG (GATRG). Coordinate axes in Λ_{3+1} are shown as dotted lines with arrows. Different numbers are assigned to specify different tensors. (A) Initial tensor network in Eq. (7.11). Eight types of tensors are located at a spatial unit cube. A periodic structure is explicitly shown on x-y plane. The tensor network is uniform in t-direction. (B) The first coarse-graining along z-direction reduces types of tensor from eight to four. The tensor network becomes uniform in t-, z-directions. (C) The second coarse-graining along y-direction makes the structure uniform except in x-direction. (D) A uniform tensor network is obtained by the third coarse-graining along x-direction. In the following coarse-graining steps, the structure is invariant.

7.3 Procedure of TRG calculation

To evaluate the Grassmann tensor network in Eq. (7.11), we employ the ATRG algorithm. Hereafter, we refer 1-, 2-, 3-, and 4-directions as x-, y-, z-, and t-directions, respectively. In the initial Grassmann tensor network of Eq. (7.11), where are eight types of Grassmann tensors (Fig. 7.2 (A)). Firstly, we carry out the renormalization-group transformation along the z-direction, which reduces the total number of the Grassmann tensors from eight to four (Fig. 7.2 (B)). Secondly, we repeat it but along the y-direction (Fig. 7.2 (C)). Similarly, we again repeat it but along the x-direction (Fig. 7.2 (D)), where there is just a single kind of Grassmann tensor in the Grassmann tensor network. After that, we can normally employ the ATRG algorithm to access the thermodynamic limit at zero temperature.

7.4 Heavy dense limit as a benchmark

Before we investigate the chiral-symmetry restoration at vanishing fermion mass, let us confirm the efficiency of the Grassmann ATRG (GATRG) algorithm by benchmarking with the model in the so-called heavy dense limit, which is defined as $m \to \infty$ and $\mu \to \infty$, with keeping e^{μ}/m fixed. We can compare the numerical results with the exact solution in the heavy dense limit, where the number density $\langle n \rangle$ and the fermion condensate $\langle \bar{\chi}(n)\chi(n) \rangle$ at zero temperature is derived analytically as

$$\langle n \rangle = \Theta(\mu - \mu_{\mathrm{c}}), \tag{7.16}$$

$$\langle \bar{\chi}(n)\chi(n) \rangle = \frac{1}{m}\Theta(\mu_{\mathrm{c}} - \mu), \tag{7.17}$$

where Θ denotes the step function and $\mu_{\mathrm{c}} = \ln(2m)$ [PZ13].

    Figures 7.3 and 7.4 show the numerical results for $\langle n \rangle$ and $\langle \bar{\chi}(n)\chi(n) \rangle$ as functions of chemical potential μ, setting $m = 10^4$ and $D = 30$. The number density is calculated by the numerical derivative such that

$$\langle n \rangle = \frac{1}{V}\frac{\partial \ln Z(\mu)}{\partial \mu} \approx \frac{1}{V}\frac{\ln Z(\mu + \Delta\mu) - \ln Z(\mu)}{\Delta\mu}. \tag{7.18}$$

Just in the vicinity of μ_{c}, we set $\Delta\mu = 4.0 \times 10^{-3}$. The fermion condensate is also obtained by the numerical derivative with respect to m,

$$\langle \bar{\chi}(n)\chi(n) \rangle|_{m=10^4} = \frac{1}{V}\frac{\ln Z(m + \Delta m) - \ln Z(m)}{\Delta m}\bigg|_{m=10^4}, \tag{7.19}$$

with $\Delta m = 1$. Since there is little difference between the results obtained on the lattice volumes $V = 128^4$ and 1024^4, the $V = 1024^4$ lattice is sufficiently large to be identified as the thermodynamic limit at zero temperature. The numerical results well reproduce the analytical ones, including the location of $\mu_{\mathrm{c}} = \ln(2m) = 9.903$, both for $\langle n \rangle$ and $\langle \bar{\chi}(n)\chi(n) \rangle$. Note that the numerical difference between $\ln Z(D = 25)$ and $\ln Z(D = 30)$ has been already suppressed less than $2.1 \times 10^{-3}\%$ even in the vicinity of μ_{c}.

7.5 Chiral phase transition

Having confirmed the efficiency of the algorithm in the heavy dense limit, we now turn to the calculation with the light fermion masses. We set $g_0 = 32$ for the four-fermi coupling in Eq. (7.2), because
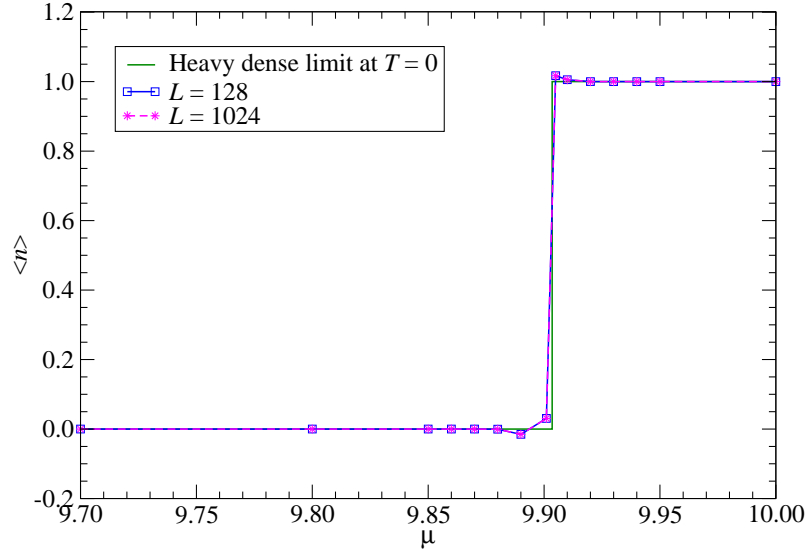
Figure 7.3: Number density at $m = 10^4$ and $g_0 = 32$ on 128^4 and 1024^4 lattices as a function of μ with $D = 30$. $\Delta\mu = 4.0 \times 10^{-3}$ in the vicinity of μ_c. Green line denotes the step function in Eq. (7.16).
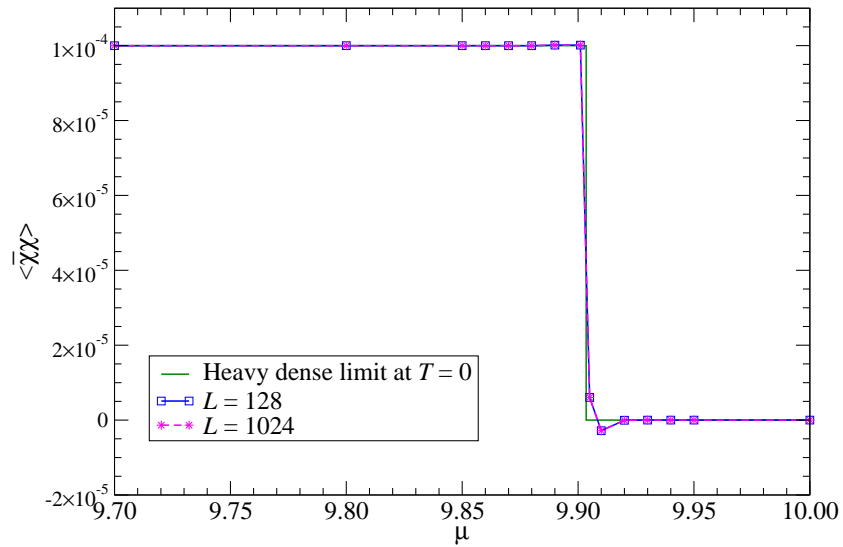
Figure 7.4: Fermion condensate at $m = 10^4$ and $g_0 = 32$ on 128^4 and 1024^4 lattices as a function of μ with $D = 30$. Green line denotes the step function in Eq. (7.17).

the FRG analysis in Ref. [AKY18] indicates the vanishing phase transition for smaller g_0. We first check the convergence of the thermodynamic potential by defining the relative error as

$$\delta_D = \left| \frac{\ln Z(D) - \ln Z(D = 55)}{\ln Z(D = 55)} \right| \tag{7.20}$$

on $V = 1024^4$. Fig. 7.5 plots δ_D at $\mu = 2.875$, which is in the vicinity of the transition point and $\mu = 4.0$, which is in the denser region with the restored chiral symmetry, as we will see below. Although both of them are in the cold and dense region characterized with $\mu/T \sim \mathcal{O}(10^3)$, where the MC simulation should be severely hindered by the sign problem, the convergence for the bond dimension is confirmed. Near the transition point, δ_D is reduced to about 10^{-4} up to $D = 55$. The convergence becomes better in the denser regime, $\delta_D \lesssim 10^{-7}$. Hereafter we always set $D = 55$.
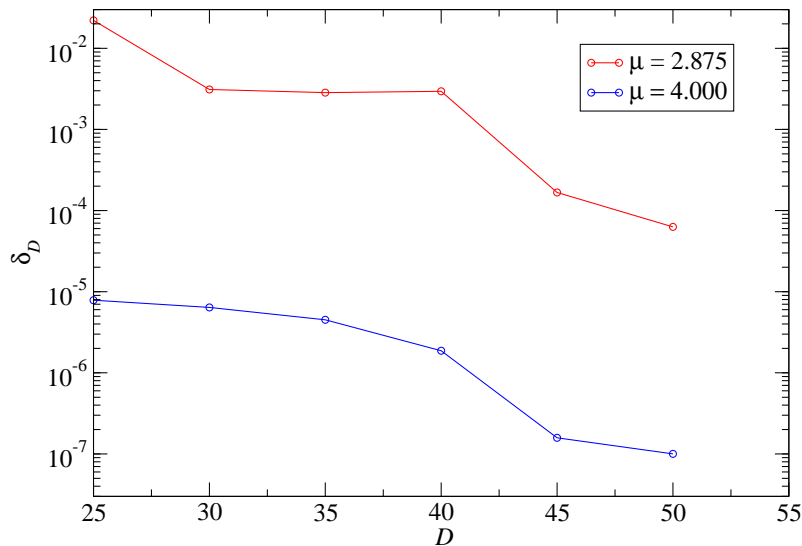
Figure 7.5: Convergence behavior of thermodynamic potential as a function of D on $V = 1024^4$ with $m = 0.01$.

We investigate the chiral phase transition, employing the chiral condensate $\langle \bar{\chi}(n)\chi(n) \rangle$, as an order parameter, which is defined by

$$\langle \bar{\chi}(n)\chi(n) \rangle = \lim_{m \to 0} \lim_{V \to \infty} \frac{1}{V} \frac{\partial}{\partial m} \ln Z, \tag{7.21}$$

in the cold regime. We calculate $\langle \bar{\chi}(n)\chi(n) \rangle$ by the numerical derivative as in the calculation of the heavy dense limit and the chiral extrapolation with the corresponding results at finite mass in the thermodynamic limit. [2] The partial derivative in Eq. (7.21) is numerically evaluated via

$$\frac{\partial}{\partial m} \ln Z \approx \frac{\ln Z(m + \Delta m) - \ln Z(m)}{\Delta m}, \tag{7.22}$$

---

[2]It is possible to evaluate the chiral condensate with the impurity tensor method [YKN+18,MOR19]. Since Eq. (7.11) consists of eight types of tensor, there are eight configurations of an impurity tensor. Consequently, the computational cost is eight times larger than that of coarse-graining Eq. (7.11). One can also evaluate the number density discussed below with the impurity tensor method, which requires four times larger cost than that to coarse-grain Eq. (7.11).

with $\Delta m = 0.01$. In Fig. 7.6, we show the chiral condensate as a function of μ at $m = 0.01$ and 0.02 on the $V = 1024^4$ lattice. The signals show slight fluctuations as a function of μ around the transition point. Away from the transition point, we found little response in $\langle \bar{\chi}(n)\chi(n) \rangle$ to changes in mass. Figure 7.7 presents the chiral limit which is estimated by the chiral extrapolation with the data at $m = 0.01$ and 0.02 on $V = 128^4$ and 1024^4 lattices. It is hard to find the difference between the results on these two lattice volumes, so we successfully reaches the thermodynamic limit at vanishing temperature. We observe the discontinuity from a finite value to zero for the chiral condensate at $\mu_c = 3.0625 \pm 0.0625$, which indicates the first-order phase transition.
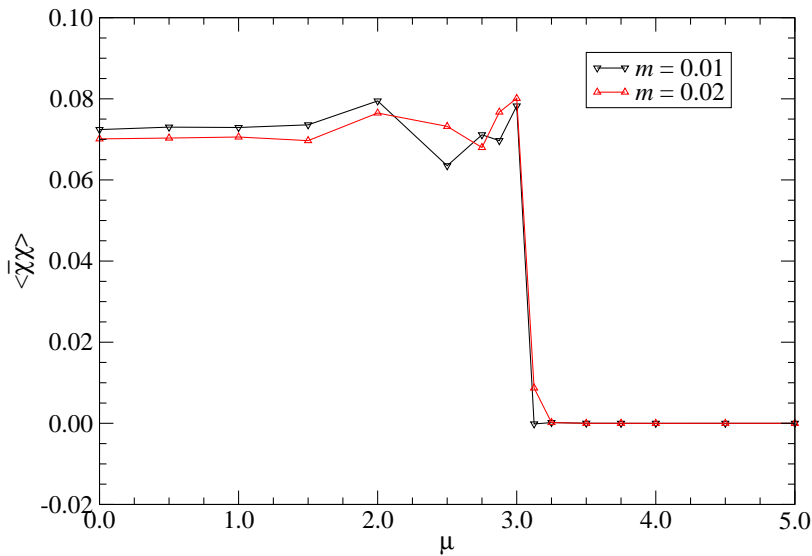
Figure 7.6: Chiral condensate at $m = 0.01$ and 0.02 on 1024^4 lattice as a function of μ with $D = 55$.

7.6   Equation of state

The equation of state tells us a relationship between the pressure and the particle number density. In the thermodynamic limit, the pressure P is directly obtained as the thermodynamic potential,

$$P = \frac{\ln Z}{V}, \tag{7.23}$$

where the vast homogeneous system is assumed. Since the TRG approach allows us to compute the path integral Z directly, we can easily obtain the pressure P as a function of a certain parameter. Figure 7.8, shows P as a function of μ at $m = 0.01$. We find a kink behavior at $\mu_c = 3.0625 \pm 0.0625$, where the chiral condensate shows the discontinuity. We confirmed that the result at $m = 0.02$ shows little difference from Fig. 7.8. In addition, we can see that the Silver Blaze phenomenon takes place. Fig. 7.9 shows the particle number density $\langle n \rangle$ also as a function of chemical potential. This is obtained by Eq. (7.18). An abrupt jump from $\langle n \rangle = 0$ to $\langle n \rangle = 1$ at $\mu_c = 2.9375 \pm 0.0625$ is observed. This is another indication that the current chiral phase transition is of the first-order. The small shift of μ_c compared to the cases of chiral condensate and pressure is attributed to the definition of the numerical derivative in Eq. (7.18).
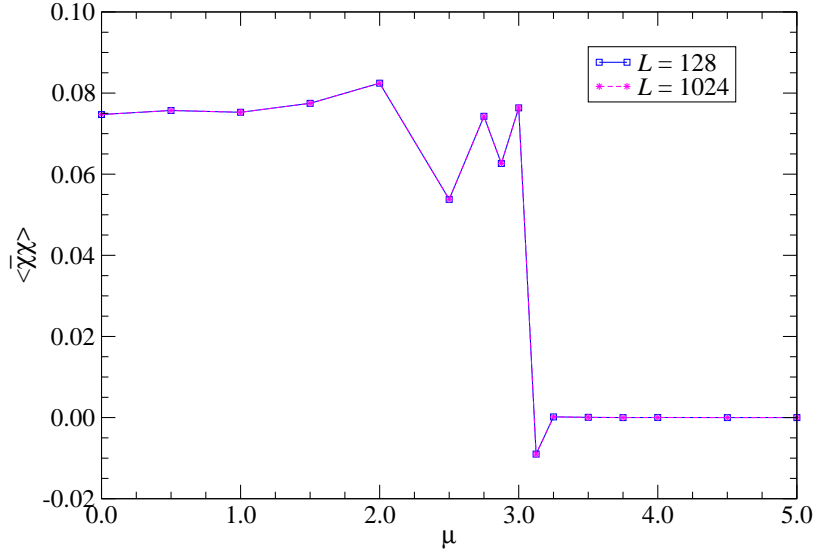
Figure 7.7: Chiral condensate extrapolated in the chiral limit as a function of μ with $D = 55$ on 128^4 and 1024^4 lattices.
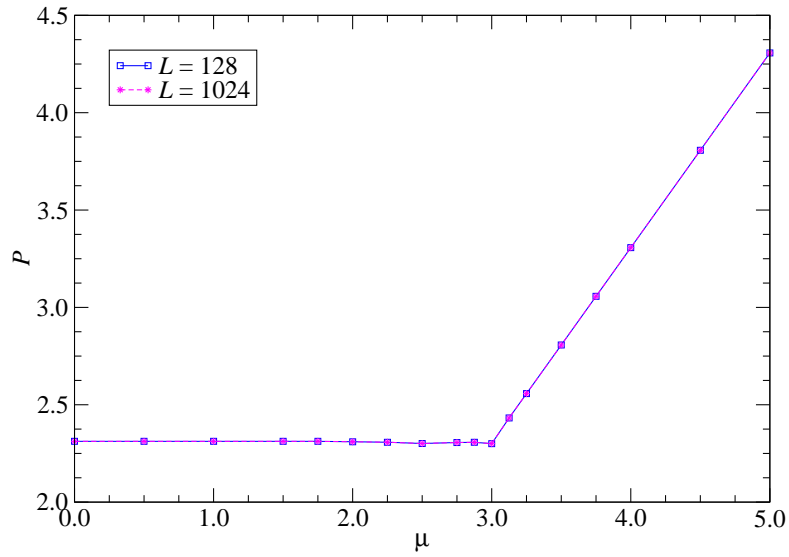
Figure 7.8: Pressure at $m = 0.01$ as a function of μ on 128^4 and 1024^4 lattices.
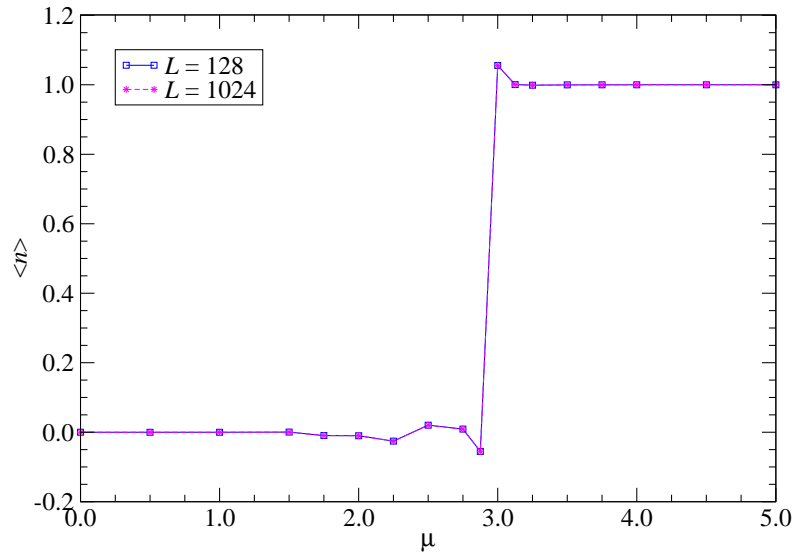
Figure 7.9: Particle number density at $m = 0.01$ as a function of μ on 128^4 and 1024^4 lattices.

8 Conclusion

We applied the TRG approach to the higher-dimensional lattice systems, including the spin model, relativistic scalar field theories, non-relativistic electrons, and relativistic lattice fermions. We demonstrated how to derive the tensor network representation for each case and showed that the efficiency of the TRG algorithms, such as the HOTRG and ATRG. The parallel computation in the higher-dimensional algorithms plays a significant role to enlarge the bond dimension, that is, to improve the accuracy of approximations based on the SVD.

The Ising model on a four-dimensional lattice was calculated by the parallelized HOTRG, which found the comparable transition point to the MC estimations, but with signals of the weak first-order phase transition. The possibility of the weak first-order phase transition in this model implies that the same phase transition may take place in the ϕ^4 theory, assuming the universality class. We then employed the ATRG with parallel computation to investigate the phase transition of the four-dimensional lattice ϕ^4 theory, where we indeed encountered the signal of the weak first-order phase transition. This result suggests that ϕ^4 theory on a four-dimensional lattice does not have the continuum limit. The TRG studies at finite density regimes in the complex ϕ^4 theory, the Hubbard models, and the NJL model suggest that the method does work in the systems accompanied by the sign problem, even in higher dimensions. In the study of the complex ϕ^4 theory in four dimensions, we used the parallelized ATRG, which successfully confirmed that the system exhibited the Silver Blaze phenomenon. The efficiency of the TRG approach for the lattice fermions was checked by benchmarking with the (1+1)-dimensional Hubbard model at finite density. The Grassmann HOTRG calculation nicely restored the exact solution based on the Bethe ansatz with the scaling with respect to the bond dimension. This work was followed by the Grassmann ATRG study of the (2+1)-dimensional Hubbard model at finite density, where the metal-insulator transition was observed over the vast regime of the Coulomb coupling. This result is consistent with recent quantum MC simulations. Finally, we applied the method to the NJL model at cold and dense regimes, where the serious sign problem takes place in the MC simulations. The parallelized Grassmann ATRG algorithm efficiently evaluated the staggered Grassmann tensor network with finite bond dimension and current numerical results showed that the chiral symmetry was restored in the cold and dense region with the first-order phase transition, as expected.

It can be said that remarkable progress of the TRG approach has been made in the recent few years. In particular, the higher-dimensional application has evolved dramatically, mainly because of the drastic cost reduction achieved by the ATRG algorithm [AOT20a] and the efficiency of the parallel computing in higher-dimensional TRGs [YS21, AKYY19, AKYY20]. The cost reduction of the TRG algorithm has been one of the hottest topics in this community [LE19, KN19, MK21, AOT20b, KOT21].

These applications must encourage us to investigate various higher-dimensional QFTs with the TRG approach in the future. One of the important research directions is to apply the method for the higher-dimensional systems with gauge interactions. This is currently in progress. Steady development has been made toward the TRG study of the QCD.

Acknowledgement

A   Subscript-swapping procedure with the RSVD

Suppose we want to know the truncated SVD of an $m \times n$ matrix A up to D. The idea of the RSVD can be sketched by

$$A \approx QQ^\dagger A = Q\tilde{U}\sigma V^\dagger, \tag{A.1}$$

where we are allowed to identify $U[A] = Q\tilde{U}$, $\sigma[A] = \sigma$, and $V^\dagger[A] = V^\dagger$. Q is an $m \times (D+p)$ matrix, whose columns are orthogonal. Considering the SVD of $Q^\dagger A$, instead of A itself, the RSVD is more economic than the usual SVD. p is an oversampling parameter. For the algorithmic details of RSVD, see Ref. [EVBK19], for example. The choice of Q is determined in the RSVD algorithm, which is explained below.
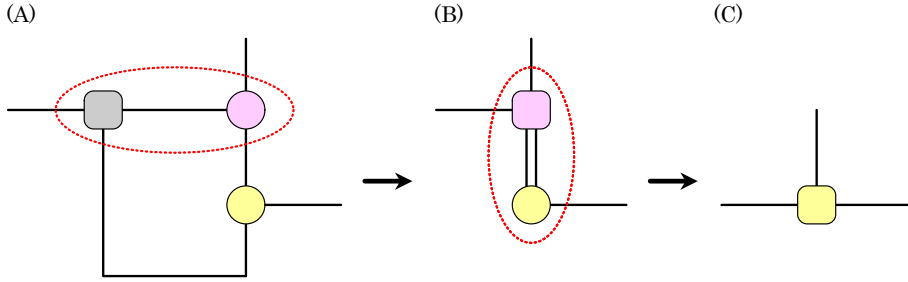
Figure A.1: Schematic pictures of the tensor contractions considered in the power iteration scheme. (A) One multiplies $R[\mathcal{B}]$ by Ω (or $Q[\Gamma]$) as in Eq. (A.2). (B) Multiplication of $R[\mathcal{C}]$ by $\tilde{\tilde{\Xi}}$ in Eq. (A.3). (C) One obtains Ξ.

Our goal is to obtain Eq. (2.47) without explicitly making $\mathcal{M}$, whose definition is Eq. (2.46). Firstly, we prepare a random matrix $\Omega_{\beta p, \delta}$, where the subscript δ runs up to $D + p$. Ω can be drawn from the normal distribution, the Gaussian distribution, or the other you want. Since it is important that the columns of such a random matrix will be linearly independent with high probability, the choice of Ω is not so essential. Then we consider the tensor contraction corresponding to $\mathcal{M}\Omega$ in the following steps,

$$\tilde{\tilde{\Xi}}_{i_1(n)\alpha\beta\delta} = \sum_p R[\mathcal{B}]_{i_1(n)\alpha,p}\Omega_{\beta p,\delta}, \tag{A.2}$$

$$\Xi_{\alpha q \delta} = \sum_{i_1(n),\beta} R[\mathcal{C}]_{i_1(n)\beta,q}\tilde{\tilde{\Xi}}_{i_1(n)\alpha\beta\delta}. \tag{A.3}$$

These steps are shown in Fig. A.1. Then the QR decomposition of Ξ, or $\mathcal{M}\Omega$, gives us

$$\Xi_{\alpha q\delta} = \sum_{\delta'} Q[\Xi]_{\alpha q,\delta'} R[\Xi]_{\delta,\delta'}. \tag{A.4}$$

Using the orthogonal matrix $Q[\Xi]$, we consider the tensor contraction corresponding to $\mathcal{M}^\dagger Q[\Xi]$ in the following steps,

$$\tilde{\Gamma}_{i_1(n)\beta\alpha\delta'} = \sum_q R[\mathcal{C}]^*_{i_1(n)\beta,q} Q[\Xi]_{\alpha q,\delta'}, \tag{A.5}$$

$$\Gamma_{\beta p\delta'} = \sum_{i_1(n),\alpha} R[\mathcal{B}]^*_{i_1(n)\alpha,p} \tilde{\Gamma}_{i_1(n)\beta\alpha\delta'}. \tag{A.6}$$

Again, the QR decomposition of Γ, or $\mathcal{M}^\dagger Q[\Xi]$, provides us with

$$\Gamma_{\beta p\delta'} = \sum_\delta Q[\Gamma]_{\beta p,\delta} R[\Xi]_{\delta',\delta}. \tag{A.7}$$

Now we can turn back to Eq. (A.2), replacing Ω by $Q[\Gamma]$. Repeating from Eq. (A.2) to Eq. (A.7), we can obtain a proper matrix Q, which is applied in the first step of Eq. (A.1). This is so-called power iteration scheme demonstrated in Ref. [MIZK18]. We denoted the iteration number of this scheme by q. The cost of the power iteration scheme scales with $\mathcal{O}(qD^{\min(d+3,6)})$. After the power iteration scheme, we carry out the tensor contraction in the following steps,

$$\tilde{\Theta}_{i_1(n)\beta\alpha\delta} = \sum_q R[\mathcal{C}]_{i_1(n)\beta,q} Q^*_{\alpha q,\delta}, \tag{A.8}$$

$$\Theta_{\delta\beta p} = \sum_{i_1(n),\alpha} R[\mathcal{B}]_{i_1(n)\alpha,p} \tilde{\Theta}_{i_1(n)\beta\alpha\delta}, \tag{A.9}$$

whose SVD is

$$\Theta_{\delta\beta p} = \sum_{\gamma=1}^{D+p} \tilde{U}_{\delta,\gamma} \sigma_\gamma V^*_{\beta p,\gamma}. \tag{A.10}$$

The matrices on the right-hand side are ingredients to reproduce the truncated SVD in Eq. (2.47) via

$$U[\mathcal{M}]_{\alpha q,\gamma} = \sum_{\delta=1}^{D+p} Q_{\alpha q,\delta} \tilde{U}_{\delta,\gamma}, \tag{A.11}$$

and $\sigma[\mathcal{M}]_\gamma = \sigma_\gamma$, $V^*[\mathcal{M}]_{\beta p,\gamma} = V^*_{\beta p,\gamma}$. At this stage, the subscript γ runs up to $D + p$, so γ is finally truncated up to D to restore Eq. (2.47).

B   Gauss quadrature rules

This appendix summarizes the several Gauss quadrature rules employed in this paper. [1]

B.1   Gauss-Hermite quadrature rule

This quadrature rule considers the approximation

$$\int_{-\infty}^{\infty} \mathrm{d}x \ \mathrm{e}^{-x^2} f(x) \approx \sum_{i=1}^{K} w_i f(x_i).$$

(B.1)

x_i denotes i-th root of the K-th Hermite polynomial $H_K(x)$. w_i is the associated weight defined via

$$w_i = \frac{2^{K-1} K! \sqrt{\pi}}{K^2 (H_{K-1}(x_i))^2}.$$

(B.2)

Fig. B.1 shows the weight w_i at the each node x_i, varying K.

B.2   Gauss-Laguerre quadrature rule

This quadrature rule considers the approximation

$$\int_{0}^{\infty} \mathrm{d}x \ \mathrm{e}^{-x} f(x) \approx \sum_{i=1}^{K} w_i f(x_i).$$

(B.3)

x_i denotes i-th root of the K-th Laguerre polynomial $L_K(x)$. w_i is the associated weight defined via

$$w_i = \frac{x_i}{(K+1)^2 (L_{K+1}(x_i))^2}.$$

(B.4)

Fig. B.2 shows the weight w_i at the each node x_i, varying K.

B.3   Gauss-Legendre quadrature rule

This quadrature rule considers the approximation

$$\int_{-1}^{1} \mathrm{d}x f(x) \approx \sum_{i=1}^{K} w_i f(x_i).$$

(B.5)

x_i denotes i-th root of the K-th Legendre polynomial $P_K(x)$. w_i is the associated weight defined via

$$w_i = \frac{2}{(1-x_i^2)(P_K'(x_i))^2}.$$

(B.6)

Fig. B.3 shows the weight w_i at the each node x_i, varying K.

---

[1] The construction of tensor networks based on the Gauss quadrature rule is explained from the viewpoint of a modified harmonic-oscillator algebra in §9.1 of Ref. [Meu21].
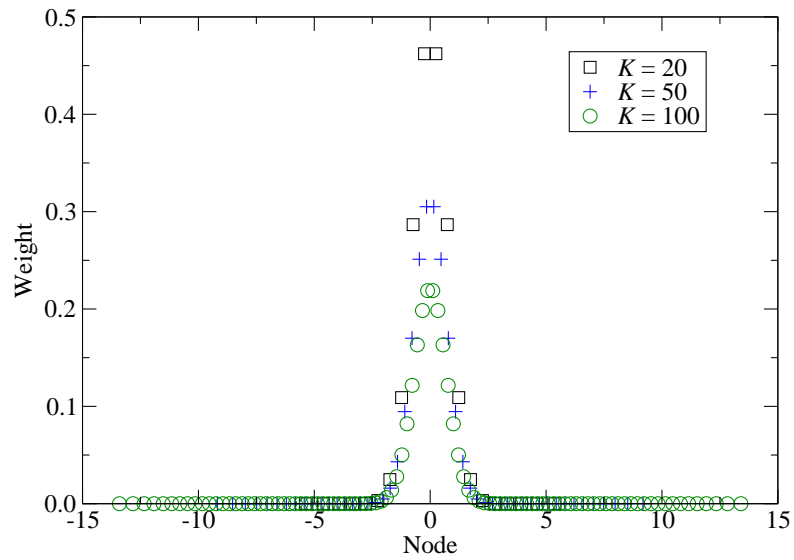
Figure B.1: Weight at each node in the Gauss-Hermite quadrature rule varying the regularization parameter K.
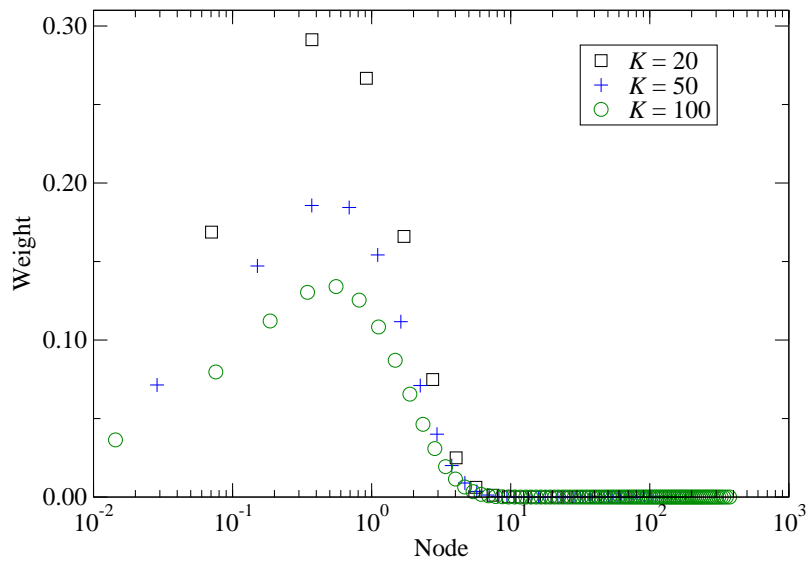
Figure B.2: Weight at each node in the Gauss-Laguerre quadrature rule varying the regularization parameter K.
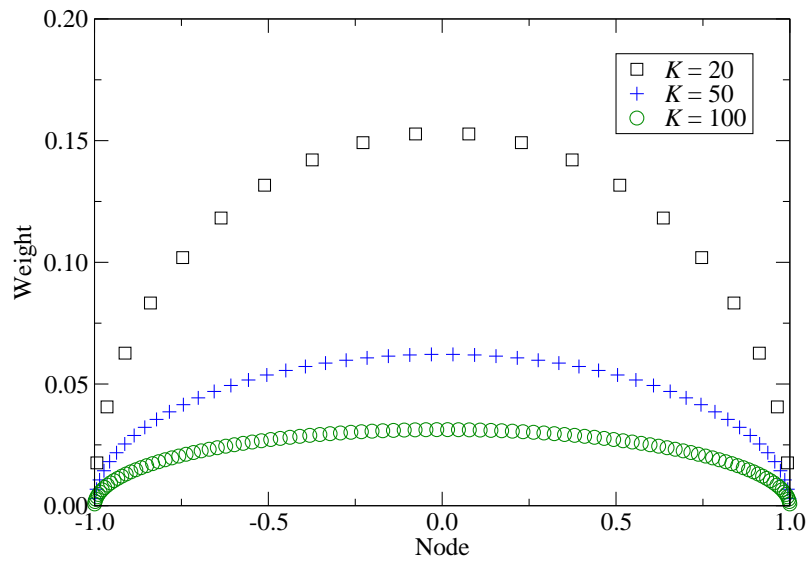
Figure B.3: Weight at each node in the Gauss-Legendre quadrature rule varying the regularization parameter K.

C   Relation between the staggered fermion and the Dirac fermion

We assume that a linear lattice size N_ν satisfies $N_\nu \in 2\mathbb{Z}$ for all ν. Firstly, we group together the 2^4 sites in the lattice Λ_{3+1}, where $|\Lambda_{3+1}| = N_1 N_2 N_3 N_4$, and regard them as a block site in new lattice Λ'_{3+1}. $n_\nu \in \Lambda_{3+1}$ is translated into $h_\nu \in \Lambda'_{3+1}$ as

$$n_\nu = 2h_\nu + s_\nu. \tag{C.1}$$

When $n_\nu = 0, 1, \cdots, N_\nu - 1$,

$$h_\nu = 0, 1, \cdots, \frac{N_\nu}{2} - 1 \tag{C.2}$$

and

$$s_\nu = 0, 1. \tag{C.3}$$

In other words, $s_\nu = n_\nu \mod 2$. Thanks to this identification, we have

$$\eta_\nu(n) = \eta_\nu(2h + s) = \eta_\nu(s) \tag{C.4}$$

for all ν. Our aim is to identify the staggered fermions $\chi(n)$ and $\bar{\chi}(n)$ live in Λ_{3+1} with the four-component Dirac fermions $\psi^{(t)}(h)$ and $\bar{\psi}^{(t)}(h)$, where t labels the fermion species of the resulting Dirac fermions. Let us define the s-dependent staggered transformation $\Gamma^{(s)}$ as follows,

$$\Gamma^{(s)} = \gamma_1^{s_1} \gamma_2^{s_2} \gamma_3^{s_3} \gamma_4^{s_4}. \tag{C.5}$$

Before discussing some identities for $\Gamma^{(s)}$, we quickly review the Fierz transformation. When we have the complete linear system spanned by $\{|e_\mu\rangle\}$, where $|e_\mu\rangle$ is an n-dimensional vector and satisfies

$$\langle e_\mu | e_\nu \rangle = \delta_{\mu\nu}, \tag{C.6}$$

any n-dimensional vector $|c\rangle$ can be expanded in this basis as

$$|c\rangle = \left(\sum_\mu |e_\mu\rangle \langle e_\mu| \right) |c\rangle = \sum_\mu |e_\mu\rangle \langle e_\mu | c \rangle. \tag{C.7}$$

Similar relation also holds in the system spanned by matrices. Suppose we have the complete orthogonal system $\{\lambda_\mu\}$ spanned by $n \times n$ matrices satisfying

$$\text{Tr}[\lambda_\mu^\dagger \lambda_\nu] = N \delta_{\mu\nu}. \tag{C.8}$$

Then any $n \times n$ matrix Γ is expanded in this system as

$$\Gamma = \frac{1}{N} \sum_\mu \lambda_\mu \text{Tr}[\lambda_\mu^\dagger \Gamma]. \tag{C.9}$$

Now, for any $n \times n$ matrices Λ^1 and Λ^2, we set

$$\Gamma_{il}^{(jk)} = \Lambda_{ij}^1 \Lambda_{kl}^2 \tag{C.10}$$

and we regard $\Gamma^{(jk)}_{il}$ as a component of the matrix $\Gamma^{(jk)}$. We expand $\Gamma^{(jk)}$ as

$$\Gamma^{(jk)}_{il} = \frac{1}{N}\sum_\mu (\lambda_\mu)_{il}\mathrm{Tr}[\lambda^\dagger_\mu \Gamma^{(jk)}] = \frac{1}{N}\sum_\mu (\lambda_\mu)_{il}(\Lambda^2\lambda^\dagger_\mu\Lambda^1)_{kj}, \tag{C.11}$$

that is,

$$\Lambda^1_{ij}\Lambda^2_{kl} = \frac{1}{N}\sum_\mu (\lambda_\mu)_{il}(\Lambda^2\lambda^\dagger_\mu\Lambda^1)_{kj} \tag{C.12}$$

holds. Finally, we find the Fierz transformation,

$$(\bar\psi_1\Lambda^1\psi_2)(\bar\psi_3\Lambda^2\psi_4) = \frac{1}{N}\sum_\mu (\bar\psi_1\lambda_\mu\psi_4)(\bar\psi_3\Lambda^1\lambda^\dagger_\mu\Lambda^2\psi_2), \tag{C.13}$$

where ψ_i and $\bar\psi_j$ are n-dimensional vectors. We now come back to the staggered transformation $\Gamma^{(s)}$ defined in Eq. (C.5). $\Gamma^{(s)}$ satisfies the completeness relation Eq. (C.8) in the following sense,

$$\mathrm{Tr}[\Gamma^{(s)\dagger}\Gamma^{(s')}] = 4\delta_{ss'}. \tag{C.14}$$

The above relation holds because for the Euclidean γ-matrix, $\gamma^\dagger_\mu = \gamma_\mu = \gamma^{-1}_\mu$ follows. Hence, the Fierz transformation gives us

$$\delta_{ab}\delta_{cd} = \frac{1}{4}\sum_s \Gamma^{(s)}_{ad}\sum_{m,n}\delta_{cm}\Gamma^{(s)\dagger}_{mn}\delta_{nb} = \frac{1}{4}\sum_s \Gamma^{(s)}_{ad}\Gamma^{(s)*}_{bc}. \tag{C.15}$$

Then, we introduce the following linear combinations of the staggered fermions,

$$q(h)_{ab} = \frac{1}{8}\sum_s \Gamma^{(s)}_{ab}\chi(2h+s), \tag{C.16}$$

$$\bar q(h)_{ab} = \frac{1}{8}\sum_s \bar\chi(2h+s)\Gamma^{(s)*}_{ba}. \tag{C.17}$$

Using Eq. (C.14), we obtain the inverse staggered transformation,

$$2\mathrm{Tr}[\Gamma^{(s)\dagger}q(h)] = 2\sum_{a,b}\Gamma^{(s)*}_{ab}q(h)_{ab} = \frac{1}{4}\sum_{s'}\sum_{a,b}\Gamma^{(s)*}_{ab}\Gamma^{(s')}_{ab}\chi(2h+s') = \chi(2h+s), \tag{C.18}$$

$$2\mathrm{Tr}[\bar q(h)\Gamma^{(s)}] = 2\sum_{a,b}\bar q(h)_{ab}\Gamma^{(s)}_{ba} = \frac{1}{4}\sum_{s'}\sum_{a,b}\bar\chi(2h+s')\Gamma^{(s')*}_{ba}\Gamma^{(s)}_{ba} = \bar\chi(2h+s). \tag{C.19}$$

It is ready to apply the staggered transformation for Eq. (7.2). Setting the lattice spacing for Λ_{3+1} as a, that for Λ'_{3+1} as $b = 2a$. For the free staggered fermions, Eq. (7.2) becomes

$$S = a^4\sum_{n\in\Lambda_{3+1}}\bar\chi(n)\left[\sum_{\nu=1}^4 \eta_\nu(n)\frac{\mathrm{e}^{\mu a\delta_{\nu,4}}\chi(n+\hat\nu) - \mathrm{e}^{-\mu a\delta_{\nu,4}}\chi(n-\hat\nu)}{2a} + m_0\chi(n)\right]. \tag{C.20}$$

For the mass term, we have

$$a^4 \sum_{n\in\Lambda_{3+1}} \bar{\chi}(n)\chi(n) = 4a^4 \sum_{h\in\Lambda'_{3+1}} \sum_{a,b,c,d} \sum_{s} \bar{q}(h)_{ab}\Gamma^{(s)}_{ba}\Gamma^{(s)*}_{cd}q(h)_{cd}$$

$$= (2a)^4 \sum_{h\in\Lambda'_{3+1}} \sum_{a,b,c,d} \bar{q}(h)_{ab}q(h)_{cd}\delta_{bc}\delta_{da}$$

$$= b^4 \sum_{h\in\Lambda'_{3+1}} \mathrm{Tr}[\bar{q}(h)q(h)]. \tag{C.21}$$

For the hopping terms, we need to pay a little attention, because the hopping in the lattice Λ_{3+1} is interpreted in two ways in Λ'_{3+1}. One is the hopping inside the block site and the other is the hopping between two block sites. So,

$$\chi(2h+s+\hat{\nu}) = \begin{cases} \chi(2h+s+\hat{\nu}) & = 2\mathrm{Tr}[\Gamma^{(s+\hat{\nu})\dagger}q(h)] \\ \chi(2(h+\hat{\nu})+s-\hat{\nu}) & = 2\mathrm{Tr}[\Gamma^{(s-\hat{\nu})\dagger}q(h+\hat{\nu})], \end{cases} \tag{C.22}$$

or equivalently,

$$\chi(2h+s+\hat{\nu}) = 2\sum_{s'}\left[\delta_{s+\hat{\nu},s'}\mathrm{Tr}[\Gamma^{(s')\dagger}q(h)] + \delta_{s-\hat{\nu},s'}\mathrm{Tr}[\Gamma^{(s')\dagger}q(h+\hat{\nu})]\right] \tag{C.23}$$

holds. We have to remember that in Eq. (C.23) the first term corresponds to the hopping inside the block site h, so $s_\nu = 0$ is necessary, otherwise $s+\hat{\nu}$ does not stay in the same block site h. Similarly, the second term corresponds to the hopping between h and $h+\hat{\nu}$, so $s_\nu = 1$ is necessary. [1] Thus, Eq. (C.23) should be understood explicitly as

$$\chi(2h+s+\hat{\nu}) = 2\sum_{s'}\left[\delta_{s_\nu,0}\delta_{s+\hat{\nu},s'}\mathrm{Tr}[\Gamma^{(s')\dagger}q(h)] + \delta_{s_\nu,1}\delta_{s-\hat{\nu},s'}\mathrm{Tr}[\Gamma^{(s')\dagger}q(h+\hat{\nu})]\right]. \tag{C.24}$$

The similar consideration specifies

$$\chi(2h+s-\hat{\nu}) = 2\sum_{s'}\left[\delta_{s_\nu,1}\delta_{s-\hat{\nu},s'}\mathrm{Tr}[\Gamma^{(s')\dagger}q(h)] + \delta_{s_\nu,0}\delta_{s+\hat{\nu},s'}\mathrm{Tr}[\Gamma^{(s')\dagger}q(h-\hat{\nu})]\right]. \tag{C.25}$$

Therefore,

$$a^4 \sum_{n\in\Lambda_{3+1}} \bar{\chi}(n)\frac{1}{2a}\sum_\nu \eta_\nu(n)\left[\mathrm{e}^{\mu a\delta_{\nu,4}}\chi(n+\hat{\nu}) - \mathrm{e}^{-\mu a\delta_{\nu,4}}\chi(n-\hat{\nu})\right]$$

$$= 4a^4 \sum_{h\in\Lambda'_{3+1}} \sum_\nu \frac{1}{2a}\sum_{s,s'} \mathrm{Tr}[\bar{q}(h)\Gamma^{(s)}]\eta_\nu(s)$$

$$\times \left[\mathrm{e}^{\mu a\delta_{\nu,4}}\left\{\delta_{s_\nu,0}\delta_{s+\hat{\nu},s'}\mathrm{Tr}[\Gamma^{(s')\dagger}q(h)] + \delta_{s_\nu,1}\delta_{s-\hat{\nu},s'}\mathrm{Tr}[\Gamma^{(s')\dagger}q(h+\hat{\nu})]\right\}\right.$$

$$\left. -\mathrm{e}^{-\mu a\delta_{\nu,4}}\left\{\delta_{s_\nu,1}\delta_{s-\hat{\nu},s'}\mathrm{Tr}[\Gamma^{(s')\dagger}q(h)] + \delta_{s_\nu,0}\delta_{s+\hat{\nu},s'}\mathrm{Tr}[\Gamma^{(s')\dagger}q(h-\hat{\nu})]\right\}\right]$$

$$= 4a^4 \sum_{h\in\Lambda'_{3+1}} \sum_\nu \sum_{s,s'} \mathrm{Tr}[\bar{q}(h)\Gamma^{(s)}]\eta_\nu(s)\left\{\frac{1}{2a}(\delta_{s_\nu,0}\delta_{s+\hat{\nu},s'} + \delta_{s_\nu,1}\delta_{s-\hat{\nu},s'})\sinh(\mu' b\delta_{\nu,4})\right.$$

$$\left. + (\delta_{s_\nu,0}\delta_{s+\hat{\nu},s'} + \delta_{s_\nu,1}\delta_{s-\hat{\nu},s'})\nabla_\nu(\mu') - a(\delta_{s_\nu,0}\delta_{s+\hat{\nu},s'} - \delta_{s_\nu,1}\delta_{s-\hat{\nu},s'})\Delta_\nu(\mu')\right\}\mathrm{Tr}[\Gamma^{(s')\dagger}q(h)] \tag{C.26}$$

---

[1] In the original lattice Λ_{3+1}, $n_\nu \mod 2 = s_\nu$ and the sites satisfying $s_\nu = 0$ is usually called even sites and those with $s_\nu = 1$ is called odd sites.

where $\nabla_\nu(\mu')$ and $\Delta_\nu(\mu')$ are the differential operators with the chemical potential μ' on the lattice Λ'_{3+1}, whose lattice spacing is $b = 2a$, defined by

$$\nabla_\nu(\mu')f(h) = \frac{\mathrm{e}^{\mu'b\delta_{\nu,4}}f(h+\hat{\nu}) - \mathrm{e}^{-\mu'b\delta_{\nu,4}}f(h-\hat{\nu})}{2b}, \tag{C.27}$$

$$\Delta_\nu(\mu')f(h) = \frac{\mathrm{e}^{\mu'b\delta_{\nu,4}}f(h+\hat{\nu}) - \mathrm{e}^{\mu'b\delta_{\nu,4}}f(h) - \mathrm{e}^{-\mu'b\delta_{\nu,4}}f(h) + \mathrm{e}^{-\mu'b\delta_{\nu,4}}f(h-\hat{\nu})}{b^2}. \tag{C.28}$$

μ' is defined by

$$\mu'b = \mu a \Longleftrightarrow \mu' = \frac{\mu}{2} \tag{C.29}$$

Now, we are ready to carry out the summation over s and s'. Since

$$\Gamma^{(s\pm\hat{\nu})} = \eta_\nu(s)\gamma_\nu\Gamma^{(s)}, \tag{C.30}$$

we find that

$$\sum_{s,s'}\mathrm{Tr}[\bar{q}(h)\Gamma^{(s)}]\eta_\nu(s)(\delta_{s_\nu,0}\delta_{s+\hat{\nu},s'} + \delta_{s_\nu,1}\delta_{s-\hat{\nu},s'})\sinh(\mu'b\delta_{\nu,4})\mathrm{Tr}[\Gamma^{(s')\dagger}q(h)]$$

$$= \sum_{a,b,c,d}\sum_s \bar{q}(h)_{ab}\Gamma^{(s)}_{ba}(\delta_{s_\nu,0} + \delta_{s_\nu,1})(\gamma_\nu\Gamma^{(s)})^\dagger_{cd}\sinh(\mu'b\delta_{\nu,4})q(h)_{dc}$$

$$= \sum_{a,b,c,d,e}\sum_s \bar{q}(h)_{ab}\Gamma^{(s)}_{ba}\Gamma^{(s)*}_{ec}(\gamma_\nu)_{ed}q(h)_{dc}$$

$$= 4\mathrm{Tr}[\bar{q}(h)\gamma_\nu\sinh(\mu'b\delta_{\nu,4})(\mu')q(h)] \tag{C.31}$$

and

$$\sum_{s,s'}\mathrm{Tr}[\bar{q}(h)\Gamma^{(s)}]\eta_\nu(s)(\delta_{s_\nu,0}\delta_{s+\hat{\nu},s'} + \delta_{s_\nu,1}\delta_{s-\hat{\nu},s'})\nabla_\nu(\mu')\mathrm{Tr}[\Gamma^{(s')\dagger}q(h)]$$

$$= \sum_{a,b,c,d}\sum_s \bar{q}(h)_{ab}\Gamma^{(s)}_{ba}(\delta_{s_\nu,0} + \delta_{s_\nu,1})(\gamma_\nu\Gamma^{(s)})^\dagger_{cd}\nabla_\nu(\mu')q(h)_{dc}$$

$$= \sum_{a,b,c,d,e}\sum_s \bar{q}(h)_{ab}\Gamma^{(s)}_{ba}\Gamma^{(s)*}_{ec}(\gamma_\nu)_{ed}\nabla_\nu(\mu')q(h)_{dc}$$

$$= 4\mathrm{Tr}[\bar{q}(h)\gamma_\nu\nabla_\nu(\mu')q(h)]. \tag{C.32}$$

We have used the expansion by the indicator function,

$$\sum_{s_\nu=0}^{1} f(s_\nu) = f(0) + f(1) = \sum_{s_\nu=0}^{1}[\delta_{s_\nu,0}f(s_\nu) + \delta_{s_\nu,1}f(s_\nu)] \tag{C.33}$$

The remaining term we have to evaluate is

$$\sum_{s,s'}\mathrm{Tr}[\bar{q}(h)\Gamma^{(s)}]\eta_\nu(s)(\delta_{s_\nu,0}\delta_{s+\hat{\nu},s'} - \delta_{s_\nu,1}\delta_{s-\hat{\nu},s'})\Delta_\nu(\mu')\mathrm{Tr}[\Gamma^{(s')\dagger}q(h)]. \tag{C.34}$$

Unfortunately, we cannot directly apply the expansion like in Eq. (C.33) because of the negative sign in the middle parentheses. So we employ the following γ-algebra; if $\rho \neq \sigma$,

$$\gamma_\rho^{s_\rho} \gamma_\sigma = (-1)^{s_\rho} \gamma_\sigma \gamma_\rho^{s_\rho}, \tag{C.35}$$

and if $\rho = \sigma$,

$$\gamma_\rho^{s_\rho} \gamma_\sigma = \gamma_\sigma \gamma_\rho^{s_\rho} = (-1)^{s_\rho}(-1)^{s_\rho} \gamma_\sigma \gamma_\rho^{s_\rho}, \tag{C.36}$$

hold, obviously. Hence, we result in

$$\gamma_\nu \Gamma^{(s)} = (-1)^{s_\nu} \eta_5(s) \Gamma^{(s)} \gamma_\nu. \tag{C.37}$$

Moreover,

$$\gamma_5 \Gamma^{(s)} = \eta_5(s) \Gamma^{(s)} \gamma_5 \iff \eta_5(s) \Gamma^{(s)} = \gamma_5 \Gamma^{(s)} \gamma_5 \tag{C.38}$$

holds. Applying Eqs. (C.30), (C.37) and (C.38) to Eq. (C.34), we find

$$\begin{aligned}
&\sum_{s,s'} \text{Tr}[\bar{q}(h)\Gamma^{(s)}]\eta_\nu(s)(\delta_{s_\nu,0}\delta_{s+\hat{\nu},s'} - \delta_{s_\nu,1}\delta_{s-\hat{\nu},s'})\Delta_\nu(\mu')\text{Tr}[\Gamma^{(s')\dagger}q(h)] \\
&= \sum_{a,b,c,d} \sum_s \bar{q}(h)_{ab}\Gamma_{ba}^{(s)}(\delta_{s_\nu,0} - \delta_{s_\nu,1})(\gamma_\nu\Gamma^{(s)})_{cd}^\dagger \Delta_\nu(\mu')q(h)_{dc} \\
&= \sum_{a,b,c,d} \sum_s \bar{q}(h)_{ab}\Gamma_{ba}^{(s)}[\delta_{s_\nu,0}(-1)^{s_\nu} - \delta_{s_\nu,1}(-1)^{s_\nu}](\eta_5(s)\Gamma^{(s)}\gamma_\nu)_{cd}^\dagger \Delta_\nu(\mu')q(h)_{dc} \\
&= \sum_{a,b,c,d,e,f,g} \sum_s \bar{q}(h)_{ab}\Gamma_{ba}^{(s)}[\delta_{s_\nu,0} + \delta_{s_\nu,1}](\gamma_\nu)_{ce}(\gamma_5)_{ef}\Gamma_{gf}^{(s)*}(\gamma_5)_{gd}\Delta_\nu(\mu')q(h)_{dc} \\
&= \sum_{a,b,c,d,e,f,g} \sum_s \bar{q}(h)_{ab}\Gamma_{ba}^{(s)}(\gamma_\nu)_{ce}(\gamma_5)_{ef}\Gamma_{gf}^{(s)*}(\gamma_5)_{gd}\Delta_\nu(\mu')q(h)_{dc} \\
&= 4\text{Tr}[\bar{q}(h)\gamma_5\Delta_\nu(\mu')q(h)\gamma_\nu\gamma_5].
\end{aligned} \tag{C.39}$$

Therefore, free staggered action (C.20) is now transformed as

$$\begin{aligned}
S = b^4 \sum_{h\in\Lambda'_{3+1}} &\left[m_0\text{Tr}[\bar{q}(h)q(h)] + \sum_\nu \text{Tr}[\bar{q}(h)\gamma_\nu\left\{\nabla_\nu(\mu') + \frac{1}{b}\sinh(\mu'b\delta_{\nu,4})\right\}q(h)] \right. \\
&\left. - \frac{b}{2}\sum_\nu \text{Tr}[\bar{q}(h)\gamma_5\Delta_\nu(\mu')q(h)\gamma_\nu\gamma_5] \right].
\end{aligned} \tag{C.40}$$

Identifying the Dirac indices α and quark species labels t for $q(h)$ and $\bar{q}(h)$ by setting

$$\psi^{(t)}(h)_\alpha = q(h)_{\alpha t}, \quad \bar{\psi}^{(t)}(h)_\alpha = \bar{q}(h)_{t\alpha}, \tag{C.41}$$

Eq (C.40) reads

$$\begin{aligned}
S = b^4 \sum_{h\in\Lambda'_{3+1}} &\left[\sum_{t=1}^4 \left(m_0\bar{\psi}^{(t)}(h)\psi^{(t)}(h) + \sum_\nu \bar{\psi}^{(t)}(h)\gamma_\nu\left\{\nabla_\nu(\mu') + \frac{1}{b}\sinh(\mu'b\delta_{\nu,4})\right\}\psi^{(t)}(h) \right) \right. \\
&\left. - \frac{b}{2}\sum_\nu \sum_{t,t'=1}^4 \bar{\psi}^{(t)}(h)\gamma_5\Delta_\nu(\mu')\psi^{(t')}(h)(\gamma_\nu\gamma_5)_{tt'} \right],
\end{aligned} \tag{C.42}$$

or, introducing the direct product of the groups describing the symmetry of chirality and flavor,

$$SU(4) \otimes SU(4) = \{\gamma_\nu \otimes \tau_\nu | \gamma_\nu \in SU(4), \tau_\nu \in SU(4)\}, \tag{C.43}$$

where $\tau_\nu = \gamma_\nu^* = \gamma_\nu^{\mathrm{T}}$,

$$S = b^4 \sum_{h \in \Lambda'_{3+1}} \left[m_0 \bar{\psi}(h) \mathbb{1} \otimes \mathbb{1} \psi(h) + \sum_\nu \bar{\psi}(h) \gamma_\nu \otimes \mathbb{1} \left\{ \nabla_\nu(\mu') + \frac{1}{b} \sinh(\mu' b \delta_{\nu,4}) \right\} \psi(h) \right.$$
$$\left. - \frac{b}{2} \sum_\nu \bar{\psi}(h) \gamma_5 \otimes \tau_\nu \tau_5 \Delta_\nu(\mu') \psi(h) \right]. \tag{C.44}$$

Consequently, the staggered fermions can be regarded as the four-flavor Dirac fermions, whose chiral and flavor symmetry is broken. The above action tells us that this symmetry breaking is caused by the lattice artifact with $\mathcal{O}(a)$. Notice that $SU(4) \otimes SU(4)$ symmetry is not totally broken, because for $\forall \alpha, \beta \in \mathbb{R}$, Eq. (C.44) is invariant under the transformations,

$$\psi'(h) = \mathrm{e}^{\mathrm{i}\alpha} \psi(h), \quad \bar{\psi}'(h) = \bar{\psi}(h) \mathrm{e}^{-\mathrm{i}\alpha},$$
$$\psi'(h) = \mathrm{e}^{\mathrm{i}\beta\gamma_5 \otimes \tau_5} \psi(h), \quad \bar{\psi}'(h) = \bar{\psi}(h) \mathrm{e}^{-\mathrm{i}\beta\gamma_5 \otimes \tau_5},$$

that is, we can again see that staggered fermions are of chiral symmetry, regarding them as four-flavor Dirac fermions. If one seems that our discussion to introduce the flavor basis for the staggered fermions is somewhat *ad hoc*, refer §4.3.3 in Ref. [MM97], for instance. Note that the above transformation from the staggered fermion to the Dirac fermion allows us to exactly evaluate the path integral of the free field theory. This is explained in Appendix. D.

D   Exact solution of the free staggered fermion theory on $(3+1)$-dimensional finite lattice

When there is no interaction between staggered fermions, it is possible to obtain the exact value of Eq. (7.6), rewriting the action of the free staggered fermions to that with the Dirac fermions. Assuming $|\Lambda'_{3+1}| = \tilde{N}_1\tilde{N}_2\tilde{N}_3\tilde{N}_4$, the Dirac fermions are expanded in momentum basis,

$$\psi^{(t)}(h) = \sum_k \exp\left[\sum_\nu \frac{2\pi\mathrm{i}k_\nu h_\nu b}{\tilde{N}_\nu}\right]\phi_k^{(t)}, \tag{D.1}$$

$$\bar{\psi}^{(t)}(h) = \sum_k \exp\left[-\sum_\nu \frac{2\pi\mathrm{i}k_\nu h_\nu b}{\tilde{N}_\nu}\right]\bar{\phi}_k^{(t)}. \tag{D.2}$$

In the following, we use the chiral representation for the γ-matrix,

$$\gamma_{1,2,3} = \begin{bmatrix} 0 & -\mathrm{i}\sigma_{1,2,3} \\ \mathrm{i}\sigma_{1,2,3} & 0 \end{bmatrix}, \quad \gamma_4 = \begin{bmatrix} 0 & \mathbb{1} \\ \mathbb{1} & 0 \end{bmatrix}, \quad \gamma_5 = \begin{bmatrix} \mathbb{1} & 0 \\ 0 & -\mathbb{1} \end{bmatrix}. \tag{D.3}$$

The mass term is transformed as

$$m_0 \sum_h \sum_t \bar{\psi}^{(t)}(h)\psi^{(t)}(h) = m_0 \sum_k \sum_t \bar{\phi}_k^{(t)}\phi_k^{(t)} \tag{D.4}$$

and the rest of flavor diagonal term is

$$\sum_h \sum_t \sum_\nu \bar{\psi}^{(t)}(h)\gamma_\nu \left\{\nabla_\nu(\mu') + \frac{1}{b}\sinh(\mu'b\delta_{\nu,4})\right\}\psi^{(t)}(h)$$
$$= \frac{1}{b}\sum_k \sum_t \sum_\nu \left[\mathrm{i}\sin\left(\frac{2\pi k_\nu b}{\tilde{N}_\nu} - \mathrm{i}\mu'b\delta_{\nu,4}\right) + \sinh(\mu'b\delta_{\nu,4})\right]\bar{\phi}_k^{(t)}\gamma_\nu\phi_k^{(t)}. \tag{D.5}$$

For the chiral-flavor symmetry breaking term,

$$-\frac{b}{2}\sum_h \sum_{t,t'} \sum_\nu \bar{\psi}^{(t)}(h)\gamma_5\Delta_\nu(\mu')\psi^{(t')}(h)(\gamma_\nu\gamma_5)_{tt'}$$
$$= -\frac{1}{b}\sum_k \sum_{t,t'} \sum_\nu \left[\cos\left(\frac{2\pi k_\nu b}{\tilde{N}_\nu} - \mathrm{i}\mu'b\delta_{\nu,4}\right) - \cosh\left(\mu'b\delta_{\nu,4}\right)\right]\bar{\phi}_k^{(t)}\gamma_5\phi_k^{(t')}(\gamma_\nu\gamma_5)_{tt'}. \tag{D.6}$$

Then the path integral is given by

$$Z = \left(\prod_h \prod_t \prod_\alpha \int\int \mathrm{d}\psi_\alpha^{(t)}(h)\mathrm{d}\bar{\psi}_\alpha^{(t)}(h)\right)\mathrm{e}^{-S}$$
$$= \left(\prod_k \prod_t \prod_\alpha \int\int \mathrm{d}\phi_{\alpha,k}^{(t)}\mathrm{d}\bar{\phi}_{\alpha,k}^{(t)}\right)\mathrm{e}^{-S_k}, \tag{D.7}$$

so we need to carry out the Grassmann integration,

$$\left(\prod_t \prod_\alpha \int\int \mathrm{d}\phi_\alpha^{(t)}\mathrm{d}\bar{\phi}_\alpha^{(t)}\right)\exp\left[\sum_{t,t'} \sum_{\alpha,\beta} \bar{\phi}_\alpha^{(t)}M_{\alpha\beta}^{tt'}\phi_\beta^{(t')}\right], \tag{D.8}$$

setting

$$M_{\alpha\beta}^{tt'}(k) = -m_0\delta_{tt'}\delta_{\alpha\beta} - \frac{1}{b}\sum_\nu \left[\mathrm{i}\sin\left(\frac{2\pi(k_\nu b+\theta_\nu)}{\tilde{N}_\nu} - \mathrm{i}\frac{\mu}{2}b\delta_{\nu,4}\right) + \sinh\left(\frac{\mu}{2}b\delta_{\nu,4}\right) \right] \delta_{tt'}(\gamma_\nu)_{\alpha\beta}$$

$$+ \frac{1}{b}\sum_\nu \left[\cos\left(\frac{2\pi(k_\nu b+\theta_\nu)}{\tilde{N}_\nu} - \mathrm{i}\frac{\mu}{2}b\delta_{\nu,4}\right) - \cosh\left(\frac{\mu}{2}b\delta_{\nu,4}\right) \right] (\gamma_\nu\gamma_5)_{tt'}(\gamma_5)_{\alpha\beta}, \qquad \text{(D.9)}$$

where $k_\nu = 1, 2, \cdots, \tilde{N}_\nu$ and θ_ν describes the boundary condition in the $\hat{\nu}$-direction. In the current formalism, we set $\theta_1 = \theta_2 = \theta_3 = 0$ and $\theta_4 = 1/2$. Now we can directly calculate

$$Z = \prod_k \det M(k). \qquad \text{(D.10)}$$

The volume V of the lattice Λ'_{3+1} is equal to Λ_{3+1}, that is,

$$V = N_1 N_2 N_3 N_4 = 2^4 \tilde{N}_1 \tilde{N}_2 \tilde{N}_3 \tilde{N}_4. \qquad \text{(D.11)}$$

The thermodynamic potential and the number density exhibit the μ dependence shown in Fig. D.1 and Fig. D.2, where we consider an isotropic lattice whose linear size is denoted by L $(= N_\nu, \ \forall\nu)$.
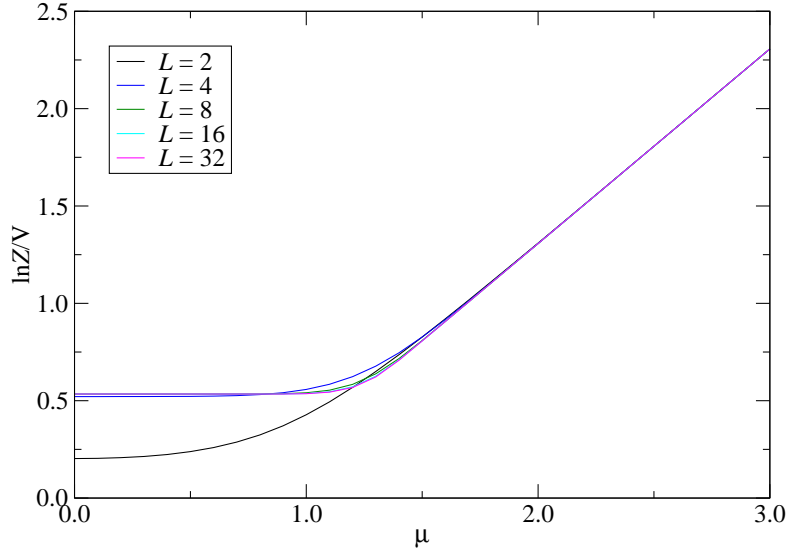
Figure D.1: Pressure against the chemical potential μ with $m_0 = 1$.

To calculate the matrix determinant, the eigenvalue decomposition is helpful, because for an $n \times n$ matrix A, its determinant is given by

$$\det A = \det U^\dagger D U = \det D = \prod_{i=1}^n \lambda_i,$$
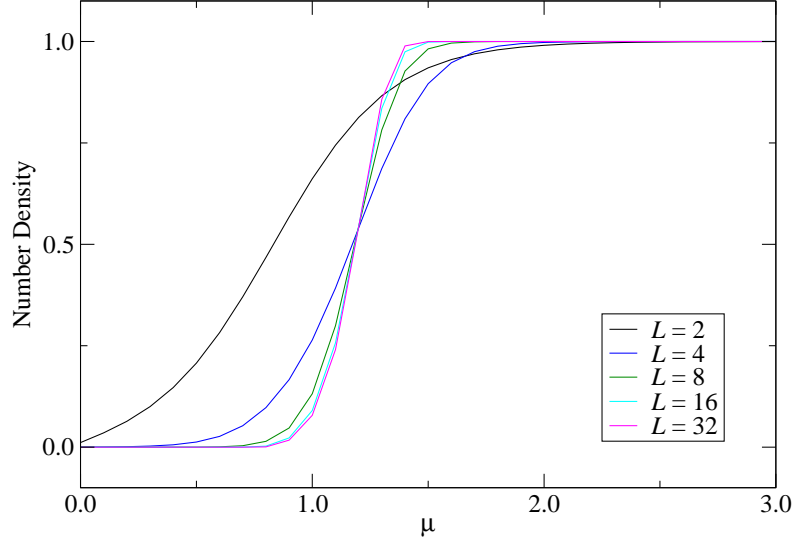
Figure D.2: Number density as a function of μ with $m_0 = 1$.

where λ_i is the ith eigenvalue of A. Another efficient way to obtain $\det A$ is the LU decomposition, $A = LU$, where L is a lower triangle matrix and U is an upper triangle matrix, which means

$$\det A = \det L \det U = \prod_{i=1}^{n} l_{ii} \prod_{j=1}^{n} u_{jj}.$$

Moreover, one can always make $u_{ii} = 1$ (or $l_{ii} = 1$) for all i and

$$\det A = \det L = \prod_{i=1}^{n} l_{ii}$$

holds. Notice that LU decomposition can be understood as the matrix form of Gaussian elimination.

References

[Aar09a] G. Aarts, *Can stochastic quantization evade the sign problem? The relativistic Bose gas at finite chemical potential*, Phys. Rev. Lett. **102** (2009) 131601 [`arXiv:0810.2089 [hep-lat]`].

[Aar09b] G. Aarts, *Complex Langevin dynamics at finite chemical potential: Mean field analysis in the relativistic Bose gas*, JHEP **05** (2009) 052 [`arXiv:0902.4686 [hep-lat]`].

[AdFGW13] O. Akerlund, P. de Forcrand, A. Georges, and P. Werner, *Dynamical Mean Field Approximation Applied to Quantum Field Theory*, Phys. Rev. D **88** (2013) 125006 [`arXiv:1305.7136 [hep-lat]`].

[ADS15] M. Aizenman, H. Duminil-Copin, and V. Sidoravicius, *Random Currents and Continuity of Ising Model's Spontaneous Magnetization*, Communications in Mathematical Physics **334** (Mar., 2015) 719–742 [`arXiv:1311.1937 [math-ph]`].

[AI96] F. F. Assaad and M. Imada, *Insulator-metal transition in the one- and two-dimensional hubbard models*, Phys. Rev. Lett. **76** (Apr, 1996) 3176–3179 [`arXiv:cond-mat/9510084`].

[Aiz81] M. Aizenman, *Proof of the Triviality of ϕ_d^4 Field Theory and Some Mean-Field Features of Ising Models for $d > 4$*, Phys. Rev. Lett. **47** (1981) 886–886.

[Aiz82] M. Aizenman, *Geometric Analysis of ϕ^4 Fields and Ising Models. Parts I and II*, Commun. Math. Phys. **86** (1982) 1.

[AK21a] S. Akiyama and D. Kadoh, *More about the Grassmann tensor renormalization group*, JHEP **10** (2021) 188 [`arXiv:2005.07570 [hep-lat]`].

[AK21b] S. Akiyama and Y. Kuramashi, *Tensor renormalization group approach to (1+1)-dimensional Hubbard model*, Phys. Rev. D **104** (2021) 014504 [`arXiv:2105.00372 [hep-lat]`].

[AKK⁺20] S. Akiyama, D. Kadoh, Y. Kuramashi, T. Yamashita, and Y. Yoshimura, *Tensor renormalization group approach to four-dimensional complex ϕ^4 theory at finite density*, JHEP **09** (2020) 177 [`arXiv:2005.04645 [hep-lat]`].

[AKY18] K.-I. Aoki, S.-I. Kumamoto, and M. Yamada, *Phase structure of NJL model with weak renormalization group*, Nucl. Phys. B **931** (2018) 105–131 [`arXiv:1705.03273 [hep-th]`].

[AKY21a] S. Akiyama, Y. Kuramashi, and T. Yamashita, *Metal-insulator transition in (2+1)-dimensional Hubbard model with tensor renormalization group*, `arXiv:2109.14149 [cond-mat.str-el]`.

[AKY21b] S. Akiyama, Y. Kuramashi, and Y. Yoshimura, *Phase transition of four-dimensional lattice ϕ^4 theory with tensor renormalization group*, Phys. Rev. D **104** (2021) 034507 [`arXiv:2101.06953 [hep-lat]`].

[AKYY19] S. Akiyama, Y. Kuramashi, T. Yamashita, and Y. Yoshimura, *Phase transition of four-dimensional Ising model with higher-order tensor renormalization group*, Phys. Rev. **D100** (2019) 054510 [`arXiv:1906.06060 [hep-lat]`].

[AKYY20]   S. Akiyama, Y. Kuramashi, T. Yamashita, and Y. Yoshimura, *Phase transition of four-dimensional Ising model with tensor network scheme*, PoS **LATTICE2019** (2020) 138 [`arXiv:1911.12954 [hep-lat]`].

[AKYY21]   S. Akiyama, Y. Kuramashi, T. Yamashita, and Y. Yoshimura, *Restoration of chiral symmetry in cold and dense Nambu–Jona-Lasinio model with tensor renormalization group*, JHEP **01** (2021) 121 [`arXiv:2009.11583 [hep-lat]`].

[AOT20a]   D. Adachi, T. Okubo, and S. Todo, *Anisotropic Tensor Renormalization Group*, Phys. Rev. B **102** (2020) 054432 [`arXiv:1906.02007 [cond-mat.stat-mech]`].

[AOT20b]   D. Adachi, T. Okubo, and S. Todo, *Bond-weighted Tensor Renormalization Group*, `arXiv:2011.01679 [cond-mat.stat-mech]`.

[AY89]   M. Asakawa and K. Yazaki, *Chiral Restoration at Finite Density and Temperature*, Nucl. Phys. A **504** (1989) 668–684.

[BBC⁺20]   Bañuls, Mari Carmen, Blatt, Rainer, Catani, Jacopo, Celi, Alessio, Cirac, Juan Ignacio, Dalmonte, Marcello, Fallani, Leonardo, Jansen, Karl, Lewenstein, Maciej, Montangero, Simone, Muschik, Christine A., Reznik, Benni, Rico, Enrique, Tagliacozzo, Luca, Van Acoleyen, Karel, Verstraete, Frank, Wiese, Uwe-Jens, Wingate, Matthew, Zakrzewski, Jakub, and Zoller, Peter, *Simulating Lattice Gauge Theories within Quantum Technologies*, Eur. Phys. J. D **74** (2020) 165 [`arXiv:1911.00003 [quant-ph]`].

[BBW04]   T. Baier, E. Bick, and C. Wetterich, *Temperature dependence of antiferromagnetic order in the hubbard model*, Phys. Rev. B **70** (Sep, 2004) 125111 [`arXiv:cond-mat/0309715 [cond-mat.str-el]`].

[BC00]   P. Butera and M. Comi, *Extension to order β^{23} of the high-temperature expansions for the spin-$\frac{1}{2}$ ising model on simple cubic and body-centered cubic lattices*, Phys. Rev. B **62** (Dec, 2000) 14837–14843 [`arXiv:hep-lat/0006009`].

[BC20]   M. C. Bañuls and K. Cichy, *Review on Novel Methods for Lattice Gauge Theories*, Rept. Prog. Phys. **83** (2020) 024401 [`arXiv:1910.00257 [hep-lat]`].

[BCM⁺20]   N. Butt, S. Catterall, Y. Meurice, R. Sakai, and J. Unmuth-Yockey, *Tensor network formulation of the massless schwinger model with staggered fermions*, Phys. Rev. D **101** (May, 2020) 094509 [`arXiv:1911.01285 [hep-lat]`].

[BJM02]   E. Bittner, W. Janke, and H. Markum, *Ising spins coupled to a four-dimensional discrete Regge skeleton*, Phys. Rev. **D66** (2002) 024008 [`arXiv:hep-lat/0205023`].

[BKP89]   S. Booth, R. Kenway, and B. Pendleton, *The Phase Diagram of the Gauge Invariant Nambu-Jona-Lasinio Model*, Phys. Lett. B **228** (1989) 115–120.

[BNW06]   J. Balog, F. Niedermayer, and P. Weisz, *Repairing Stevenson's step in the 4d Ising model*, Nucl. Phys. **B741** (2006) 390–403 [`arXiv:hep-lat/0601016`].

[BS80]   H. W. J. Blöte and R. H. Swendsen, *Critical behavior of the four-dimensional Ising model*, Phys. Rev. B **22** (Nov, 1980) 4481–4483.

[Bub05]   M. Buballa, *NJL model analysis of quark matter at large density*, other thesis, 2005.

[CC20a]   M. Consoli and L. Cosmai, *A resonance of the Higgs field at 700 GeV and a new phenomenology*, `arXiv:2007.10837 [hep-ph]`.

[CC20b]   M. Consoli and L. Cosmai, *The mass scales of the Higgs field*, Int. J. Mod. Phys. A **35** (2020) 2050103 [`arXiv:2006.15378 [hep-ph]`].

[CCC05]   P. Cea, M. Consoli, and L. Cosmai, *Large logarithmic rescaling of the scalar condensate: A Subtlety with substantial phenomenological implications*, `arXiv:hep-lat/0501013`.

[CCC19]   P. Cea, M. Consoli, and L. Cosmai, *Two mass scales for the Higgs field?*, `arXiv:1912.00849 [hep-ph]`.

[CDRMS13] M. Cristoforetti, F. Di Renzo, A. Mukherjee, and L. Scorzato, *Monte Carlo simulations on the Lefschetz thimble: Taming the sign problem*, Phys. Rev. D **88** (2013) 051501 [`arXiv:1303.7204 [hep-lat]`].

[Coh03]   T. D. . Cohen, *Functional integrals for QCD at nonzero chemical potential and zero density*, Phys. Rev. Lett. **91** (2003) 222001 [`arXiv:hep-ph/0307089`].

[Cre87]   M. Creutz, *Species Doubling and Transfer Matrices for Fermionic Fields*, Phys. Rev. D **35** (1987) 1460.

[dF09]   P. de Forcrand, *Simulating QCD at finite density*, PoS **LAT2009** (2009) 010 [`arXiv:1005.0539 [hep-lat]`].

[DN83]   R. F. Dashen and H. Neuberger, *How to Get an Upper Bound on the Higgs Mass*, Phys. Rev. Lett. **50** (1983) 1897.

[DT20]   C. Delcamp and A. Tilloy, *Computing the renormalization group flow of two-dimensional ϕ^4 theory with tensor networks*, Phys. Rev. Res. **2** (2020) 033278 [`arXiv:2003.12993 [cond-mat.str-el]`].

[EV15]   G. Evenbly and G. Vidal, *Tensor network renormalization*, Phys. Rev. Lett. **115** (Oct, 2015) 180405 [`arXiv:1412.0732 [cond-mat.str-el]`].

[EVBK19]   N. Erichson, S. Voronin, S. Brunton, and J. Kutz, *Randomized matrix decompositions using r*, Journal of Statistical Software, Articles **89** (2019) 1–48 [`arXiv:1608.02148 [stat.CO]`].

[Eve17]   G. Evenbly, *Algorithms for tensor network renormalization*, Phys. Rev. B **95** (Jan, 2017) 045117 [`arXiv:1509.07484 [cond-mat.str-el]`].

[FGP+11]   S. Fuchs, E. Gull, L. Pollet, E. Burovski, E. Kozik, T. Pruschke, and M. Troyer, *Thermodynamics of the 3d hubbard model on approaching the néel transition*, Phys. Rev. Lett. **106** (Jan, 2011) 030401 [`arXiv:1009.2759 [cond-mat.quant-gas]`].

[FHK+13]   H. Fujii, D. Honda, M. Kato, Y. Kikukawa, S. Komatsu, and T. Sano, *Hybrid Monte Carlo on Lefschetz thimbles - A study of the residual sign problem*, JHEP **10** (2013) 147 [`arXiv:1309.4371 [hep-lat]`].

[FJJ+90]   C. Frick, K. Jansen, J. Jersak, I. Montvay, P. Seuferling, and G. Munster, *Numerical Simulation of the Scalar Sector of the Standard Model in the Symmetric Phase*, Nucl. Phys. **B331** (1990) 515–530.

[FMOU90]   M. Fukugita, H. Mino, M. Okawa, and A. Ukawa, *Finite-size scaling of the three-state Potts model on a simple cubic lattice*, Journal of Statistical Physics **59** (Jun, 1990) 1397–1429.

[Fro82]   J. Frohlich, *On the triviality of $\lambda\phi_d^4$ theories and the approach to the critical point in $d_{(-)} > 4$ dimensions*, Nucl. Phys. B **200** (1982) 281–296.

[GK13]   C. Gattringer and T. Kloiber, *Lattice study of the Silver Blaze phenomenon for a charged scalar ϕ^4 field*, Nucl. Phys. B **869** (2013) 56–73 [`arXiv:1206.2954 [hep-lat]`].

[GKKR96]   A. Georges, G. Kotliar, W. Krauth, and M. J. Rozenberg, *Dynamical mean-field theory of strongly correlated fermion systems and the limit of infinite dimensions*, Rev. Mod. Phys. **68** (Jan, 1996) 13–125.

[GKR06]   A. Garg, H. R. Krishnamurthy, and M. Randeria, *Can correlations drive a band insulator metallic?* Phys. Rev. Lett. **97** (Jul, 2006) 046403 [`arXiv:cond-mat/0511351 [cond-mat.str-el]`].

[GN05]   A. Gendiar and T. Nishino, *Phase diagram of the three-dimensional axial next-nearest-neighbor ising model*, Phys. Rev. B **71** (Jan, 2005) 024404 [`arXiv:cond-mat/0210356 [cond-mat.stat-mech]`].

[GW09]   Z.-C. Gu and X.-G. Wen, *Tensor-entanglement-filtering renormalization approach and symmetry-protected topological order*, Phys. Rev. B **80** (Oct, 2009) 155131 [`arXiv:0903.1069 [cond-mat.str-el]`].

[Has01]   M. Hasenbusch, *Monte carlo studies of the three-dimensional ising model in equilibrium*, International Journal of Modern Physics C **12** (2001) 911–1009.

[Has10]   M. Hasenbusch, *Finite size scaling study of lattice models in the three-dimensional Ising universality class*, Phys. Rev. B **82** (2010) 174433 [`arXiv:1004.4486 [cond-mat.stat-mech]`].

[Hir85]   J. E. Hirsch, *Two-dimensional hubbard model: Numerical simulation study*, Phys. Rev. B **31** (Apr, 1985) 4403–4419.

[HJL$^+$87]   A. Hasenfratz, K. Jansen, C. B. Lang, T. Neuhaus, and H. Yoneyama, *The triviality bound of the four-component Φ^4 model*, Phys. Lett. B **199** (1987) 531–535.

[Hua89]   K. Huang, *Triviality of the Higgs Field*, Int. J. Mod. Phys. **A4** (1989) 1037.

[IMK20]   S. Iino, S. Morita, and N. Kawashima, *Boundary conformal spectrum and surface critical behavior of classical spin systems: A tensor network renormalization study*, Phys. Rev. B **101** (2020) 155418 [`arXiv:1911.09907 [cond-mat.stat-mech]`].

[JTM$^+$89]   K. Jansen, T. Trappenberg, I. Montvay, G. Munster, and U. Wolff, *Broken Phase of the Four-dimensional Ising Model in a Finite Volume*, Nucl. Phys. **B322** (1989) 698–720.

[Ken04]   R. Kenna, *Finite size scaling for $O(N)$ ϕ^4-theory at the upper critical dimension*, Nucl. Phys. **B691** (2004) 292–304 [`arXiv:hep-lat/0405023`].

[Kik51]   R. Kikuchi, *A theory of cooperative phenomena*, Phys. Rev. **81** (Mar, 1951) 988–1003.

[KKN+18]   D. Kadoh, Y. Kuramashi, Y. Nakamura, R. Sakai, S. Takeda, and Y. Yoshimura, *Tensor network formulation for two-dimensional lattice $\mathcal{N} = 1$ Wess-Zumino model*, JHEP **03** (2018) 141 [`arXiv:1801.04183 [hep-lat]`].

[KKN+19]   D. Kadoh, Y. Kuramashi, Y. Nakamura, R. Sakai, S. Takeda, and Y. Yoshimura, *Tensor network analysis of critical coupling in two dimensional ϕ^4 theory*, JHEP **05** (2019) 184 [`arXiv:1811.12376 [hep-lat]`].

[KKN+20]   D. Kadoh, Y. Kuramashi, Y. Nakamura, R. Sakai, S. Takeda, and Y. Yoshimura, *Investigation of complex ϕ^4 theory at finite density in two dimensions using TRG*, JHEP **02** (2020) 161 [`arXiv:1912.13092 [hep-lat]`].

[KL93]   R. Kenna and C. B. Lang, *Renormalization group analysis of finite size scaling in the ϕ_4^4 model*, Nucl. Phys. **B393** (1993) 461–479 [`arXiv:hep-lat/9210009`]. [Erratum: Nucl. Phys. **B411**, 340(1994)].

[KN19]   D. Kadoh and K. Nakayama, *Renormalization group on a triad network*, `arXiv:1912.02414 [hep-lat]`.

[Kog79]   J. B. Kogut, *An Introduction to Lattice Gauge Theory and Spin Systems*, Rev. Mod. Phys. **51** (1979) 659.

[KOT21]   D. Kadoh, H. Oba, and S. Takeda, *Triad second renormalization group*, `arXiv:2107.08769 [cond-mat.str-el]`.

[KPST07]   G. D. Kribs, T. Plehn, M. Spannowsky, and T. M. Tait, *Four generations and Higgs physics*, Phys. Rev. D **76** (2007) 075016 [`arXiv:0706.3718 [hep-ph]`].

[KS75]   J. B. Kogut and L. Susskind, *Hamiltonian Formulation of Wilson's Lattice Gauge Theories*, Phys. Rev. D **11** (1975) 395–408.

[LAB+15]   **Simons Collaboration on the Many-Electron Problem** Collaboration, J. P. F. LeBlanc, A. E. Antipov, F. Becca, I. W. Bulik, G. K.-L. Chan, C.-M. Chung, Y. Deng, M. Ferrero, T. M. Henderson, C. A. Jiménez-Hoyos, E. Kozik, X.-W. Liu, A. J. Millis, N. V. Prokof'ev, M. Qin, G. E. Scuseria, H. Shi, B. V. Svistunov, L. F. Tocchio, I. S. Tupitsyn, S. R. White, S. Zhang, B.-X. Zheng, Z. Zhu, and E. Gull, *Solutions of the two-dimensional hubbard model: Benchmarks and results from a wide range of numerical algorithms*, Phys. Rev. X **5** (Dec, 2015) 041041 [`arXiv:1505.02290 [cond-mat.str-el]`].

[LE19]   W. Lan and G. Evenbly, *Tensor Renormalization Group Centered About a Core Tensor*, Phys. Rev. B **100** (2019) 235118 [`arXiv:1906.09283 [quant-ph]`].

[Lin86]   M. Lindner, *Implications of Triviality for the Standard Model*, Z. Phys. C **31** (1986) 295.

[LM09]   P. H. Lundow and K. Markström, *Critical behavior of the Ising model on the four-dimensional cubic lattice*, Phys. Rev. E **80** (Sep, 2009) 031104 [`arXiv:1202.3031 [cond-mat.stat-mech]`].

[LM11]   P. H. Lundow and K. Markström, *Non-vanishing boundary effects and quasi-first order phase transitions in high dimensional Ising models*, Nucl. Phys. **B845** (2011) 120–139 [`arXiv:1010.5958 [cond-mat.stat-mech]`].

[LMQ$^+$13]   Y. Liu, Y. Meurice, M. P. Qin, J. Unmuth-Yockey, T. Xiang, Z. Y. Xie, J. F. Yu, and H. Zou, *Exact Blocking Formulas for Spin and Gauge Models*, Phys. Rev. **D88** (2013) 056005 [`arXiv:1307.6543 [hep-lat]`].

[LN07]   M. Levin and C. P. Nave, *Tensor renormalization group approach to two-dimensional classical lattice models*, Phys. Rev. Lett. **99** (2007) 120601 [`arXiv:cond-mat/0611687 [cond-mat.stat-mech]`].

[LS87]   I.-H. Lee and R. E. Shrock, *Chiral Symmetry Breaking Phase Transition in Lattice Gauge Higgs Theories With Fermions*, Phys. Rev. Lett. **59** (1987) 14.

[LSS90a]   I.-H. Lee, J. Shigemitsu, and R. E. Shrock, *Lattice Study of a Yukawa Theory With a Real Scalar Field*, Nucl. Phys. B **330** (1990) 225–260.

[LSS90b]   I.-H. Lee, J. Shigemitsu, and R. E. Shrock, *Study of Different Lattice Formulations of a Yukawa Model With a Real Scalar Field*, Nucl. Phys. B **334** (1990) 265–278.

[LW68]   E. H. Lieb and F. Y. Wu, *Absence of mott transition in an exact solution of the short-range, one-band model in one dimension*, Phys. Rev. Lett. **20** (Jun, 1968) 1445–1448.

[LW87]   M. Lüscher and P. Weisz, *Scaling Laws and Triviality Bounds in the Lattice ϕ^4 Theory (I) One Component Model in the Symmetric Phase*, Nucl. Phys. **B290** (1987) 25–60.

[LW88]   M. Lüscher and P. Weisz, *Scaling Laws and Triviality Bounds in the Lattice ϕ^4 Theory (II) One Component Model in the Phase with Spontaneous Symmetry Breaking*, Nucl. Phys. **B295** (1988) 65–92.

[LW89]   M. Lüscher and P. Weisz, *Scaling Laws and Triviality Bounds in the Lattice ϕ^4 Theory (III) N Component Model*, Nucl. Phys. **B318** (1989) 705–741.

[LW03]   E. H. Lieb and F. Wu, *The one-dimensional hubbard model: a reminiscence*, Physica A: Statistical Mechanics and its Applications **321** (2003) 1–27 [`arXiv:cond-mat/0207529 [cond-mat.str-el]`].

[Meu21]   Y. Meurice, *Quantum Field Theory*. 2053-2563. IOP Publishing, 2021.

[MIZK18]   S. Morita, R. Igarashi, H.-H. Zhao, and N. Kawashima, *Tensor renormalization group with randomized singular value decomposition*, Phys. Rev. E **97** (Mar, 2018) 033310 [`arXiv:1712.01458 [cond-mat.stat-mech]`].

[MK21]   S. Morita and N. Kawashima, *Global optimization of tensor renormalization group using the corner transfer matrix*, Phys. Rev. B **103** (2021) 045131 [`arXiv:2009.01997 [cond-mat.stat-mech]`].

[MKO18]   Y. Mori, K. Kashiwa, and A. Ohnishi, *Application of a neural network to the sign problem via the path optimization method*, PTEP **2018** (2018) 023B04 [`arXiv:1709.03208 [hep-lat]`].

[MM97]   I. Montvay and G. Münster, *Quantum Fields on a Lattice*. Cambridge Monographs on Mathematical Physics. Cambridge University Press, 1997.

[MOR19]   *Calculation of higher-order moments by higher-order tensor renormalization group*, Computer Physics Communications **236** (2019) 65 – 71 [`arXiv:1806.10275 [cond-mat.stat-mech]`].

[MSUY20]   Y. Meurice, R. Sakai, and J. Unmuth-Yockey, *Tensor field theory with applications to quantum computing*, `arXiv:2010.06539 [hep-lat]`.

[Nag21]   K. Nagata, *Finite-density lattice QCD and sign problem: current status and open problems*, `arXiv:2108.12423 [hep-lat]`.

[NHO⁺01]   T. Nishino, Y. Hieida, K. Okunishi, N. Maeshima, Y. Akutsu, and A. Gendiar, *Two-Dimensional Tensor Product Variational Formulation*, Progress of Theoretical Physics **105** (03, 2001) 409–417 [`arXiv:cond-mat/0011103 [cond-mat.stat-mech]`].

[NJL61a]   Y. Nambu and G. Jona-Lasinio, *Dynamical Model of Elementary Particles Based on an Analogy with Superconductivity. I*, Phys. Rev. **122** (1961) 345–358.

[NJL61b]   Y. Nambu and G. Jona-Lasinio, *Dynamical Model of Elementary Particles Based on an Analogy with Superconductivity. II*, Phys. Rev. **124** (1961) 246–254.

[Oba20]   H. Oba, *Cost Reduction of Swapping Bonds Part in Anisotropic Tensor Renormalization Group*, PTEP **2020** (2020) 013B02 [`arXiv:1908.07295 [cond-mat.stat-mech]`].

[OG18]   O. Orasch and C. Gattringer, *Canonical simulations with worldlines: An exploratory study in ϕ_2^4 lattice field theory*, Int. J. Mod. Phys. A **33** (2018) 1850010 [`arXiv:1708.02817 [hep-lat]`].

[ONU21]   K. Okunishi, T. Nishino, and H. Ueda, *Developments in the Tensor Network – from Statistical Mechanics to Quantum Entanglement*, `arXiv:2111.12223 [cond-mat.stat-mech]`.

[Orú19]   R. Orús, *Tensor networks for complex quantum systems*, APS Physics **1** (2019) 538–550 [`arXiv:1812.04011 [cond-mat.str-el]`].

[PBH⁺07]   N. Paris, K. Bouadim, F. Hebert, G. G. Batrouni, and R. T. Scalettar, *Quantum monte carlo study of an interaction-driven band-insulator–to–metal transition*, Phys. Rev. Lett. **98** (Jan, 2007) 046403 [`arXiv:cond-mat/0607707 [cond-mat.str-el]`].

[PZ13]   J. M. Pawlowski and C. Zielinski, *Thirring model at finite density in 2+1 dimensions with stochastic quantization*, Phys. Rev. D **87** (2013) 094509 [`arXiv:1302.2249 [hep-lat]`].

[Shi12a]   Y. Shimizu, *Analysis of the (1+1)-dimensional lattice ϕ^4 model using the tensor renormalization group*, Chin. J. Phys. **50** (2012) 749.

[Shi12b]   Y. Shimizu, *Tensor renormalization group approach to a lattice boson model*, Mod. Phys. Lett. **A27** (2012) 1250035.

[Shr14]   R. Shrock, *Question of an ultraviolet zero of the beta function of the $\lambda(\vec{\phi}^2)_4^2$ theory*, Phys. Rev. D **90** (2014) 065023 [`arXiv:1408.3141 [hep-th]`].

[Shr16]   R. Shrock, *Study of the six-loop beta function of the $\lambda\phi_4^4$ theory*, Phys. Rev. D **94** (2016) 125026 [`arXiv:1610.03733 [hep-th]`].

[Shr17]   R. Shrock, *Study of the question of an ultraviolet zero in the six-loop beta function of the O(N) $\lambda|\vec{\phi}|^4$ theory*, Phys. Rev. D **96** (2017) 056010 [`arXiv:1707.06248 [hep-th]`].

[SHT10]   G. Sordi, K. Haule, and A.-M. S. Tremblay, *Finite doping signatures of the mott transition in the two-dimensional hubbard model*, Phys. Rev. Lett. **104** (Jun, 2010) 226402 [`arXiv:1002.2960 [cond-mat.str-el]`].

[Ste05]   P. M. Stevenson, *Comparison of conventional RG theory with lattice data for the 4d Ising model*, Nucl. Phys. **B729** (2005) 542–557 [`arXiv:hep-lat/0507038`].

[Suz76]   M. Suzuki, *Generalized Trotter's Formula and Systematic Approximants of Exponential Operators and Inner Derivations with Applications to Many Body Problems*, Commun. Math. Phys. **51** (1976) 183–190.

[SV87]   E. Sanchez-Velasco, *A finite-size scaling study of the 4D Ising model*, J. Phys. **A20** (1987) 5033.

[Tak19]   S. Takeda, *Tensor network approach to real-time path integral*, PoS **LATTICE2019** (2019) 033 [`arXiv:1908.00126 [hep-lat]`].

[Tak21]   S. Takeda, *A novel method to evaluate real-time path integral for scalar ϕ^4 theory*, 8, 2021. `arXiv:2108.10017 [hep-lat]`.

[Tro59]   H. F. Trotter, *On the product of semi-groups of operators*, Proceedings of the American Mathematical Society **10** (1959) 545–551. `http://www.jstor.org/stable/2033649`.

[TY15]   S. Takeda and Y. Yoshimura, *Grassmann tensor renormalization group for the one-flavor lattice Gross-Neveu model with finite chemical potential*, PTEP **2015** (2015) 043B01 [`arXiv:1412.7855 [hep-lat]`].

[Whi92]   S. R. White, *Density matrix formulation for quantum renormalization groups*, Phys. Rev. Lett. **69** (1992) 2863–2866.

[Whi93]   S. R. White, *Density-matrix algorithms for quantum renormalization groups*, Phys. Rev. B **48** (1993) 10345–10356.

[Wil74]   K. G. Wilson, *Confinement of Quarks*, Phys. Rev. D **10** (1974) 2445–2459.

[WK74]   K. G. Wilson and J. B. Kogut, *The Renormalization group and the ε expansion*, Phys. Rept. **12** (1974) 75–199.

[WR73]   F. J. Wegner and E. K. Riedel, *Logarithmic Corrections to the Molecular-Field Behavior of Critical and Tricritical Systems*, Phys. Rev. B **7** (Jan, 1973) 248–256.

[WXC+14]   S. Wang, Z.-Y. Xie, J. Chen, B. Normand, and T. Xiang, *Phase transitions of ferromagnetic potts models on the simple cubic lattice*, Chinese Physics Letters **31** (Jul, 2014) 070503 [`arXiv:1405.1179 [cond-mat.stat-mech]`].

[XCQ+12]   Z. Y. Xie, J. Chen, M. P. Qin, J. W. Zhu, L. P. Yang, and T. Xiang, *Coarse-graining renormalization by higher-order singular value decomposition*, Phys. Rev. B **86** (Jul, 2012) 045139 [`arXiv:1201.1144 [cond-mat.stat-mech]`].

[YGW17]   S. Yang, Z.-C. Gu, and X.-G. Wen, *Loop optimization for tensor network renormalization*, Phys. Rev. Lett. **118** (Mar, 2017) 110504 [`arXiv:1512.04938 [cond-mat.str-el]`].

[YKN+18]   Y. Yoshimura, Y. Kuramashi, Y. Nakamura, S. Takeda, and R. Sakai, *Calculation of fermionic Green functions with Grassmann higher-order tensor renormalization group*, Phys. Rev. **D97** (2018) 054511 [`arXiv:1711.08121 [hep-lat]`].

[YS21]   T. Yamashita and T. Sakurai, *A Parallel Computing Method for the Higher Order Tensor Renormalization Group*, `arXiv:2110.03607 [hep-lat]`.